University of South Florida
Scholar Commons

Graduate Theses and Dissertations   Graduate School

2009

A quasi Yagi antenna with end fire radiation over a metal ground

Sergio E. Melais
University of South Florida

Follow this and additional works at: http://scholarcommons.usf.edu/etd

Part of the American Studies Commons

Scholar Commons Citation

A Quasi Yagi Antenna with End Fired Radiation over a Metal Ground

by

Sergio E. Melais

A dissertation submitted in partial fulfillment
of the requirements for the degree of
Doctor of Philosophy
Department of Electrical Engineering
College of Engineering
University of South Florida

Major Professor: Thomas M. Weller, Ph.D.
Jing Wang, Ph.D.
Kenneth Buckle, Ph.D.
Miguel A. Labrador, PhD.
Dennis Killinger, Ph.D.

Date of Approval:
October 23, 2009

Keywords: high impedance surface, beam steering, Jerusalem cross, angular stability, surface waves

Dedication

To my Mother Fidelina de Melais Rodriguez and my Father Sergio E. Melais L.

Acknowledgements

I will like to express my gratitude to Dr. Thomas Weller for his unlimited support, excellent guidance, and for granting me with the opportunity to work in various projects such as the ones developed in this dissertation. The technical insights and problem solving skills I have learned from him have influenced greatly my development as a better engineer. Additionally, I want to thank my committee member Dr. Jing Wang, Dr. Kenneth Buckle, Dr. Dennis Killinger, Dr. Miguel A. Labrador and Dr. Nagarajan Ranganathan for reviewing this dissertation and participating in the oral defense.

Next, I want to thank my colleagues in the Antennas and Propagation lab (412) for their great help and friendship, especially, Bojana Zivanovic, Alberto Rodriguez, Srinath Balachandran, Saravana P. Natarajan, Scott Skidmore, Quenton Bonds, Suzette Aguilar, Henrry La Rosa and David Cure.

Finally, I want to sincerely thank my mother Fidelina de Melais and my father Sergio Melais for their unlimited lover and support. They are both the most important people in my life and are the inspiration to my work, I will forever be thankful to them.

Table of Contents

List of Tables

List of Figures

A Quasi Yagi Antenna with End Fire Radiation over a Metal Ground

Sergio E. Melais

ABSTRACT

This dissertation presents a detailed investigation on the development of a quasi Yagi antenna with end fire radiation at 2.4 GHz (ISM band) over a metal reflector. Realization of an end fire radiator on top of a metal ground is very difficult because the reflected waves and image currents from the ground degrade the frequency bandwidth and steer the radiation pattern in the broadside direction. This destructive interference is reduced in this research through two quasi Yagi-ground configurations. The first arrangement utilizes a substrate of suitable thickness (7.5mm-0.19 λ_g) to displace the ground away from the antenna. The second design implements a high impedance surface (HIS) as ground plane for the antenna. The preferred HIS is the Jerusalem Cross Frequency Selective Surface (JC-FSS) because of its compact size, numerous parameters for tuning and frequency stability in the operating band for a large angular spectrum of TE and TM polarized incident waves. In this work a new parameter is added to the model used for the derivation of the JC-FSS which accounts for the substrate of the antenna lying on top of the FSS, this addition allows for a smaller cell grid.

The results for the quasi Yagi antenna over the 7.5mm grounded slab presented an operational bandwidth of 190 MHz with 40˚ of beam steering in the end fire direction while the quasi Yagi over the JC-FSS offered 260 MHz of functional bandwidth and 54˚

of beam steering towards the end fire direction. In addition, the quasi Yagi design over the JC-FSS decreases the combined profile (antenna/backing structure) by 33% in relation to the 7.5mm grounded slab.

This dissertation combines for the first time a quasi Yagi antenna with a JC-FSS to achieve end fire radiation in the presence of a ground metal.

Chapter 1

Introduction

1.1 Overview

The work presented in this dissertation introduces the design of a printed Yagi-Uda array with end fire radiation at the 2.4 GHz ISM band when backed by a metal reflector. The selected Yagi-Uda array is known in the antenna field as a quasi Yagi antenna. This antenna consists of an array of dipoles printed on a high permittivity substrate and fed by a microstrip to coplanar strip-line transition. Here the ground plane from the microstrip transition is used as the reflector element for the array. The main advantages of a quasi Yagi design for this research are the inherent traits of broadband frequency operation, planar design making it PCB compatible and the radiation profile in the end fire direction. These benefits are relevant because the original application for the antenna was to serve as the communication link for a wireless sensor network inside a multipath rich environment (e.g. inside an aircraft). Additionally the tight locations (e.g. lid for a sensor node behind the cockpit) in which the antenna will be used lead to the desired end fire pattern and back-metal shielding. Unfortunately when the quasi Yagi antenna is backed by a metal ground plane, the image currents from the ground cancel the current of the antenna degrading its operational bandwidth and steering the beam away from the end fire direction.

This dissertation prepares two solutions to reduce the destructive interference present in the quasi Yagi when flushed over a ground metal. The first solution consisted

of printing the quasi Yagi on a grounded dielectric slab, thick enough (0.19λ_g - 7.5 mm) so that the ground metal is sufficiently displaced away from the antenna to minimize adverse affects of image current cancelation and surface wave radiation. The second solution consists of backing the antenna by a textured structure which alters the electromagnetic properties of the ground plane. The mentioned structure, known as a high impedance surfaces (HIS), suppresses the propagation of surfaces waves from radiating into the surrounding medium for a particular frequency band called the band gap frequency. The HIS are modeled by an LC network and at the resonance frequency they present very high impedance. The preferred HIS configuration used for this work is the Jerusalem Cross Frequency Selective Surface (JC-FSS) because the frequency band gap is relatively stable for a large angular (<70˚) spectrum of incident waves. Both presented solutions are fabricated and compared in this work. The first solution offers an operational bandwidth from 2.36 to 2.55 GHz, with a directional beam steering of 40˚ towards the end fire direction. The second solution shows an operational bandwidth from 2.29 GHz to 2.55 GHz, radiation pattern with beam steering towards the end fire direction of 54˚, and an overall profile reduction of 33% in respect with the first solution.

1.2 Dissertation Organization

This dissertation is organized into seven chapters, with one and seven corresponding to the introduction and conclusion respectively, and chapters two through six describing the main contents of the structures designed.

Chapter 2 presents a review on antenna concepts related to the design and operation of the of the quasi Yagi antenna. First a review on array theory is detailed to inform how a directional end fire radiation is obtained from the array of dipoles in the

quasi Yagi antenna. Following this, a description on the properties of surface waves for a dielectric/metal interface is prepared to explain how the ground metal interferes with the radiation pattern of an end fire antenna.

Chapter 3 offers a review on the design of a quasi Yagi antenna. It explains the derivations of the different elements within this array, the balun, the driver and the director. Additionally it offers a study on the impact of the director dipole for this design. Finally a metal backing is added and the degradation of the operational bandwidth and radiation pattern is shown.

Chapter 4 elaborates on the first solution to reduce the ground plane interference to the antenna. A background review is offered on boundary conditions and wave reflection theory to understand how travelling waves propagate. Furthermore a study is carried out to evaluate the impact that the substrate height, shorting vias (connecting ground planes to same potential) and director dipole on the quasi Yagi antenna when packaged over the metal ground.

Chapter 5 presents the design of an electromagnetic textured structure which will be used as ground plane for the quasi Yagi antenna. The selected structure is the JC-FSS. A background review is detailed here comparing the propagation of surface waves in a metal versus on a textured surface. Next, an effective medium model (quasi TEM) based on equations is derived to design the grids elements of this structure for operation at 2.4 GHz. Also an assessment is added to this model including the effect brought in by an antenna (quasi Yagi) flush on top of it. Finally the model design is simulated then measured and the results are compared.

Chapter 6 presents the combined design of the quasi Yagi antenna packaged over the JC-FSS. The design is optimized for operation at 2.4 GHz through simulations in Ansoft HFSS. The simulated and measured data shows good comparison except for a frequency shift on the operational band caused by tolerances to layer adhesion. Furthermore, the simulated results are evaluated against a design of same substrate height packaged over a metal with no FSS included. Finally the measured data of the combined structure is compared to the measured data from chapter 4.

1.3 Contributions

The main contributions from this work are the analysis and development of planar end fire radiators over a metal ground, and expansion on techniques used for elimination of phase reflections and suppression of undesired surface waves from a metal ground.

The first end fire radiator presented here consisted of a quasi Yagi antenna printed over a high profile grounded dielectric slab. The main additions from this configuration are beam steering towards the end fire direction of 40° and reduction of ground interference by displacing ground away from the antenna by a substrate of suitable height (0.19λ). The second end fire configuration consisted of a quasi Yagi packaged over a JC-FSS. This design improves on the previous high profile configuration with 14° of additional beam steering towards the end fire direction and 33% reduction on the overall design profile. Furthermore, an additional feature unique to this work is the addition of the antenna substrate to the closed form equations for the JC-FSS tuning the grid impedance to the desired frequency. To the best of the author's knowledge previous work on a quasi Yagi over a metal ground has not been previously been presented, nor the implementation of the JC-FSS at its backing structure.

1.4 Existing Technology

Existing configurations of antennas (e.g. dipoles, patches) over high impedance structures (e.g. square patch EBG's, Jerusalem Crosses) are reviewed to support the impact and uniqueness of the work presented in this dissertation.

Recent work derived in [1] demonstrates an Archimedean spiral antenna over a square patch electromagnetic band-gap structure (EBG). The implementation of an EBG herein, versus the conventional 0.25λ cavity, provides an overall antenna/EBG profile reduction >69% and allows for the antenna to maintain its wide bandwidth without affecting its directive gain.

Another case developed in [2] shows a wearable dual band (2.4 and 5.1 GHz) coplanar patch antenna combined with a square patch EBG made of common clothing fabrics. The EBG is used here to improve antenna gain (3 dB) and reduce back radiation into the body (>10 dB). An equivalent design is presented in [3] offering the same characteristics (high gain and low back radiation), but it used a non conformal material instead and the EBG arrangement consists of a Jerusalem Cross slot array.

An example published in [4] shows a flared dipole with quasi end fire radiation at 3 GHz over a high impedance surface (HIS) consisting of an array of hexagonal grids (thumbtacks). The amount of angular beam steering towards the end fire direction depends on the impedance of the HIS which can be tuned in real time by a variety of methods (e.g. electronically-incorporating varactor diodes [5]).

Work presented in [6] illustrates a broadband diamond dipole antenna over a Jerusalem Cross Frequency Selective Surface. The bandwidth for the combined structure

extends from 5 to 11 GHz with high gain (>6 dB) from 3.7 to 6.8 GHz and non disturbed (without unwanted nulls) directive pattern up to 7 GHz.

The evaluation listed above shows various instances of antennas placed over high impedance surfaces. The primary assessed benefits from backing antennas with high impedance structures (versus a regular ground plane) are the preservation of the antenna bandwidth, improved gain, reduction of back radiation and increased radiation efficiency.

In comparison to the quasi Yagi over JC-FSS developed in this dissertation, the majority of the existing antenna/EBG designs offer radiation in the broadside direction. The particular example from [4] with quasi end fire radiation uses a more complex EBG arrangement than the one elaborated on in this dissertation.

Chapter 2

Background Review

2.1 Introduction

This chapter presents a review on antenna concepts related to the design and operation of the of the quasi Yagi antenna. First, a review on array theory is offered, explaining why an array configuration is preferred to achieve end fire radiation. In the selected array arrangement, Yagi-Uda array, only one of the elements is energized to avoid complexity of input feed interconnects, while the rest of the elements are excited by parasitic coupling. Following this, it is explained how by varying the parasitic element length and spacing with respect to the driven element the forward and backward direction of the pattern can be altered. Finally, the properties of surface waves on a dielectric/metal interface are defined. Understanding the interference from surface waves is of importance because these will affect the quasi Yagi end fire pattern and input matching once a metal backing is placed beneath its radiating elements.

2.2 Array Theory

The antenna prepared for this research requires maximum radiation towards a particular direction, the axis of the antenna. If a single antenna element is used, an antenna of large size will be necessary. To avoid this, a configuration made of an assembly of antenna elements in an array configuration is preferred. The arrangement of the antenna elements in this array allow for control of the radiating direction. In addition,

the array configuration can be arranged such that the radiation between elements sums up to give maximum radiation in a particular direction and minimum in others.

The total field of the array is derived from the vector addition of the fields radiated by individual elements. To obtain a directive pattern, it is essential that the fields from the elements of the array interfere constructively (add) in the preferred direction and interfere destructively (cancel) in the remaining space. For an array of identical elements, aspects of the design that influence the array pattern include [7]:

- Geometrical configuration of overall array (linear, rectangular, spherical)

- Separation between elements

- Excitation amplitude and phase of the individual elements

- Pattern of the individual elements

An array configuration is often formed by organizing the elements in a linear array. To assist with the interpretation of the array operation, a two element array is used. For an array of two infinitesimal horizontal dipoles, as shown in Figure 2.1 (a), the total field radiated by the two elements, assuming no coupling between the elements, is equivalent to the sum of the two as described by (in the y-z plane)

$$\text{Et} = \text{E1} + \text{E2} = \hat{a}_\theta j\eta \frac{KI_0 l}{4\pi} \left\{ \frac{e^{-j\left[kr1 - \left(\frac{\beta}{2} \right) \right]}}{r1} \cos\theta 1 + \frac{e^{-j\left[kr2 + \left(\frac{\beta}{2} \right) \right]}}{r2} \cos\theta 2 \right\} \qquad (2.1)$$

where β is the difference in phase excitation between the elements. The magnitude excitation for each radiator is identical. Assuming far-field observation and referring to

Figure 2.1 (b), $\qquad\qquad\qquad \theta_1 \approx \theta_1 \approx \theta_1$ $\qquad\qquad\qquad\qquad\qquad$ (2.2)

for phase variations $\qquad\qquad\qquad \text{r1} \approx r - \frac{d}{2}\cos\theta$ $\qquad\qquad\qquad\qquad$ (2.2a)

$$\text{r2} \approx r + d/2\cos\theta \qquad\qquad\qquad (2.2b)$$

8

for amplitude variations $\qquad\qquad r1 \approx r2 \approx r$ $\qquad\qquad\qquad$ (2.2c)

resulting in equation (2.1) which reduces to

$$Et = \hat{a}_\theta j\eta \frac{kI_o \ell e^{-jkr}}{4\pi r} \cos\left[e^{\frac{j\cdot(kd\cos\theta+\beta)}{2}} + e^{\frac{-j\cdot(kd\cos\theta+\beta)}{2}}\right]$$

$$Et = \hat{a}_\theta j\eta \frac{kI_o \ell e^{-jkr}}{4\pi r} \cos\left\{2\cdot\cos\left[\frac{1}{2}(kd\cos\theta+\beta)\right]\right\} \qquad (2.3)$$

From equation (2.3) it is evident that the total field of the array is equal to the field of a single element placed at the origin multiplied by an array factor which for the case of the two element array is

$$AF = 2\cdot\cos\left[\frac{1}{2}(kd\cos\theta+\beta)\right] \qquad (2.4)$$

and when normalized

$$AF_n = \cos\left[\frac{1}{2}(kd\cos\theta+\beta)\right] \qquad (2.5)$$

From (2.5) it is determined that the array factor is dependent on the geometry of the array (d) and the excitation phase (β). Varying these parameters allows controlled of the array factor and the total field of the array.

(a) $\qquad\qquad\qquad\qquad\qquad\qquad$ (b)
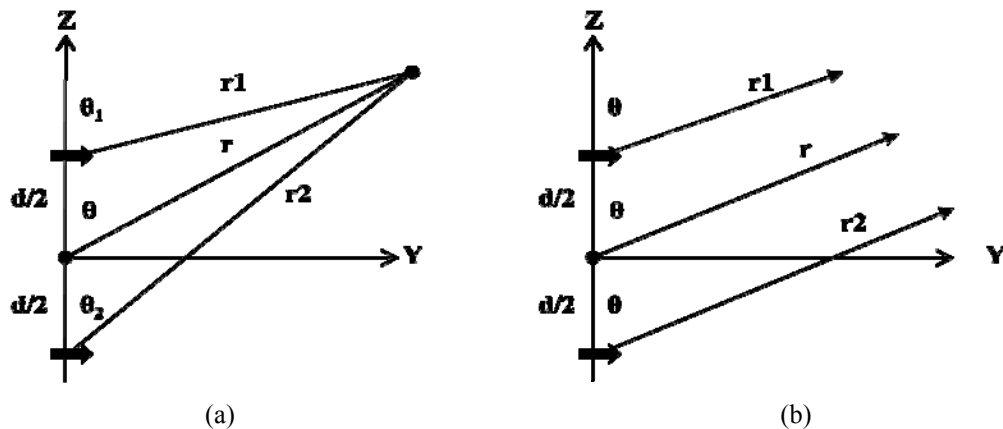
Figure 2.1 - Geometry of two element array along the Z-axis. (a) Two infinitesimal dipoles. (b) Far field observations.

The total field calculated from (2.3) is also referred as pattern multiplication for an array of identical elements. The presented derivation, even though it refers to a two element array, is also valid for arrays with any number of identical elements regardless of identical magnitude, phases or spaces between them.

Following the two element array case, a more generalized method for N element arrays is included as illustrated in Figure 2.2 (a). An array of identical elements with equal magnitude and with progressive phase (current in an element leads the current of the proceeding element) is referred to as a uniform array. The array factor is obtained similarly as to the two element array (2.3), assuming the elements to be point sources, the total field is formed by multiplying the array factor of the isotropic sources by the field of a single element. The array factor is calculated by

$$AF = 1 + e^{+j(kd \cos \theta + \beta)} + e^{+2j(kd \cos \theta + \beta)} + \cdots + e^{+(N-1)j(kd \cos \theta + \beta)}$$

$$AF = \sum_{n=1}^{N} e^{j(n-1)(kd \cos \theta + \beta)} \tag{2.6}$$

where
$$\psi = kd \cos \theta + \beta$$

From (2.6) the total array factor is a sum of exponentials, it can also be described by the vector sum of N phasors each of unit amplitude and progressive phase ψ. This is explained by Figure 2.2 (b). From this phasor diagram it is clear that the amplitude and AF is controlled in uniform arrays by the relative phase ψ between elements. For non-uniform arrays the amplitude and phase are used to control the formation and distribution of the array factor.
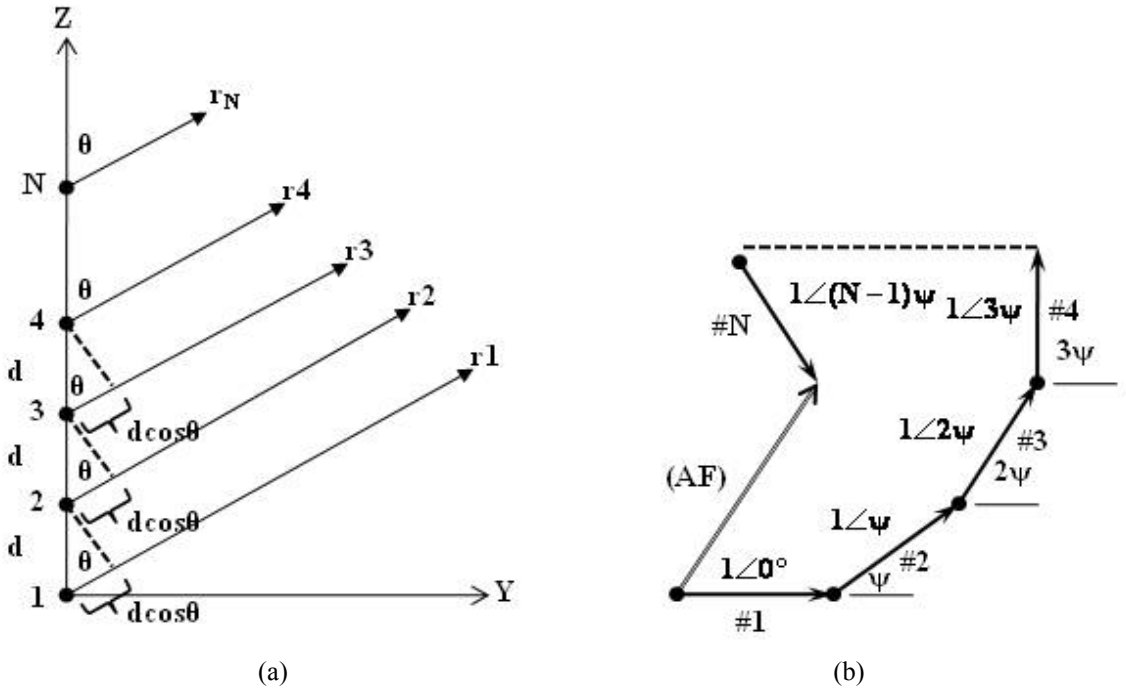
Figure 2.2 - N-element array of isotropic source along z axis. (a) Far field geometry. (b) Phasor diagram.

To simplify the expression for the array factor from (2.6) into a compact and closed form, both sides are multiplied by $e^{j\psi}$ resulting

$$(AF)e^{j\psi} = e^{j\psi} + e^{j2\psi} + e^{j3\psi} + \cdots + e^{j(N-1)\psi} + e^{jN\psi} \qquad (2.7)$$

subtracting (2.6) from (2.7) simplifies the expression to

$$AF(e^{j\psi} - 1) = (-1 + e^{jN\psi}) \qquad (2.8)$$

which can be written as

$$AF = \left[\frac{e^{jN\psi} - 1}{e^{j\psi} - 1}\right] = e^{j\left[\frac{(N-1)}{2}\right]\psi}\left[\frac{e^{j\left(\frac{N}{2}\right)\psi} - e^{-j\left(\frac{N}{2}\right)\psi}}{e^{j\left(\frac{1}{2}\right)\psi} - e^{-j\left(\frac{1}{2}\right)\psi}}\right]$$

$$AF = e^{j\left[\frac{(N-1)}{2}\right]\psi}\left[\frac{\sin\left(\frac{N}{2}\psi\right)}{\sin\left(\frac{1}{2}\psi\right)}\right] \qquad (2.9)$$

11

If the reference point is located in the center of the array, the array factor from (2.9) is reduced to

$$AF = \left| \frac{\sin\left(\frac{N}{2}\psi\right)}{\sin\left(\frac{1}{2}\psi\right)} \right| \qquad (2.10)$$

For small values of ψ (2.10) can be estimated by

$$AF \approx \left| \frac{\sin\left(\frac{N}{2}\psi\right)}{\left(\frac{\psi}{2}\right)} \right| \qquad (2.11)$$

Equation (2.10) and (2.11) are normalized to the maximum value N resulting in

$$(AF)_n = \frac{1}{N} \left| \frac{\sin\left(\frac{N}{2}\psi\right)}{\sin\left(\frac{1}{2}\psi\right)} \right| \qquad (2.12)$$

$$(AF)_n \approx \left| \frac{\sin\left(\frac{N}{2}\psi\right)}{\left(\frac{N}{2}\psi\right)} \right| \qquad (2.13)$$

12

2.2.1 End Fire Array

An ordinary end fire array is an array of elements with maximum radiation along the axis of the array ($\theta = 0°$ or $180°$, Figure 2.3) [7]. The individual currents are equal in magnitude but the phase varies progressively along the line in such a way as to make the overall arrangement unidirectional. Here the direction of the signal lies along the axis of the antenna.

To direct the first maximum towards $\theta = 0°$

$$\psi = kd \cos \theta + \beta|_{\theta=0°} = kd + \beta = 0 \rightarrow \beta = -kd \tag{2.18}$$

and towards $\theta = 180°$

$$\psi = kd \cos \theta + \beta|_{\theta=180°} = -kd + \beta = 0 \rightarrow \beta = kd \tag{2.19}$$

An important parameter of great significant for control on the direction of radiation is the separation (d) of the array elements. For the case of one maximum in the end-fire direction, the maximum separation between elements has to be less than half a wavelength $d_{max} < \lambda/2$.
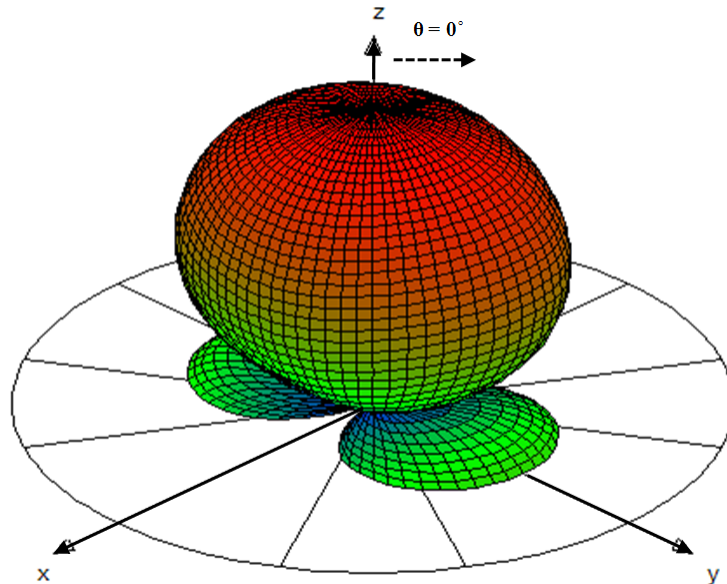
Figure 2.3 - End-fire pattern for $\theta = 0°$.

13

2.2.2 Arrangement Involving Parasitic Antennas

The feed line for interconnecting the antennas of an array must be arranged so that the driving voltage appears at each antenna with proper amplitude and phase. Because of feed line complexities, sometimes is desirable to feed certain antennas of an array parasitically. This is the case for the quasi Yagi of this research. The currents observed in the parasitic elements (director and reflector dipole) are obtained from the radiation of an adjacent driven element (driven dipole). However, when the parasitic elements are displaced away from the driven element these experience a rapid drop in the magnitude of the current. Hence small separations are preferred. On the other hand, the phase of the parasitic current relative to the driven element increases with separation. In order to obtain the necessary phase separation, it may be optimal to operate with considerable spacing, perhaps a quarter wavelength (0.25λ) or even one half wavelength (0.5λ). Therefore a compromise must be made between magnitude and phase, separating the parasitic elements by distances smaller than expected. Furthermore, another factor used to alter the phase of the parasitic is by varying the length.

For the case of an end fire array as shown in Figure 2.4, the driven antenna and a single parasitic are separated by a 0.25λ, the current in the parasitic is much smaller than in the driven antenna, and as a result the front to back ratio is usually low.
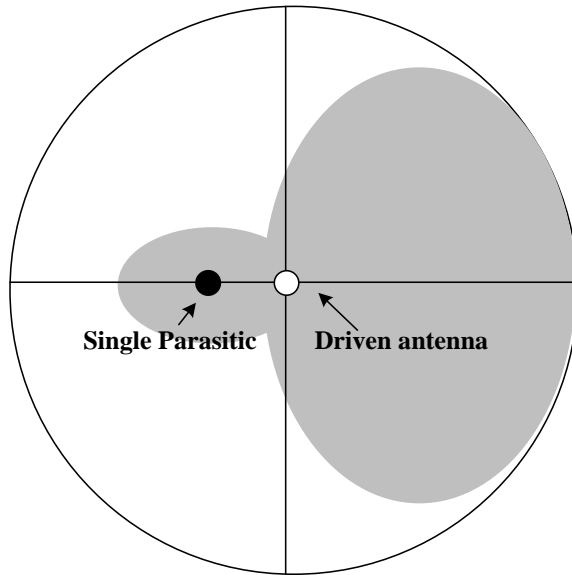
Figure 2.4 - Representative pattern from a single driven antenna together with a single parasitic and separated by one quarter wavelength.

In addition to the quarter-wave spacing between a driven antenna and its parasitic, interesting results are obtained from relatively close spacing [8]. These results are shown in Figure 2.5. The configuration from Figure 2.5 (a) represents a directional pattern both in the plane of the two antennas (x-z) and at right angles (x-y) for closely separated elements (0.04λ). For this close spacing, both elements, the parasitic and driven antenna are resonant. Since these are oppositely phase there is a null along the Y and Z axis. In addition this patter presents a front to back ratio of unity.
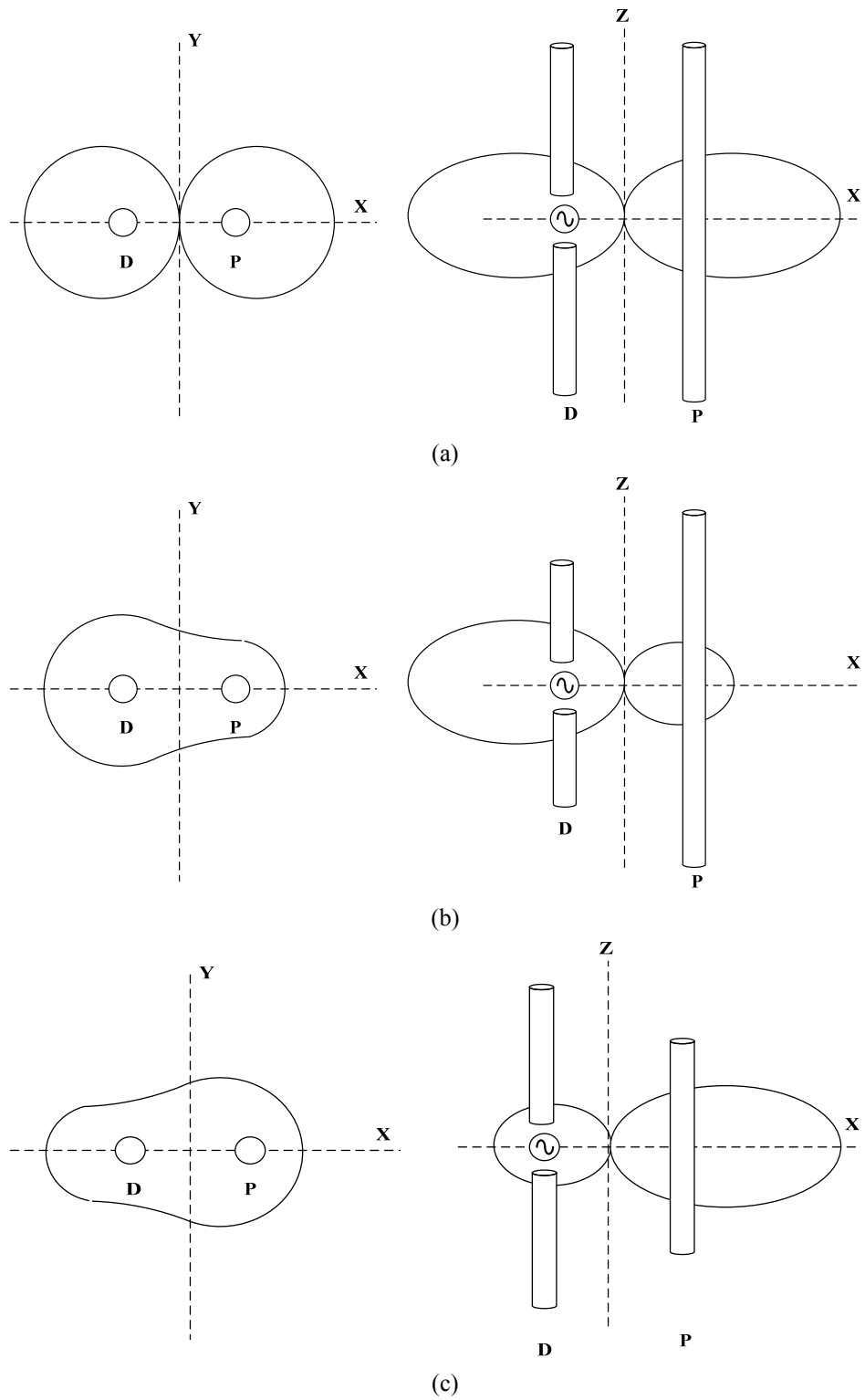
Figure 2.5 - Representative patterns from a driven antenna together with a single closely spaced parasitic. (a) Both elements are resonant. (b) Parasitic element with length increase by 5% acts as reflector. (c) Parasitic element with length shortened by 5% acts as director.

By increasing the length of the parasitic by, for example 5%, while maintaining the spacing the same, the symmetry from Figure 2.5 (a) is altered to Figure 2.5 (b). The parasitic now operates as a reflector given a directive pattern. The front to back ratio is improved but the null along the Y axis is lost. Next, by reducing the length of the parasitic by the same percentage the pattern will remain the same but with opposite direction as represented by Figure 2.5 (c). In this case the parasitic is acting as a director. As expected, the reflector and director can be combined with a driven antenna two from a three elements array, this array is known as a Yagi-Uda antenna.

2.2.3 Yagi Uda Array

A conventional Yagi-Uda array consists of a number of linear dipole elements with one of these elements energized directly by a feeding transmission line while the others act as parasitic radiators whose current are induced by mutual coupling (Figure 2.6). The Yagi-Uda radiator is designed for end-fire radiation by presenting the parasitic element in the forward beam act as directors while those in the back act as reflectors.
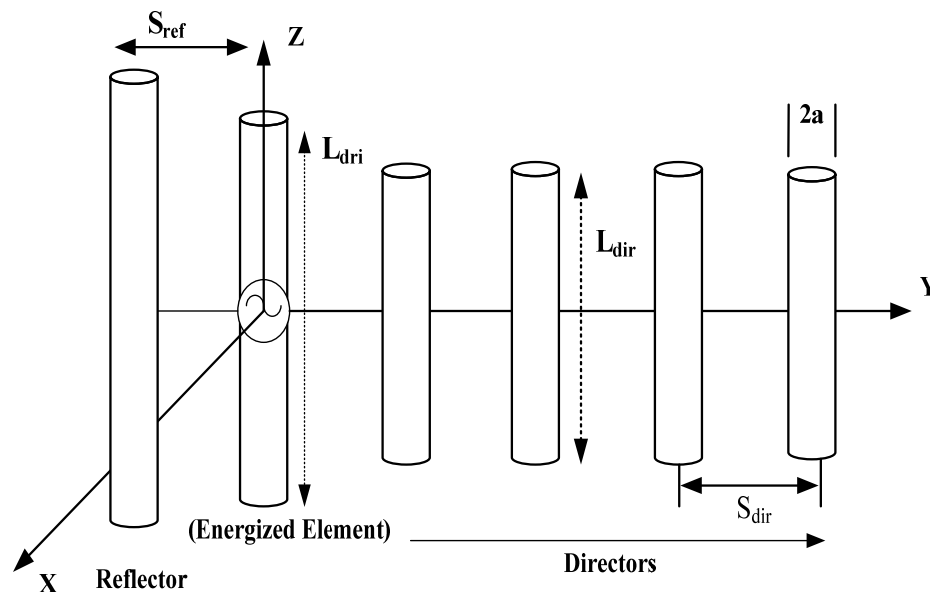
Figure 2.6 - Yagi Uda antenna.

The following guidelines are followed to obtained end-fire beam formation [7]. The parasitic elements in the direction of the beam are smaller in length than the feed element ($L_{dir} < L_{dri}$). As a design standard, the driven element resonates with a length less than $\lambda/2$, usually from 0.45-0.49λ, whereas directors have lengths on the range from 0.4-0.45λ. The directors do not require all being of same length and diameter. The separation between directors (S_{dir}) ranges from 0.3-0.4λ and does not need to be uniform between elements to achieve adequate operation. The length of the reflector is greater than that of the feed element ($L_{ref} > L_{dri}$). Moreover, the separation between the driven element and the reflector (S_{ref}) is smaller than the spacing between the driven element and the nearest director (S_{dir}), presenting optimal size for S_{ref} of 0.25λ.

Since the length of each director is smaller than its respective resonant length, the existing impedance is capacitive and the phase of the currents leads the induced electromagnetic field. Similarly the impedance of the reflector is inductive and the phase of the currents lags the electromagnetic field. The total phase of the currents in the directors and reflectors is not only determined by the length, but also by the separation between adjacent elements. As a result, properly spaced elements with lengths slightly smaller than the corresponding resonant length ($\lambda/2$) operate as directors, forming an array with currents equal in magnitude and progressive phase shift directing the field of the energized element towards the directors. Similarly, a properly spaced element with length equal to the resonant length of $\lambda/2$ or greater functions as a reflector. A Yagi Uda array may be considered as a structure supporting a traveling wave whose performance is dependent on the current distribution of each element and phase velocity of the traveling wave.

18

The radiation characteristics of interest for a Yagi-Uda antenna are the forward and backward gain, input impedance, bandwidth, front to back ratio, and magnitude of minor lobes. These characteristics are controlled by parameters such as length, diameters of directors and reflectors as well as their respective spacing. For example, improvements on input impedance and bandwidth for a Yagi-Uda can be achieved by compromising the gain and/or magnitude of the minor lobes. Another way to increase the input impedance without affecting other parameters is to use an impedance step up element as feed (e.g. two element folded dipole). In addition, enhancements on radiation direction, such as the front to back ratio, can be achieved by increasing the element spacing.

In summary the performance of a Yagi-Uda array is considered into three parts. First, the reflector to feeder arrangement, the reflector spacing and size have negligible effects on the forward gain but large effect on the backward gain (front to back ratio) and input impedance. This criterion is used to optimize antenna parameters without affecting dramatically the gain. Second, the feeder, its length and radius have small effects on the forward gain but large effects on the backward gain and input impedance. In addition, its geometry controls the input impedance commonly made real. Third, the size and spacing of the directors have a large effect on the forward gain, backward gain and input impedance. Consequently the rows of directors are considered to be the most critical elements of the array.

2.3 Properties of Surface Waves

Surface waves are propagating electromagnetic waves that are bound to the interface between two media, for example a dielectric/metal boundary (Figure 2.10). For design purposes, a surface wave is characterized by a single parameter, the wavelength in the direction of propagation along the interface [8]. The various surface wave parameters are next defined and formulas are given for their interrelationship.

For a surface wave propagating on an infinite dielectric/metal boundary, Figure 2.7, the separability condition for the wave equation in rectangular coordinates is

$$k_x{}^2 + k_y{}^2 + k_z{}^2 = k^2 \qquad (2.27)$$
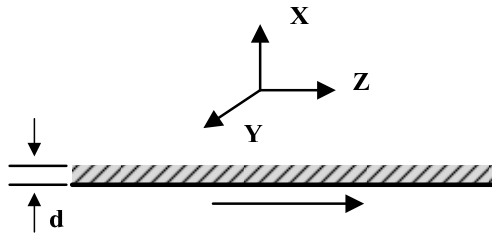
Figure 2.7 - Surface wave propagation over infinite dielectric plane sheet on metal.

where the wave numbers k's are in general complex, $k_x = \beta_x - j\alpha_x$, with β_x the phase constant in radians per unit length and α_x the attenuation in nepers per unit length. The wave number k represents the medium in which the wave travels, $k = \omega\sqrt{\epsilon_0\mu_0}$, with ω as the angular frequency, ε_0 as the dielectric constant, and μ_0 as the permeability. In air k is purely real and related to the wavelength λ by $k = \beta = 2\pi/\lambda$ and to the phase velocity of light c by $k = \omega/c$. Similarly, the phase constant β_z along the surface is related to the surface wavelength λ_z by $\beta_z = 2\pi/\lambda_z$ and to the surface phase velocity v_z by $\beta_z = \omega/v_z$. The next ratios are equivalent

$$\beta_z/k = \lambda/\lambda_z = c/v_z \qquad (2.28)$$

When this ratio is greater than 1, the wave is referred to as a slow wave (slower than the speed of light $v_z < c$); when the ratio is less than 1, the wave is referred to as a fast wave (faster than the speed of light $v_z > c$). The surface wave wavelength λ_z of slow waves is shorter than λ, and for fast waves longer than λ.

A surface wave is one that propagates parallel to the interface and decades vertically to it. This means that the phase constant β_x is zero resulting in $k_x = -j\alpha_x$ (pure attenuation) with α_x positive. Also a surface wave assumes that the wave extends indefinitely in the transverse direction so $k_y = 0$, referred to Figure 2.7. To meet the condition of (2.27), k_z is set to be a real with no attenuation in the direction of propagation and the following relation is obtained

$$\beta_z^2 = k^2 + \alpha_x^2 \tag{2.29}$$

or equivalently using (2.28)

$$\frac{\lambda}{\lambda_z} = \frac{c}{v_z} = \sqrt{1 + \left(\frac{\alpha_x \lambda}{2\pi}\right)^2} \tag{2.30}$$

from which it follows that this is a slow wave. These types of slow surface waves ($v_z < c$) are used in the design of end fire antennas. Figure 2.8 illustrates the amplitude and phase fronts which are $90°$ from each other assuming that the medium above the interface is lossless (e.g. air). The closer the surface phase velocity (v_z) approaches the speed of light (c), the smaller the attenuation (α_x) and the larger the vertical extent of the surface wave in Figure 2.8.
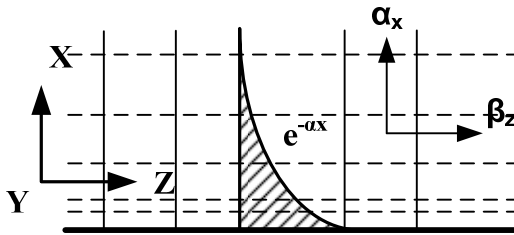
Figure 2.8 - Constant phase (β) and amplitude (α) contours of a plane surface wave. The surface wave propagates on an arbitrary interface in the Z direction with the field decaying in the X direction. The solid line represents the constant phase front, the shaded line the constant amplitude front, and the shaded region shows the amplitude decay.

All components of the total electromagnetic field of the surface wave for E_z are of the form

$$E_z(x,z,t) = E_z e^{-\alpha_x x} \cdot e^{-j\beta_z z} \cdot e^{j\omega t} \qquad (2.31)$$

The vertical decay of the E_z, E_x and H_y components for the TM surface ($H_z = 0$) waves are shown in Figure 2.9 and the composite electric field lines over a full wavelength interval are in Figure 2.10. It can be seen that E_z is in phase with H_y and in phase quadrature with E_x. The first two components, H_z and H_y, carry all the power along the interface, while E_x and H_y form a vertically pulsating storage field, apparent as loops.
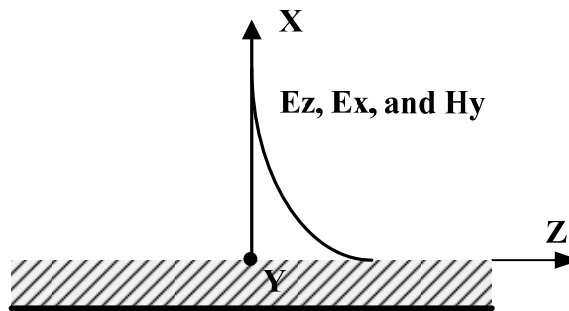
Figure 2.9 - Surface wave field structure above interface. TM wave component on plane surface.
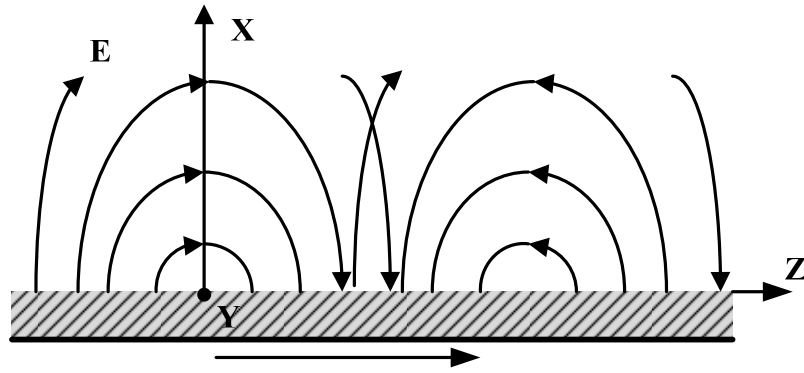
Figure 2.10 - Surface wave field structure above interface. Composite electric field lines over one wavelength interval. Z is the direction of propagation. The component of Ex and Hy form the vertically pulsating storage field.

2.3.1 Impact of Finite Ground Plane on the Radiation Pattern

The effect of a finite ground plane on the radiation pattern, for a surface wave antenna is next discussed. Vertically polarized surface wave line sources (Yagis) or areas sources are often mounted on a ground whose finite length g, as shown in Figure 2.11(a), distorts the antenna pattern into two ways: by tilting the beam with an angle ψ away from the end fire and by broadening the main beam to a half power beamwidth BW'.

The full half power beamwidth BW of the unperturbed pattern is

$$\psi_{max} \cong 60 \cdot \sqrt{\frac{\lambda}{\ell}} \qquad (2.49)$$

and is illustrated in Figure 2.11(b), which shows the area source antenna with an infinite ground plane (g = ∞). The beam tilt is maximum for g = 0, when there is no ground plane in front of antenna. In addition, the beam broadens so that the 3 dB level lies in the end fire direction as in Figure 2.11(c) and the perturbed beamwidth (BW') is twice as wide as the unperturbed beamwidth (BW). The tilt can be reduced by slowing down the surface wave from its optimum infinite ground plane. However this increases sidelobes and

23

reduces gain. The gain, on the other hand, is optimized by speeding the surface wave at the expense of increasing the tilt.

As g increases, towards an infinite ground plane, the beam tilt decreases. The beamwidth approaches the unperturbed value when g = L, BW' = 1.25 BW [8]. Modifying the surface wave velocity again affects oppositely the beam tilt and gain. From this it is learned that if no beam tilting or loss gain can be tolerated, flush mounting on top of a finite ground must be avoided.
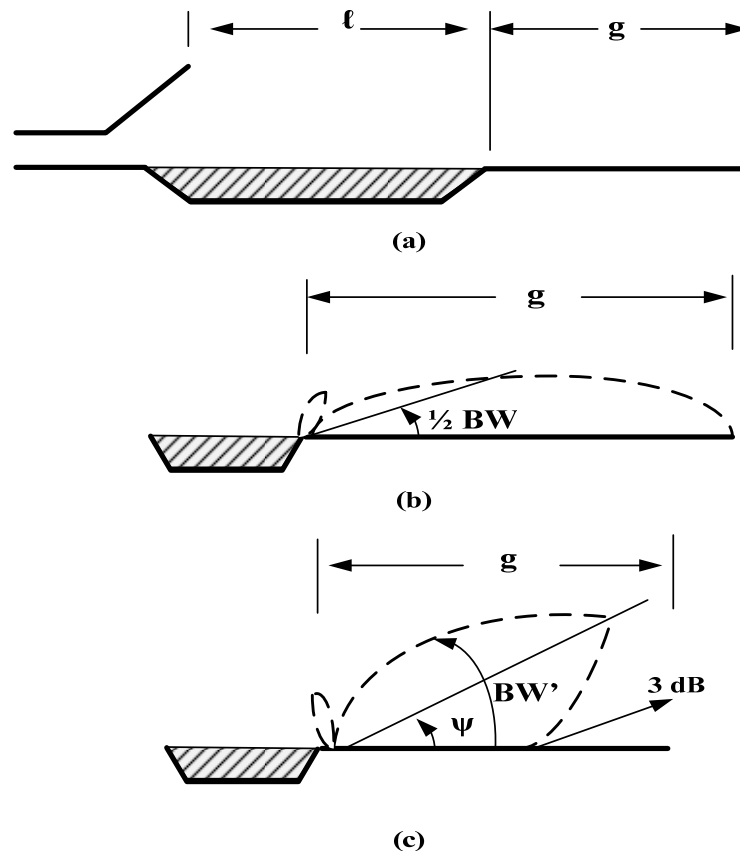
Figure 2.11 - Effect of finite ground plane on the radiation pattern of end fire antenna (e.g. area source represents the shaded region): (a) Finite ground plane. (b) Pattern on infinite ground plane, presents maximum beam tilt towards the end fire direction. (c) Pattern with no ground plane, BW' is broadens and the 3 dB point lies in the end fire direction.

2.4 Conclusion

In this review supporting information has been detailed which will facilitate the understanding of concepts presented in later this dissertation. A background study on array theory is prepared to define why an array of antennas is preferred over a single antenna to achieve a directional end fire pattern. The array pattern depends on the geometry of the array, separation between elements, excitation amplitude and phase of individual elements, and pattern of individual elements. The selected end fire array is the Yagi Uda array. This array offers simple feed by exciting only one element and using parasitic coupling to energize the rest. The Yagi-Uda radiator offers end-fire radiation by having the parasitic element in the front act as directors while those in the back act as reflectors. Finally a review has been offered on the properties of surface waves at the boundary between two media (dielectric/metal). The impact of a finite ground plane on the radiation pattern of an antenna is also explained, showing that the finite size for the ground plane results in a discontinuity which causes the surface waves from the ground plane to radiate onto the antenna, thus reducing the radiation efficiency. For an end fire antenna over a ground plane, the surface waves from the ground steer the main beam away from the end fire direction.

Chapter 3

A Quasi Yagi Antenna

3.1 Introduction

In this chapter we present a planar antenna array, the quasi Yagi antenna, with broadband characteristics and end fire radiation at the 2.4 GHz ISM band. This array is based on the conventional Yagi-Uda dipole array and was first realized by N. Kaneda in [9]. The planar design for this quasi Yagi antenna makes it suitable for current applications such as in aircraft wireless sensors systems, phased array radars, millimeter-wave imaging array systems and adaptive arrays for communications multiple beam communication systems.

Existing planar antenna arrays with broad band characteristics suffer from a variety of disadvantages for use in these applications. For example, microstrip patch antennas are inherently narrowband, although broad-band performance can be achieved through a multilayer design, an aperture coupled patch antenna [10], this approach experiences antenna complexity, manufacturing difficulties, and degraded backside radiation. In addition, the direction for the main beam pattern for a microstrip patch antenna is oriented in the broadside direction when the desired direction for this research is end fire. A second example, based on slot antennas, require additional design considerations and structural complexities such as using cavities or reflectors to overcome bidirectional radiation [11]. Additional end fire candidates are traveling wave antennas such as the Vivaldi and linearly tapered slot antennas (LTSA) which can

achieve a broad bandwidth. Unfortunately these antennas present large size, suffer from the excitation of unwanted substrate modes, experience strong cross talk in an array environment which perturbs the overall radiation pattern. In addition, the frequency response of a tapered slot antenna is affected by the complexity of the feeding network, microstrip to slot or coplanar waveguide to slot.

An improvement brought in by the quasi Yagi antenna is that it adapts the classical Yagi Uda configuration for operation at microwaves frequencies, and in addition introduces the compactness of resonant type antennas and the broadband characteristics of travelling wave antennas. The arrangement of the quasi Yagi antenna consists of an array dipoles printed on a high permittivity substrate (ε_r=10.2) where one of its elements (driver) is fed by a microstrip to coplanar strip (CPS) transition. The main feature introduced by this design is the used of the truncated ground plane from the feed network as the reflecting element. This trait eliminates the need for an additional reflecting dipole, resulting in a more compact design ($< \lambda_0/2$) and also provides direct compatibility with microstrip circuitry. Further advantages inherent in the quasi Yagi design are mechanical support and planar transmission line compatibility due to the presence of a substrate. The use of a high permittivity substrate means that the antenna will be extremely compact in terms of free space wavelength (λ_0).

In this chapter detailed information is offer on the design and performance of a broadband quasi Yagi antenna at the 2.4 GHz ISM band. The simulated antenna shows 10 dB return loss bandwidth extending from 1.95 - 3.17 GHz (1.22GHz, 49%), front to back ratio of 17 dB, cross polarization level of -18 dB and moderate gain of 4.6 dB. Also a study is carried on the impact the director adds to the quasi Yagi configuration. The

results showed that the director adds minimum effect to the return loss bandwidth and the end fire pattern. Finally, a ground metal shielding is included under the radiating elements, the results demonstrate that the addition of this shield degrades the overall return loss bandwidth and steers the beam to the broadside direction.

3.2 Quasi Yagi Antenna

The quasi Yagi antenna (Figure 3.1) is design on a single substrate (2.5 mm thick RT Duroid 6010 LM, $\varepsilon_r = 10.2$) with metallization on both sides. The top metallization consists of the microstrip transition, a broadband microstrip to coplanar strip-line balun (CPS) [12], and two dipole elements, the driver fed by the CPS transition and the parasitic director. The bottom metallization consists of the truncated ground plane for the microstrip transition which is the reflector element for the quasi Yagi.
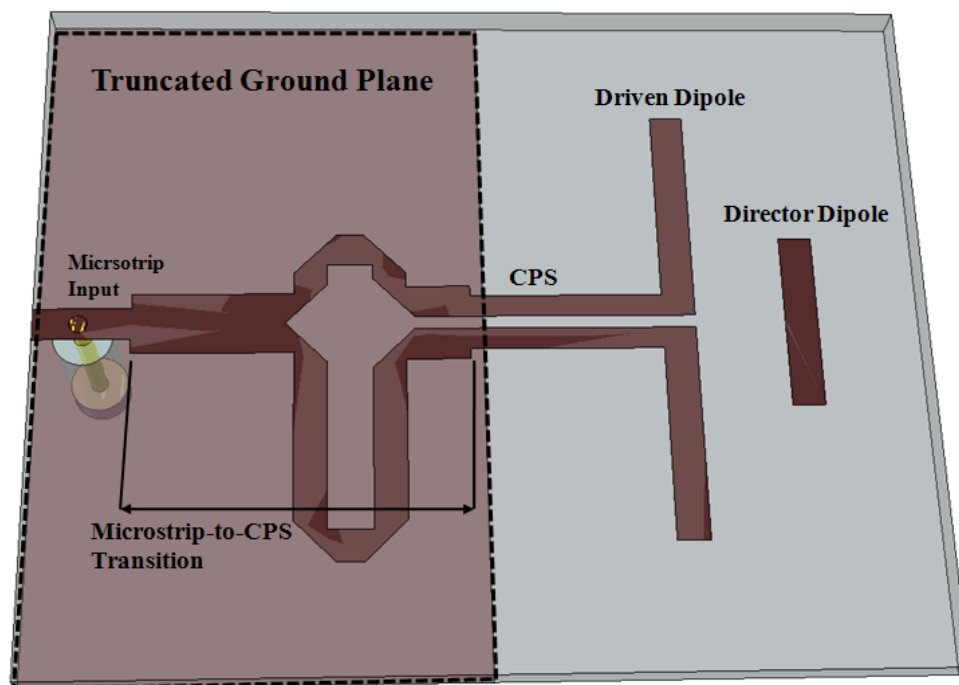
Figure 3.1 - Quasi Yagi Antenna.

The radiation of the quasi Yagi is a combination of free space and substrate radiation. The substrate radiation consists of the combination of a TE (transverse electric) and TM (transverse magnetic) polarized wave travelling through the media (ε_r = 10.2). For this wave the electric and magnetic field are perpendicular to each other, and both are perpendicular to the direction in which the wave travels. From the theory presented in Appendix A for wave propagation, a wave travelling though a guided dielectric slab presents TE_0 and TM_0 as the dominant modes, while for a grounded dielectric slab, TM_0 is dominant and TE_0 is cutoff. The TE_0 mode is cutoff in a grounded dielectric slab because the ground conductor forbids internal electric fields and continuity across the dielectric/air boundary, forcing the tangential electric field at the surface to zero.

The driven printed dipole generates a TE_0 surface wave with very little TM_0, minimizing cross polarization. The parasitic director enables impedance matching and directs the energy propagation towards the end fire direction. The driver and the director dipoles are strongly coupled by the TE_0 surface wave. The new feature introduced by this antenna is the use of the truncated ground plane as the reflector element. The truncated ground plane acts a reflector for the propagation of the TE_0 mode beneath the grounded dielectric slab region because the tangential component for the E field is zero at the boundary between the dielectric and the metal surface.

3.2.1 Derivation of the Balun

The balun for this antenna serves as a transition for a microstrip line and a coplanar strip-line (CPS) [12]. The microstrip lines at the input port as well as the two split arms to the CPS are all assumed to be 50Ω. The balun employs a quarter-wave long, 35.4Ω impedance transformer, followed by a symmetric Tee junction for signal dividing/combining, and miters for the 90° microstrip bends.

The quarter-wave transformer (Figure 3.2) is a section of transmission line, λ/4 long, used to match the input impedance of the Tee- junction ($R_L = 25Ω$) to the 50Ω input impedance of the microstip line. First, Z_{IN} is found looking into the λ/4 section by

$$Z_{IN} = Z_1 \frac{R_L + j \cdot Z_1 \cdot \tan \beta \ell}{Z_1 + j \cdot R_L \cdot \tan \beta \ell} \tag{3.1}$$

where $\beta\ell = (2\pi/\lambda)\cdot(\lambda/4) = \pi/2$. Next, the limit $\beta\ell \rightarrow \pi/2$ is used in (3.1) and both numerator and denominator are divided by $\tan \beta\ell$ resulting in

$$Z_{IN} = \frac{Z_1^2}{R_L} \tag{3.2}$$

To find $Z_1 = 35.4Ω$, for $\Gamma = 0$ looking into λ/4 section, $Z_0 = Z_{IN}$ which yields

$$Z_1 = \sqrt{Z_0 R_L} \tag{3.3}$$
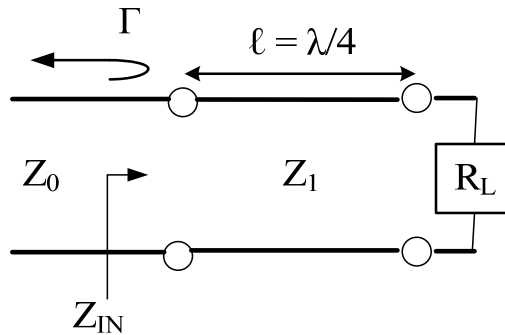
Figure 3.2 - The quarter-wave matching transformer used between the input microstrip line and the Tee junction section.

30

The symmetric Tee-junction line is a simple three port network used for power dividing/combining in any type of transmission line medium. The Tee-junction used here is assumed to be lossless, $B = 0$ in (3.4), and modeled by three transmission lines, Z_0, Z_1 and Z_2 as shown in Figure 3.3 [13].

$$Y_{IN} = j{\cdot}B + 1/Z_1 + 1/Z_2 + 1/Z_0 \tag{3.4}$$

$$1/Z_1 + 1/Z_2 = 1/Z_0 \tag{3.5}$$

Since equal power split is desired (3dB) for Z_1 and Z_2 (50Ω each), the input line must be 25Ω (Note: this is the output, $R_L = 25\Omega$, impedance from the quarter wave section).
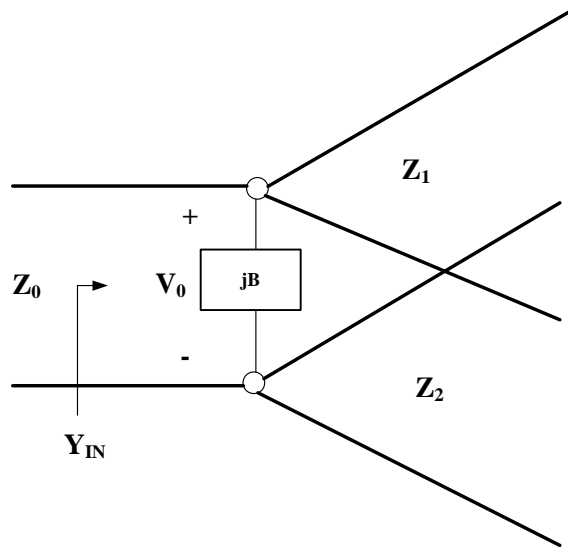
Figure 3.3 - Transmission line model for a lossless Tee-junction line.

Following the Tee-junction, a 180° phase delay is introduced to the microstrip section to balance the phase between the lines. This is achieved by adjusting the length of the arms so that their difference is $\lambda g/4$ (λ_g guided wavelength in the microstrip).

Next, the microstrip-to-CPS transition (Figure 3.4) is simulated to attest that equal power split is achieved for both arms of the transition. This simulation is analyzed in

Ansoft HFSS 11.2. At the CPS port, two modes are excited, the even and odd mode. The even mode is generated by the coupling between ground and a strip. The odd mode is produced by the coupling between adjacent strips. For the even mode, Figure 3.5, the electric field has even symmetry about the center lines and no current flows between the two strip conductors. For the odd mode, Figure 3.6, the electric field lines have odd symmetry about the center and a voltage null exist between the two conductors.
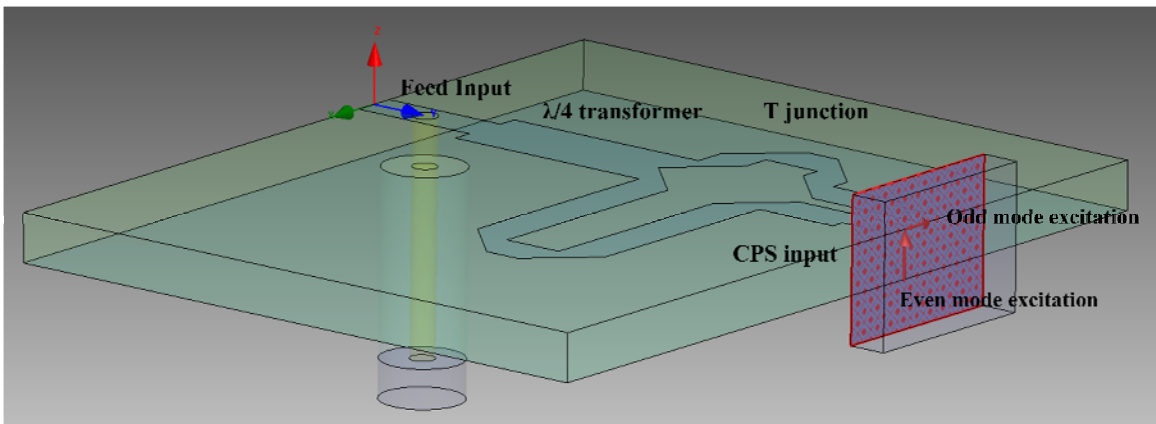
Figure 3.4 - Microstrip to CPS transition for the quasi Yagi simulated in Ansoft HFSS.
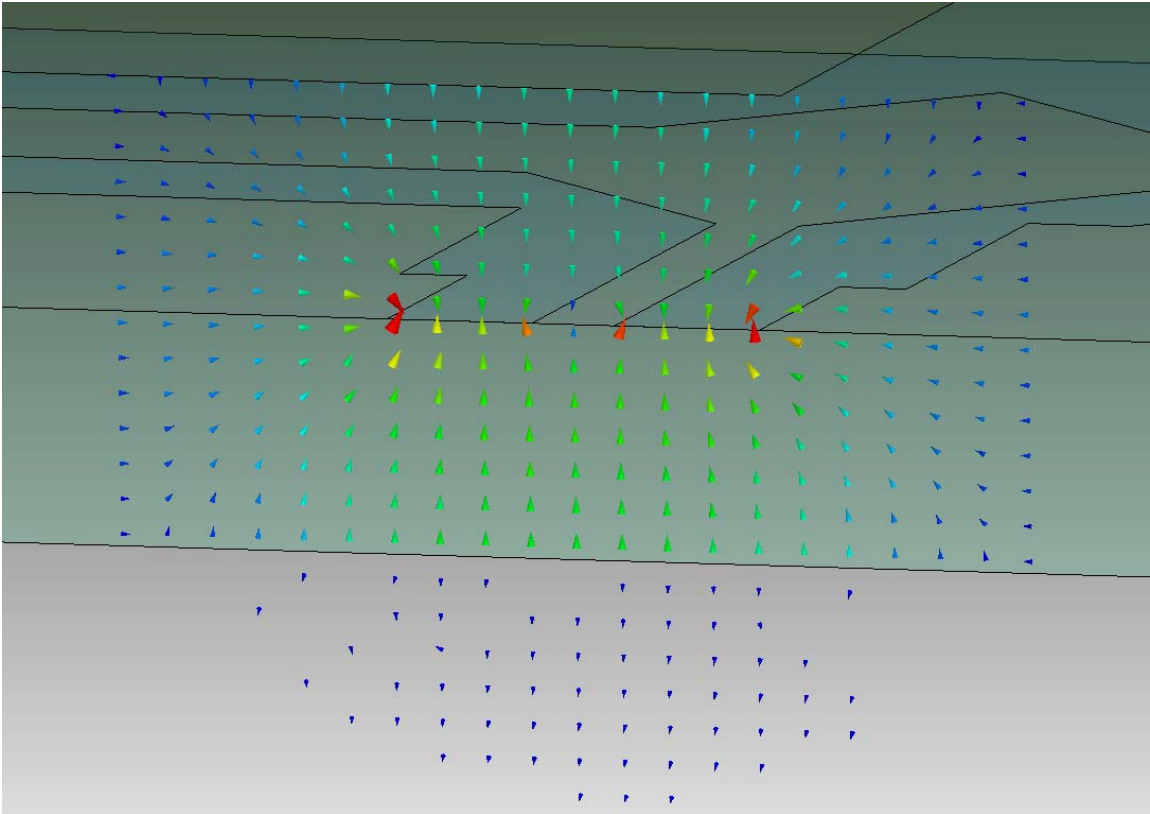
Figure 3.5 - Even mode symmetry.
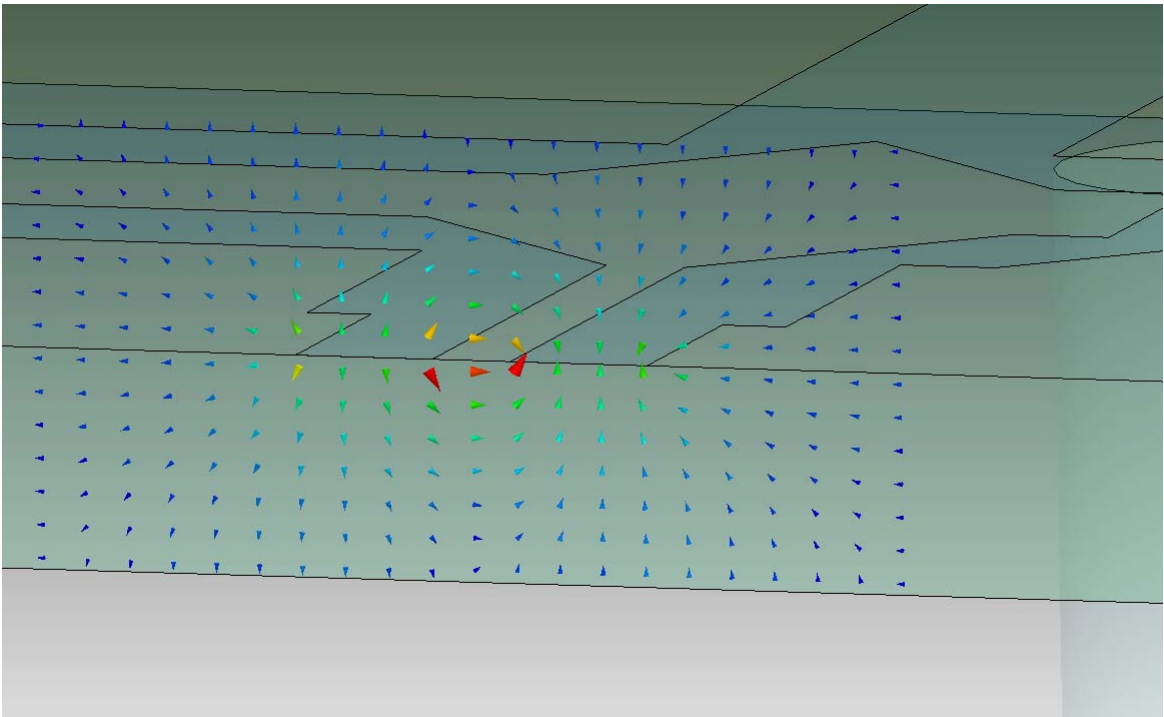
Figure 3.6 - Odd mode symmetry.

The simulation results for the microstrip-to-CPS transition displayed in Figure 3.7 demonstrate a satisfactory input match to the microstrip section and maximum power transfer through the delay lines to the CPS lines. The dimensions for the balun are listed on Table 3.1.
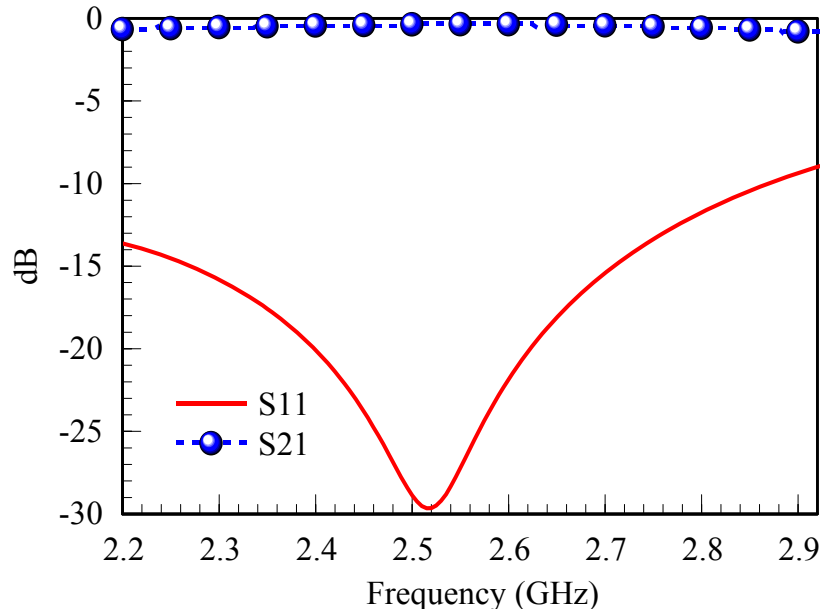
Figure 3.7 - S11 and S21 dB for the microstrip to CPS transition. S21 refers to the odd mode for port 2 in respect to port 1.

3.3 Simulation of the Quasi Yagi Antenna

Figure 3.8 illustrates the different parameters defining each dimension for the simulated quasi Yagi antenna and their corresponding values are listed in Table 3.1. The results for the simulated design are listed next and are compared to previous work from [14] to validate expected performance.

The results on return loss (Figure 3.9) present a broad bandwidth of 1.22GHz (1.95 – 3.17 GHz, 49%) for an S11 < -10 dB. The radiation pattern for the E and H plane of the quasi Yagi at 2.45 GHz are shown in Figure 3.10 and Figure 3.11 respectively. The co-polarized H-plane radiation in Figure 3.10 presents an end fire pattern (maximum at θ

= 90˚) with negligible cross polarization. The co-polarized E-plane pattern in Figure 3.11

demonstrates a directional pattern with 3 dB beamwidth of 91˚ and good radiation profile,

a front to back ratio of 17 dB and cross polarization -18dB. The achieved front to back

ratio is the result of the back reflector attenuating the TE_0 mode in the grounded dielectric

slab region. The small level of existing cross polarization is a result of the dominance of

the TE_0 over the TM_0 for the slab region beneath the radiating elements. Furthermore, the

quasi Yagi also achieves a moderate gain of 4.6 dB over the ISM band as illustrated by

Figure 3.12. All of the simulated results present close comparison to previous work on

quasi Yagis by [14].
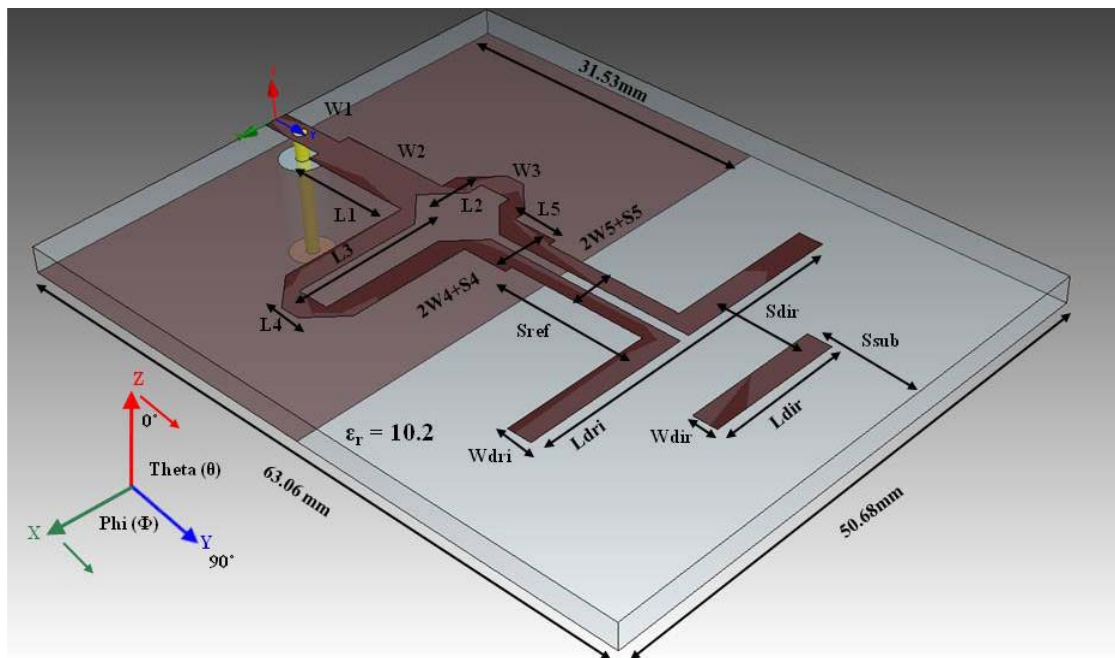
Figure 3.8 - Quasi Yagi Antenna.

Table 3.1 – Dimensions for the quasi Yagi antenna.

Antenna Element	Dimensions (mm.)
Microstrip Width (W1)	2.33
Length of 0.25λ transformer (L1)	11.3
Width of 0.25λ transformer (W2)	4.48
T-junction delay, L3-L2 = 0.25λg	16.32-5.66=10.66
Width on T-junction (W3 = W4)	2.33
Length on T-junction (L4)	5.49
Length on T-junction/CPS (L5)	5.66
T and CPS coupled section (S4 and S5)	0.9
Length of CPS (Sref)	14.76
Width of driver/director (Wdri, Wdir)	2.34
Length of Driver (Ldri)	32.5
Length of Director (Ldir)	12.87
Separation of driver and director (Sdir)	8.74
Separation of director/substrate (Ssub)	9
Height of substrate layer (H)	2.5
Length of ground under director (Lgnd)	31.53
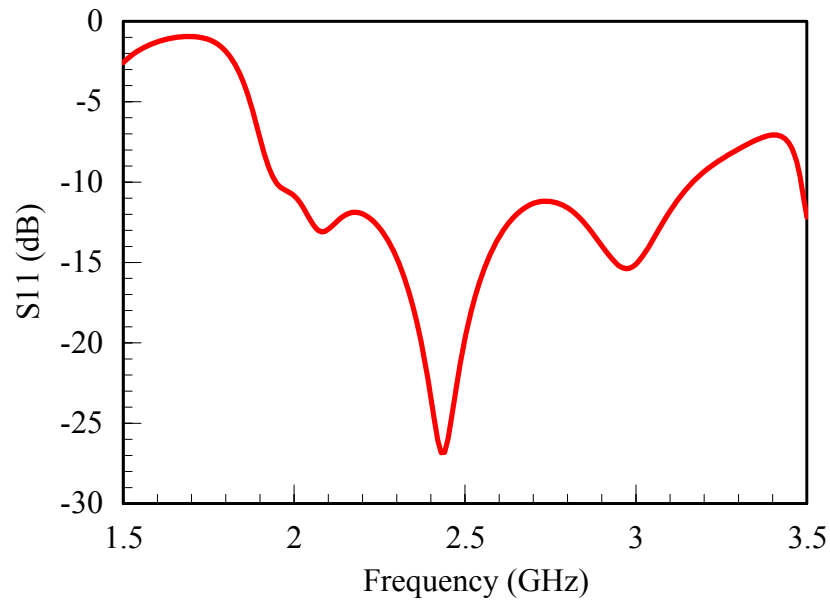
Figure 3.9 - Return loss (dB) versus frequency for simulated quasi Yagi antenna.

36
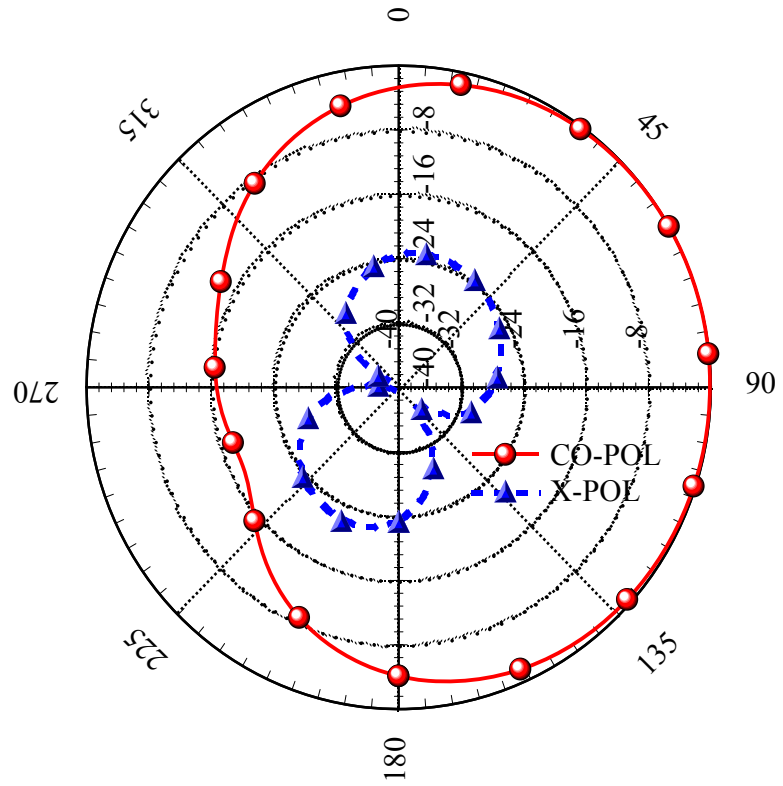
Figure 3.10 - H-plane radiation pattern for CO and CROSS polarization on the quasi Yagi antenna. Maxima for the pattern is in the end fire direction ($\theta = 90°$).
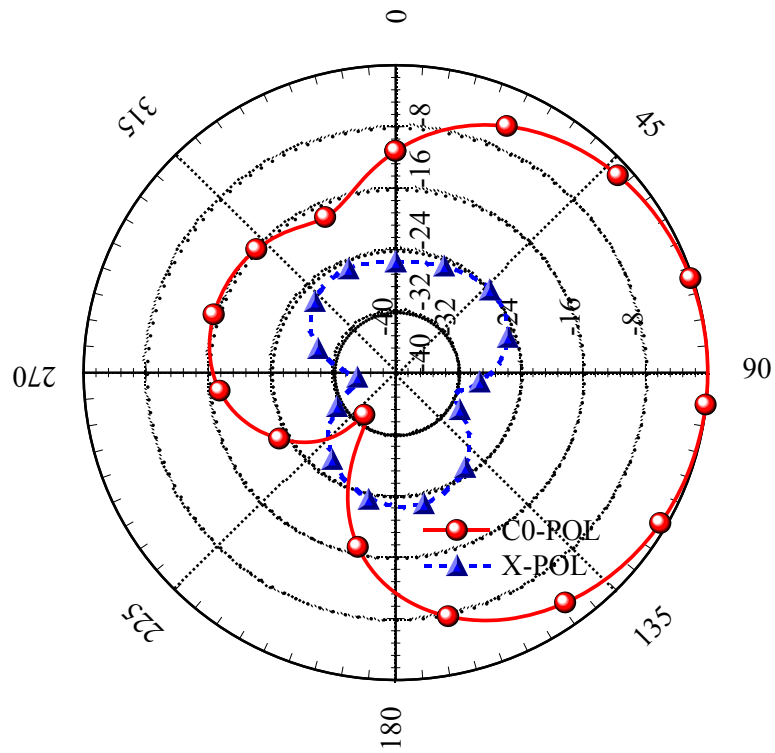
Figure 3.11 - E- plane radiation pattern for CO and CROSS polarization on the quasi Yagi antenna. Maxima for the pattern is in the end fire direction (Φ = 90˚). The recorded 3 dB beamwidth is 91˚.
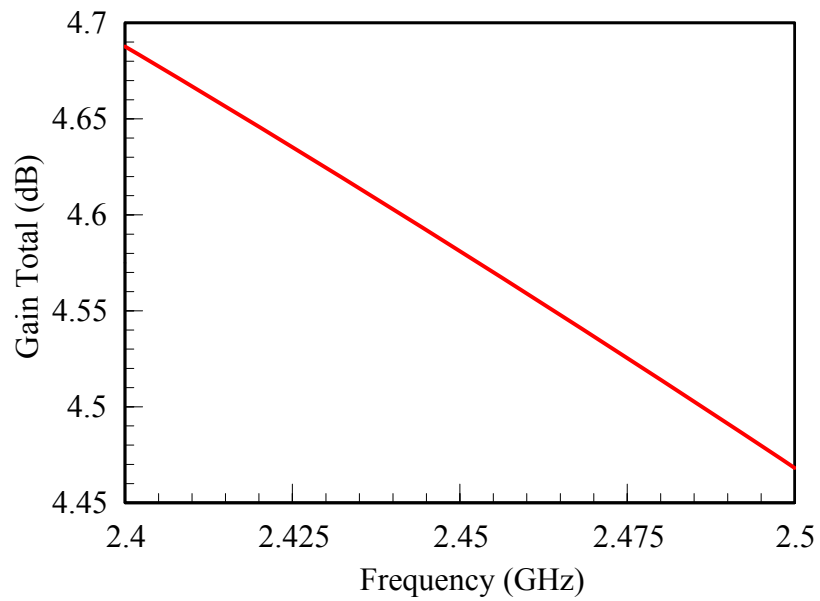
Figure 3.12 - Total gain versus frequency for quasi Yagi antenna.

3.3.1 Impact of Director on Quasi Yagi Operation

A study on the impact of having a director on the quasi Yagi configuration is prepared. The previous simulations on return loss and H-plane radiation pattern for a quasi Yagi including a director are compared to a design without a director. The results in Figure 3.13 for return loss exhibit slight variations on the overall bandwidth by using a director, except at around 2.78 GHz where the S11 dB is around -8.9 dB. The results from Figure 3.14 for the H-plane radiation pattern showed no difference on the main direction of the pattern by including a director. This suggests that the combined adjacent radiation between reflector and driver is sufficient to direct the main beam towards the end fire direction. Previous analysis on the director impact for a non grounded quasi Yagi has not been formally assessed.
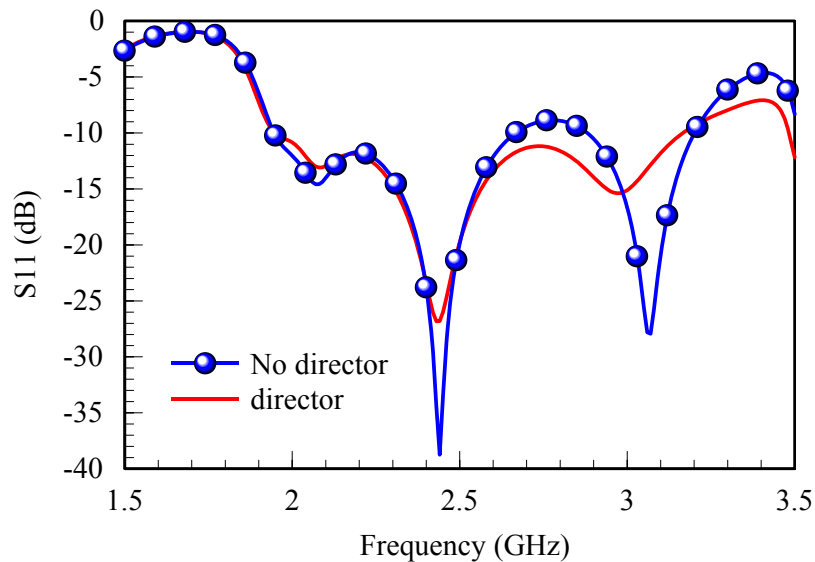
Figure 3.13 - Return loss for a quasi Yagi with director vs. no director.
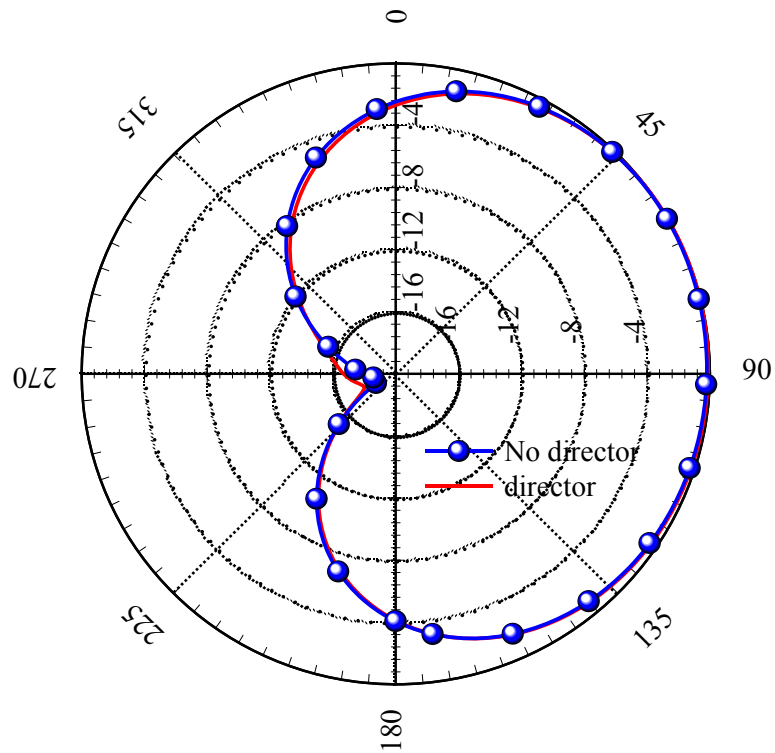
Figure 3.14 - H-plane pattern for quasi Yagi at 2.45 GHz with and without a director.

3.3.2 Simulation of Quasi Yagi with Metal Backing

For many planar antenna applications a metal backing is usually included to aid radiation characteristics by directing half of the radiation in opposite direction (from metal) and shielding object from interferences from the other side (bottom of antenna). This is the case for some applications, such as in wireless sensors networks, where the quasi Yagi antenna requires metal shielding from back interferences as a result of the location in which it will be operating (e.g. as lid of a sensor node). Thus, a simulation is prepared to study the effect that this metal backing has on the return loss and H-plane radiation pattern for the quasi Yagi. Figure 3.15 shows the overall bandwidth is degraded while Figure 3.16 demonstrates that the main beam has been completely steered away from the end fire direction ($\theta = 90°$) to the broadside direction ($\theta = 0°$). This destructive

40

interference added by this ground metal is a result of the currents on the quasi Yagi antenna being canceled by the image or reflecting currents from the ground metal. In other words the traveling wave returning from the ground plane adds 180˚ phase shit to the wave from the antenna radiating into free space.
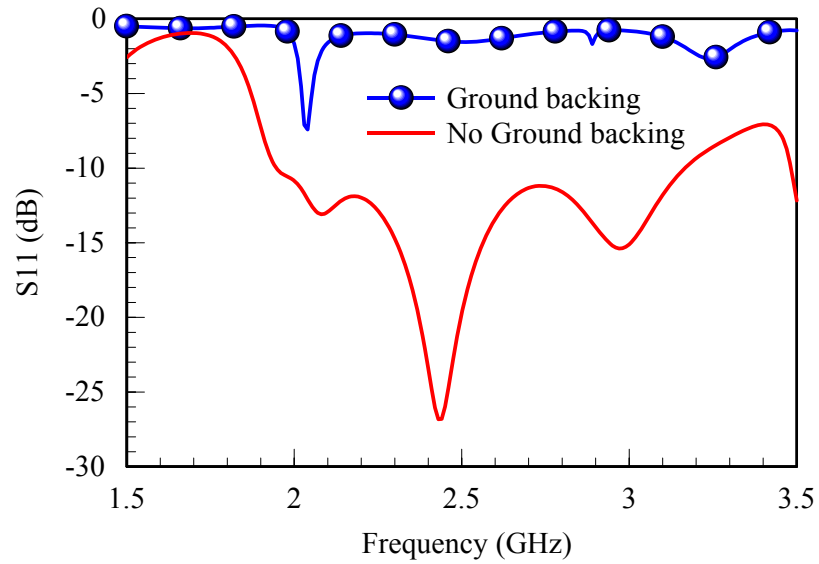
Figure 3.15 - Simulation result on return loss describing the shorting effect to the antenna added by a metal backing under its radiating elements.
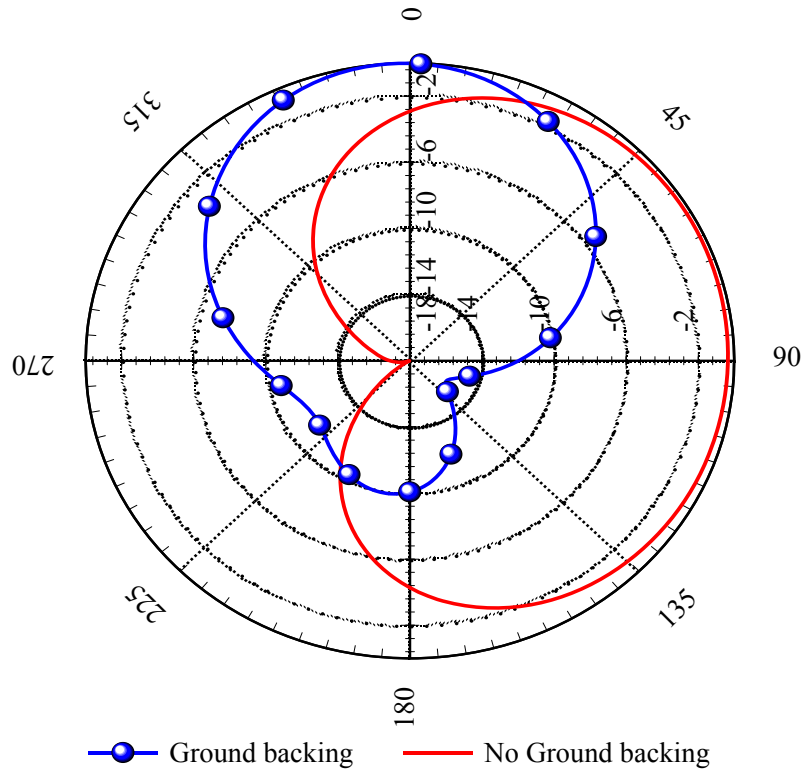
Figure 3.16 - Simulation results on H-plane pattern for the quasi Yagi with metal backing. The reflecting metal tilts the beam to the broadside direction ($\theta = 0°$).

3.4 Conclusion

A quasi Yagi antenna with broadband characteristics and end fire radiation at the 2.4 GHz ISM has been demonstrated. The simulation results show ample return loss bandwidth from 1.95 to 3.17 GHz (49%), an end fire radiation pattern with a front to back ratio of 17 dB and a cross polarization level of -18 dB. A simulation is also included to assess the impact brought in by the director in the antenna configuration. The results show that the director adds minimum contributions to the performance, the overall bandwidth and end fire pattern remain the same. The truncated ground plane from the transition is extended under the radiating elements, director and driver. Next, a simulation is performed and the results show that adding a metal backing shorts out the return loss

42

bandwidth and cancel the end fire pattern by tilting the beam to the broadside direction.

This is the main challenge of this research and is address in later chapters

Chapter 4

A Quasi Yagi Antenna Backed by a Metal Reflector Using a Displacing Dielectric Slab

4.1 Introduction

In this chapter a quasi Yagi antenna, as shown in [14], is implemented for operation in the 2.4 GHz ISM band. The intent of this design is to achieve an off-axis radiation pattern, with the main beam pointing away from the broadside direction, using an antenna that is packaged over a metallic ground. Such antennas generally exhibit poor radiation efficiency as a result of the image currents from the ground cancelling the antenna current [15], and broadside radiation due to the presence of the back metal surface. The work developed in this chapter addresses a solution to the problem presented by the ground plane. The solution consists of adding a substrate of suitable thickness, typically $0.25\lambda_g$, in order to adequately displace the ground. The substrate profile should be such that the reflecting waves from the ground metal add in phase with the waves radiated away from the substrate. The added substrate thickness is incorporated only under the radiating elements (driver and director) of the quasi Yagi antenna. A similar approach has been presented in [16] with the purpose of reducing mutual coupling between elements in an array configuration, however no formal design methodology or performance assessment was described.

In order to minimize the substrate profile, variations on the substrate thickness are applied and the effect of each thickness on the antenna performance is investigated. Substrate thicknesses ranging from $0.14\lambda_g$ (5.5 mm) to $0.25\lambda_g$ (9.7 mm) are studied, with

44

optimum operation achieved at $0.19\lambda_g$ (7.5 mm) thickness. A consequence of using a ground plane under the radiating section is the need to equalize the potential with the ground plane beneath the feed section using shorting vias. The positions for these vias are analyzed through simulation, and it is shown that via location can vary mid-band return losses between 15-30 dB.

Other options for an off-axis type radiator with metal backing have been reviewed, particularly the microstrip Yagi array [17]. A microstrip Yagi array consists of a linear array of patches made of a single driven element patch, a single parasitic reflector patch, and two director patches. The beam peak of this array can be tilted away from the broadside direction and towards the end fire direction due to the mutual coupling between elements and Yagi-Uda principles. Previous research presented in [17] showed that microstrip Yagis offer flexibility on beam steering over a ground plane, showing maximum beam peak of 35° from the normal direction with 3dB beamwidth between 5° to 55°, high efficiency, and gain of approximately 8dBi. Unfortunately, this array is not suitable for this research due to its relatively large physical size at the desired frequency (2.4GHz) and the dependence of patch coupling on substrate material. For instance, if the selected dielectric constant is too high, for example greater than five, the patch size is small but the separation between patches remains large in order to hold a $0.35\lambda_0$ separation; consequently the coupling energy between patches is insufficient to hold Yagi like operation.

The following sections offer a background review on the existing boundary conditions at the interface between the dielectric and ground, explain wave reflection principles for waves traveling through a lossless and lossy media, describe the

characterization of the antenna design, reveal the importance of the director dipole for this particular design, list results for a study on variations of substrate thickness and shorting via location, and compare simulated to measurement data.

The realized quasi Yagi antenna provides a 10 dB return loss bandwidth extending from 2.36 GHz to 2.55 GHz, beam angle displacement from 26 ˚ to 50˚ for substrate heights of $0.14\lambda_g$ (5.5 mm) to $0.25\lambda_g$ (9.7mm), directivity of 5.1 dB and efficiency of 89%. The coaxial feed and the inclusion of a ground plane are used to facilitate integration and for shielding.

4.2 Background Theory

This section explains the behavior of the electric and magnetic fields at the boundary interface between the dielectric and ground beneath the antenna [18]. The boundary conditions at the interface between two media are controlled by the tangential and normal component for the electric (E) and magnetic (H) fields. The tangential component for the E field is zero at the boundary while the normal component changes by a factor equal to the surface charge density (ρ_s). The H field is complementary to the E field, as the normal H field component is zero at the boundary and the tangential component is equal to the surface current density J_s.

The theory of wave reflection is reviewed for a wave traveling into the grounded dielectric slab region beneath the dipole elements of the quasi Yagi. As the wave travels through the substrate and arrives at the lower ground, it is reflected back with a phase reversal of 180˚. The 180˚ phase shift adds a destructive interference to the wave from the quasi Yagi travelling into free space. Fortunately, this destructive interference can be eliminated by displacing the ground metal away from the dipole elements by a certain

distance, usually $0.25\lambda_g$, which provides a wave reflection in phase or 0° phase shift towards free space. Furthermore, thinner substrates thicknesses are also evaluated to find the minimum substrate height, smaller then $0.25\lambda_g$, for which the ground shorting can be eliminated.

4.2.1 Boundary Conditions

Boundary conditions specify how the tangential and normal component of the field in one medium are related to the components of the field across the boundary in another medium [18]. For this work, the tangential and normal components for the E and H fields are derived at the interface of two media, a dielectric (medium1 - ε_1) and a conductor (medium2 – ε_2).
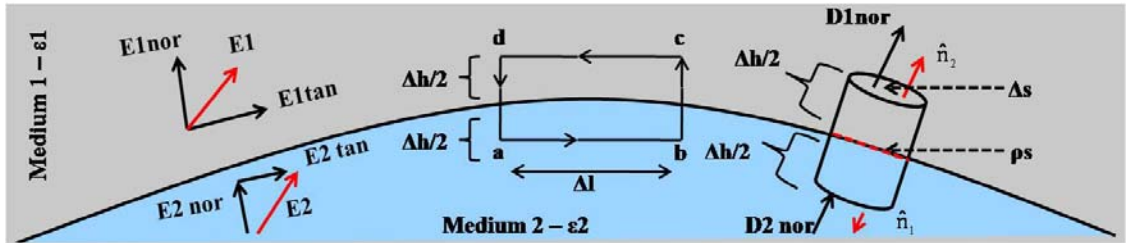
Figure 4.1 - Interface between two dielectric media, (medium 1 – ε_1) vs. (medium 2 – ε_2).

To derive the boundary condition for the tangential component of the E field, a closed rectangular loop abcda (Figure 4.1) is constructed and the conservative property of the electric field is applied on this loop. This property states that the line integral of the electrostatic field around a closed path is always zero. By letting $\Delta h \rightarrow 0$, the line integrals from segment bc and da go to zero. Resulting in

$$\oint_C E \cdot dl = \int_a^b E_2 \cdot dl + \int_c^d E_1 \cdot dl = 0 \qquad (4.1)$$

47

where E_1 and E_2 are the electric fields in dielectric and conductor. Since for a conductor, $E_2 = 0$, only E_1 is considered. In terms of the tangential and normal direction, E_1 is illustrated in Figure 4.1 as the vector addition of

$$E_1 = E_{1tangential} + E_{1normal} \tag{4.2}$$

From the previous E field property, over segment cd, $E_{1tangential}$ and dl have opposite directions, consequently (4.1) writes as

$$E = - E_{1tangential} \cdot \Delta l = 0$$

$$E = E_{1tangential} = 0 \ (V/m) \tag{4.3}$$

which concludes that the tangential component of E is zero across the boundary between the two media.

To determine the boundary conditions for the normal component of the E field Gauss's law is implemented. This law states that the total outward electric flux D through the three surfaces of the small cylinder in Figure 4.1 must equal the total charge enclosed in the cylinder. By letting $\Delta h \rightarrow 0$, the contribution from the side surface is zero and the only charge distributed is the charge on the boundary. Thus, $Q = \rho_s \Delta_s$ and by including the conductor property $D_2 = 0$ Gauss's law is written as

$$\oint_S D \cdot ds = \int_{top} D_1 \cdot \hat{n}_2 ds = \rho_s \Delta_s \tag{4.4}$$

where $\hat{n}_2$ is the outward normal unit vector from the top surface.

$D_{1normal}$ is defined as the normal components for D_1 along $\hat{n}_2$ so (4.4) is

$$D = \varepsilon_1 \cdot E_{1normal} = D_{1normal} = \hat{n}_2 \cdot \rho_s \ (C/m^2) \tag{4.5}$$

which states the normal component of E_1 at the boundary is equal to the surface charge density divided by the permittivity of the dielectric (ρ_s/ε_1).

48

In summary, the conservative property of E states that the tangential component of E is zero across the boundary while the divergence property of D states that the normal component of E is equal to ρ_S/ε_1 across the boundary.

Similarly to the procedure used to calculate the components for the electric flux D and E field, boundaries conditions are derived for the magnetic flux B and the magnetic field H. Applying Gauss's law for magnetism and $B_2 = 0$ in the conductor leads to (notice that the derivation of B is analogous to D)

$$\oint_S B \cdot ds = 0 \Rightarrow B_{1normal} = 0$$

$$B = B_{1normal} = \mu_1 H_{1normal} = 0 \tag{4.6}$$

which defines the normal component of H as been zero across the boundary

When comparing the normal component of H in (4.6) versus the previous derived normal component of E in (4.5), the normal component of H is zero across the boundary while the normal component of E is not, unless $\rho_S = 0$. A similar but opposite behavior applies to the tangential component of the E and H field. While the tangential component of the E field is zero across the boundary the H field component is not, unless the surface current density (J_S) is zero.

To obtain the boundary condition for the tangential component of H, Ampere's law is applied to the sides Δl and Δh on the close abcd rectangular path in Figure 4.2. Letting $\Delta h \rightarrow 0$ and $H_2 = 0$ results

$$\oint_C H \cdot dl = \int_c^d H_1 \cdot dl = I \tag{4.7}$$

where H_1 is the magnetic field in the dielectric. For the direction of H_1 in Figure 4.2, the tangential component of H_1 is anti-parallel to dl over segment cd. Since $\Delta h \rightarrow 0$ the

surface of the loop approaches a thin line of length Δl, and as result the total current flowing through the line is $I = J_S \Delta l$. J_S is the magnitude of the normal component of the surface current density traversing the loop. Substituting the tangential component of H_1 and J_S into (4.7) gives

$$H = - H_{1\text{tangential}} \Delta l = J_S \Delta l$$

$$H = H_{1\text{tangential}} = - J_S \; (\text{A/m}) \qquad (4.8)$$

and the tangential component of H is equal to J_S
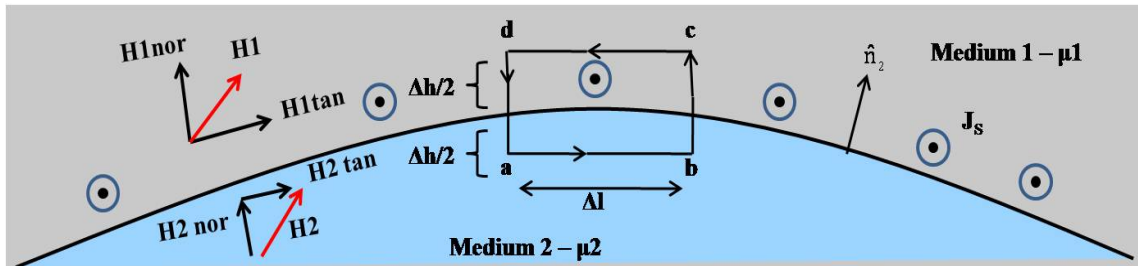
Figure 4.2 - Interface between two dielectric media, (medium 1 – μ_1) vs. (medium 2 – μ_2).

4.2.2 Wave Reflection between Media

This section discusses the TEM field solution between two semi-infinite lossless and lossy media bounded by a planar boundary of infinite extent [19]. The reflection coefficient is derived to account for the reflection of the fields at the boundary and is a function of the wave direction (β) and the direction of the E and H fields. The reflection coefficient is generally a complex quantity where its amplitude and phase can be varied by controlling the direction of the travelling wave or the angle of incidence.

When a wave impinges at the interface between two dissimilar media, part of the incident wave is reflected back to the first medium while another part is transmitted through the second medium. This wave can propagate with a normal angle of incidence through the interface as shown in Figure 4.3 or with an oblique angle of incidence as

shown in Figure 4.4 and Figure 4.5. For normal incidence ($\theta_i = 0°$), the reflection coefficient (Γ) at the boundary between two different media is independent of the polarization of the incident wave, as illustrated in Figure 4.3 the E and H fields are both always tangential to the boundary regardless of the wave polarization. This is not the case for oblique angle of incidence, $\theta i \neq 0°$. A wave with any specified polarization can be described as the superposition of two orthogonally polarized waves, one with the E field perpendicular to the plane of incidence, Figure 4.4, and another with the E field parallel to the plane of incidence, Figure 4.5. The plane of incidence (x-z) is the plane containing the normal to the boundary and the direction of propagation of the incident wave (β). Polarization with the E field perpendicular to the plane of incidence is also known as transverse electric (TE) polarization. When the E field is parallel to the plane of incidence the polarization is called TM polarization, in this case the H field is perpendicular to the plane of incidence.
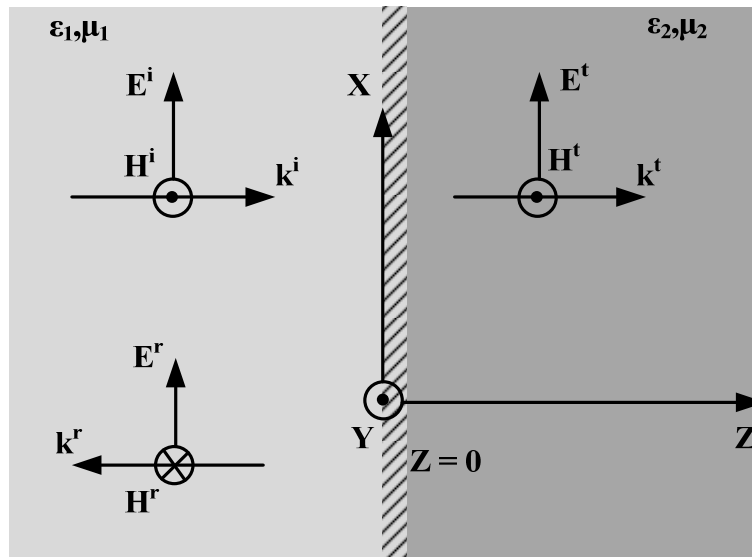
Figure 4.3 - Wave reflection and transmission at normal incidence for the interface of two media.
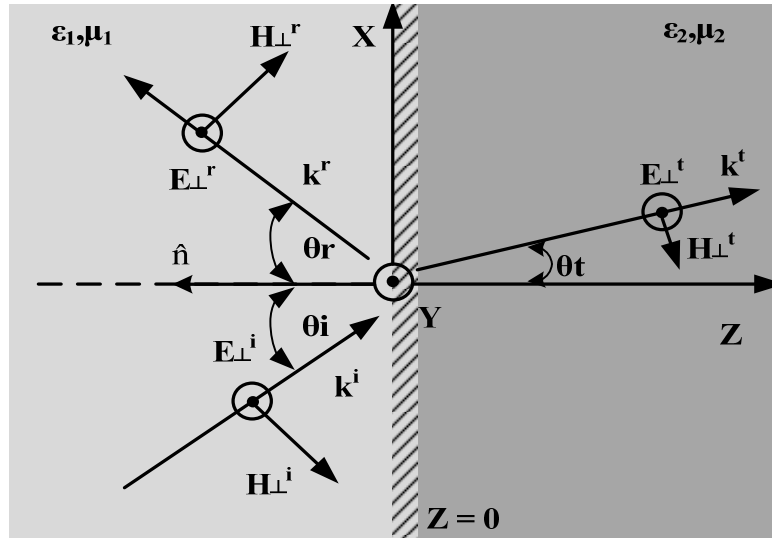
Figure 4.4 - Perpendicular (TE) polarized uniform plane wave incident at an oblique angle on an interface.
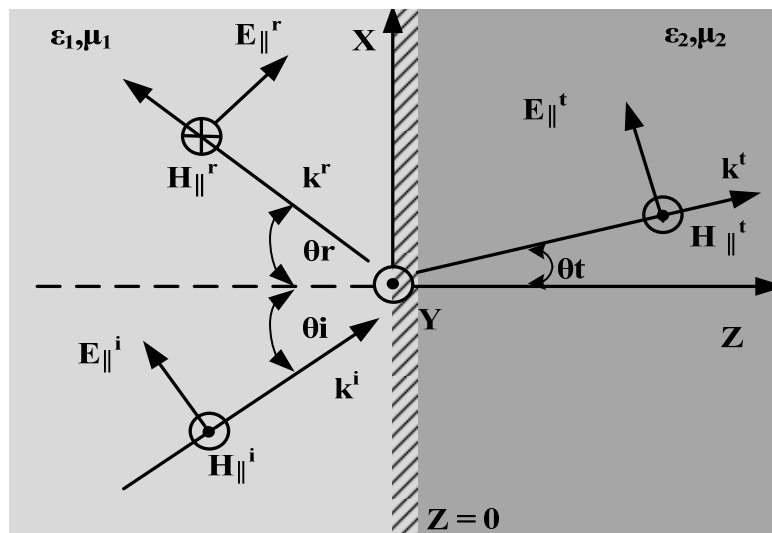
Figure 4.5 - Parallel (TM) polarized uniform plane wave incident at an oblique angle on an interface.

The previous background on wave reflection theory is used to calculate the reflection coefficient for an antenna lying flat on top of a dielectric and backed by a metal ground plane. For a plane wave with either normal or oblique incidence the ground metal reflects the wave with 180° of phase reversal. Since the ground metal backing is an excellent conductor (e.g. copper) as derived in (4.15) and its impedance is very small ($\approx$

0) as shown in (4.16), when the wave arrives at the metal boundary ($z = 0$ in Figure 4.6) the entire wave is reflected with a phase of 180° as calculated in (4.17).

If the substrate separating the antenna from the ground is very thin ($d = 0$), referring to Figure 4.6, the reflected wave at $Z = -d$ has a phase shift of 180° relative to the wave originating from the antenna into free space. As a result the ground metal is effectively shorting out the antenna and adversely affecting its radiation efficiency.

$$\frac{\sigma}{\omega \varepsilon_2} = \frac{5.8 \times 10^7}{2\pi \times 2.45 \times 10^9 \times (\frac{10^{-9}}{36\pi})} = 4.26 \times 10^8 >> 1 \tag{4.15}$$

$$\eta_3 = (1+j)\sqrt{\frac{\pi f \mu}{\sigma}} = (1+j)\sqrt{\frac{\pi \times 2.45 \times 10^9 \times 4\pi \times 10^{-7}}{5.8 \times 10^7}} = 12 \cdot (1+j)\, m\Omega \tag{4.16}$$

$$\Gamma_L(z=0^-) = \frac{Z_{IN}(z=0^+) - \eta_2}{Z_{IN}(z=0^+) + \eta_2} = \frac{\eta_3 - \eta_2}{\eta_3 + \eta_2} = -1 = 1 e^{j\pi} \tag{4.17}$$
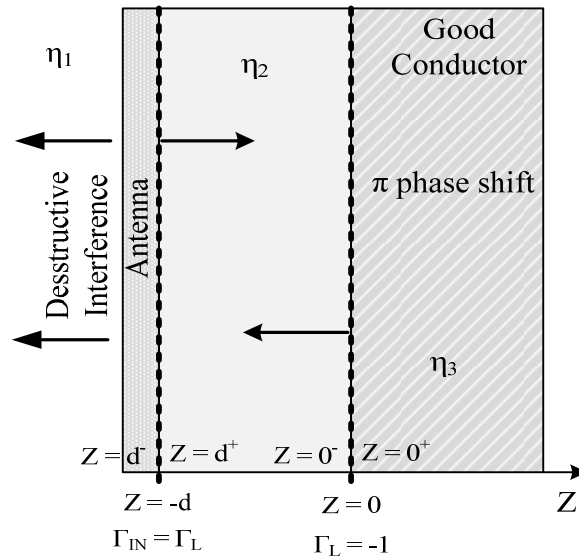
Figure 4.6 - Antenna laying flat over ground plane.

The ground destructive interference can be reduced by displacing the antenna one-quarter wavelength (d = 0.25λ_g) away from the ground (Figure 4.7). The total round trip phase shift from the antenna, to the metal, and back to the antenna, equals one complete cycle and the waves add constructively. In other words, at the antenna and dielectric boundary (z = d⁻), there is zero phase reversal and the ground plane appears like an open circuit to the antenna as shown in (4.19).

$$Z_{IN}(z=-d^+) = \eta_2 \left(\frac{1 + \Gamma_L(z=0^-)e^{-2j\beta d}}{1 - \Gamma_L(z=0^-)e^{-2j\beta d}} \right)$$

$$Z_{IN}(z=-d^+) = \eta_2 \left(\frac{1 + (-1)\cdot e^{-2j\left(\frac{2\pi}{\lambda}\right)\left(\frac{\lambda}{4}\right)}}{1 - (-1)\cdot e^{-2j\left(\frac{2\pi}{\lambda}\right)\left(\frac{\lambda}{4}\right)}} \right) \tag{4.18}$$

$$\Gamma_{IN}(z=d^-) = \frac{Z_{IN}(z=-d^+) - \eta_1}{Z_{IN}(z=-d^+) + \eta_1} = +1 = 1e^{j0} \tag{4.19}$$
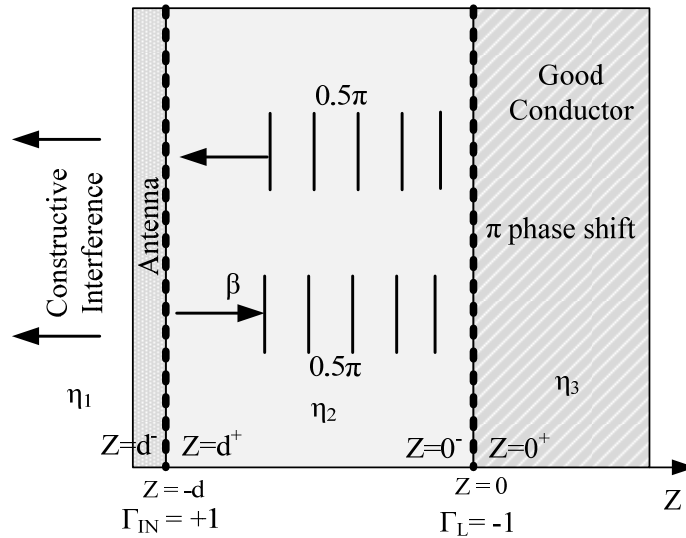
Figure 4.7 - Antenna separated by 0.25λ from ground plane.

A set of dielectric thicknesses, smaller than $0.25\lambda_g$, are evaluated to find a range of heights for which the reflected wave from the ground has minimum effect on the performance of the antenna. For simplicity, the incident wave is assumed to be normal to the surface, but in reality, this wave will also propagate at oblique angles of incidence. For this assessment the phase of the reflection coefficient from (4.19) is calculated for various values of substrate thickness (d). The minimum profile size is for a substrate thickness in which the phase of the reflection coefficient is $\leq 90°$, which corresponds to ~7.8mm ($0.2\lambda_g$) in Figure 4.8. Thus, the realized range of acceptable thicknesses extends from 7.8mm ($0.2\lambda_g$) to 9.7mm ($0.25\lambda_g$). The provided range is used as starting point for the simulations carried later on section 4.3.1 for the analysis of substrate thickness effect on antenna performance.
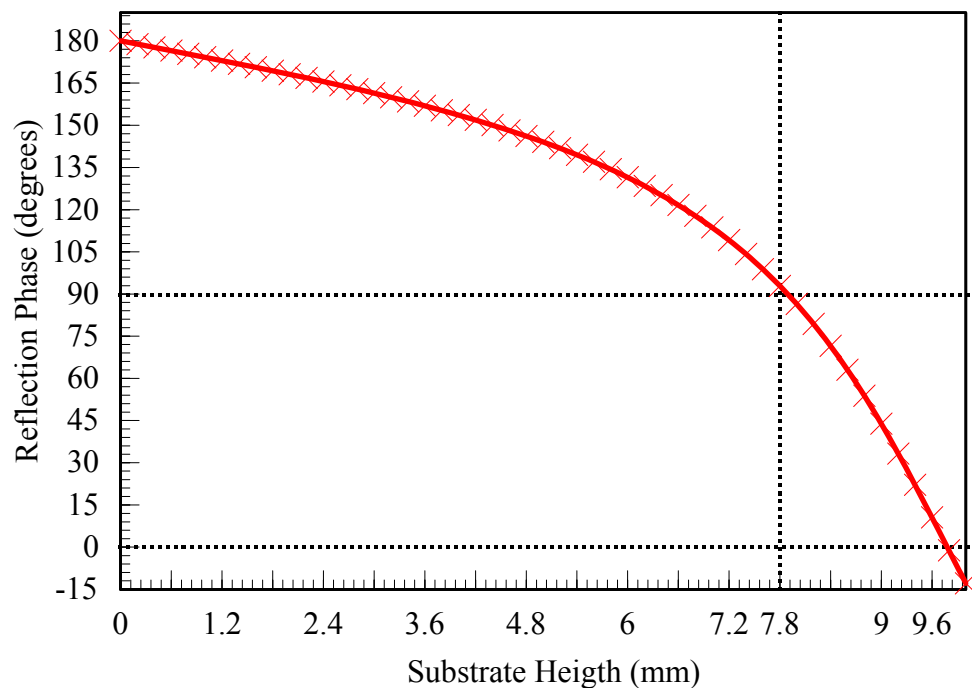
Figure 4.8 - Reflection phase (degrees) vs. substrate thickness (mm).

4.3 Design Characteristics

The substrate of interest in this work is the RT duroid 6010LM (ε_r = 10.2) with metallization on both sides. The top metal consists of a microstrip feed, a balun and the dipole elements. The bottom metallization consists of the microstrip ground and the ground beneath the dipole elements. These two grounds are connected through shorting vias.

The physical characteristics for the antenna presented in this section are derived from the conventional (non-grounded) design presented in [14] however the nature of electromagnetic field propagation is quite different. In the conventional design the TE_0 mode propagates in the non-grounded section underneath the dipoles and is reflected by the ground in the microstrip section; this behavior leads to a good front-to-back radiation ratio and low cross-polarization. On the contrary, for this quasi Yagi antenna there is no propagation of the TE_0 mode beneath the dipoles as a result of the grounded substrate. Consequently the propagating waves in the antenna section are a combination of free space waves and TM_0 surface waves. While the front-to-back ratio is lower than that of the conventional design, the step change in substrate height after the microstrip section does reduce the back-propagation of the TM_0 mode. The cut-off frequency for the first few TE and TM modes, assuming a 7.5 mm substrate, are listed in Table 4.1. These quantities are derived from (A.27) for the first two modes for TM and TE.

Table 4.1 - Cutoff frequency for selected modes.

Modes	Cutoff Frequency (GHz)
TM_0	0
TM_2	6.6
TE_1	3.3
TE_3	9.9

The dipole elements for a quasi Yagi antenna consist of the parasitic director and the driver. The driver dipole is the excited element of the array while the parasitic director enables impedance matching and directs the energy propagation towards the end fire direction. The presence of the ground and the step increase in substrate height affects the coupling between director and driver, requiring that the director spacing (Sdir) be modified relative to the non grounded design. The value for Sdir was initially based on the work presented in [20] and then refined using electromagnetic simulation in order to optimize the return loss; the final value was ~25% larger than that in [20].

The balun used to feed this antenna provides a microstrip to CPS transition. The main function desired from the transition is to achieve 180˚ phase delay between the two arms of the microstrip line. The delay is obtained by adjusting the length difference (L3-L2) to equal 0.25λ as shown in Figure 4.9.
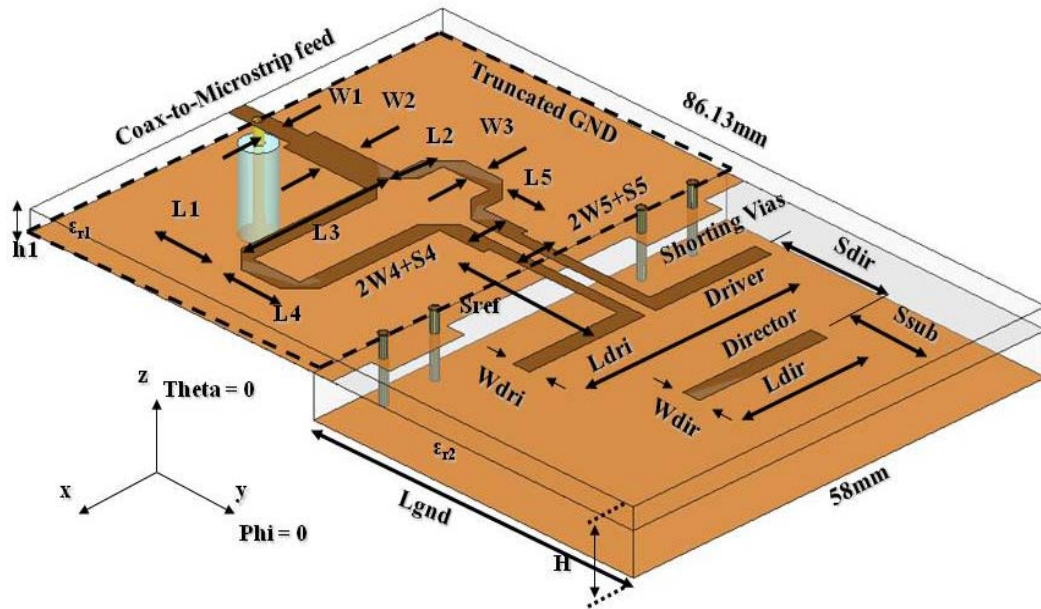
Figure 4.9 - Illustration of the quasi Yagi antenna with size and dimensions.

57

The overall size of the antenna is 58mm × 86mm. The dimensions for the elements of the quasi Yagi antenna, determined through simulations and optimization using ANSOFT HFSS10, are listed in Table 4.2.

Table 4.2 - Dimension of antenna elements.

Antenna Element	Dimensions (mm.)
Microstrip Width (W1)	2.34
Length of 0.25λ transformer (L1)	11.79
Width of 0.25λ transformer (W2)	4.47
T-junction delay, L3-L2 = 0.25λg	21-7=14
Width on T-junction (W3 = W4)	2.34
Length on T-junction (L4)	8.3
Length on T-junction/CPS (L5)	7.5
T and CPS coupled section (S4 and S5)	1.5
Length of CPS (Sref)	18.33
Width of driver/director (Wdri, Wdir)	2.34
Length of Driver (Ldri)	34
Length of Director (Ldir)	18
Separation of driver and director (Sdir)	16
Separation of director/substrate (Ssub)	10.83
Height of substrate layer (H)	7.5
Height of truncated section (h1)	2.5
Length of ground under director (Lgnd)	45.66

4.3.1 Impact of Substrate Thickness on Antenna Performance

Variations in the thickness of the metal-backed substrate under the dipole elements were investigated in order to understand the impact on several antenna performance parameters, namely the return loss, radiation pattern and cross-polarization level. The starting values for thicknesses are those from Figure 4.8. The results in Figure 4.10 indicate that the mid-band (2.45 GHz) return loss is >10 dB for thicknesses from 5.5mm (0.14λg) to 9.7mm (0.25λg). Figure 4.11, which describe return loss as a function of frequency for substrate heights of 2.5, 7.5 and 12.2mm, shows poor performance for

substrate heights at the low and high end of the range.
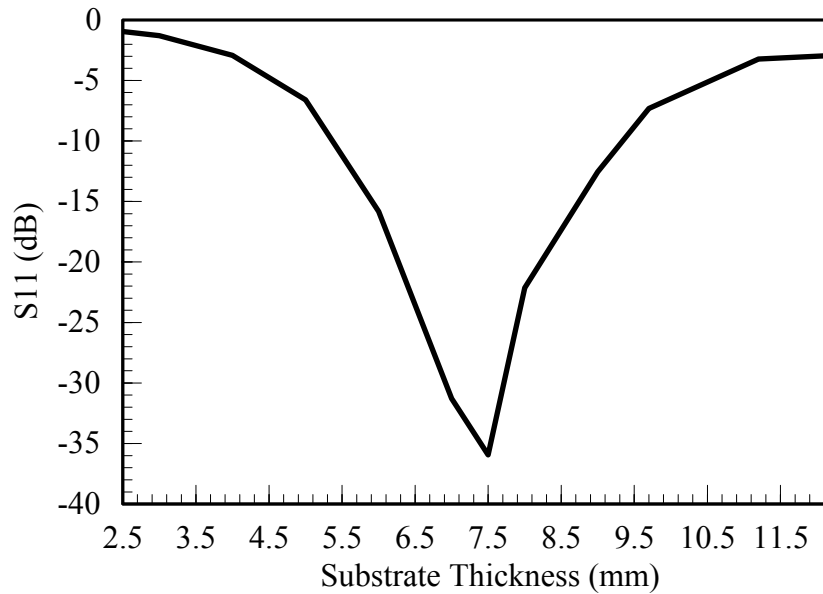
Figure 4.10 - Simulated return loss vs. substrate thickness (H) at 2.45 GHz.
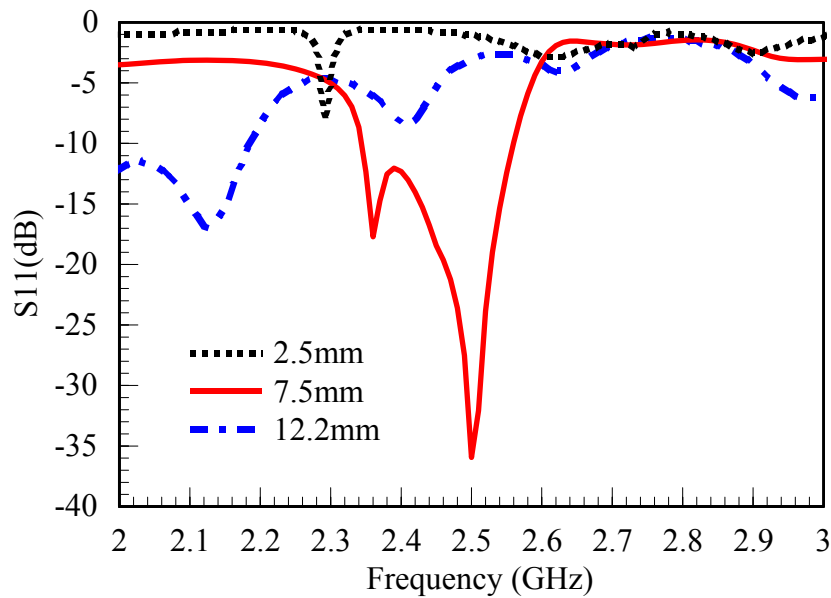
Figure 4.11 - Simulated return loss vs. frequency for selected substrate thickness.

The relationship between substrate height and H-plane radiation pattern ($\phi = 0°$) is

illustrated in Figure 4.12. The simulation results demonstrate that an increase in substrate

59

thickness causes the beam to steer towards the horizon and the peak gain to decrease. For a thickness of 5mm the beam is steered to 26˚ with a gain of 5 dB, for a thickness of 7.5mm the beam is steered to 42˚ with a gain of 4.93 dB, and for 9.7mm (0.25λg) the beam is steered to 50˚ with a gain of 0.07dB. The observed decrease in gain in the forward direction for the 9.7 mm thickness is accompanied by a flattening of the beam in the E-plane, with the peak gain shifting toward the $\phi = \pm 90°$ direction.
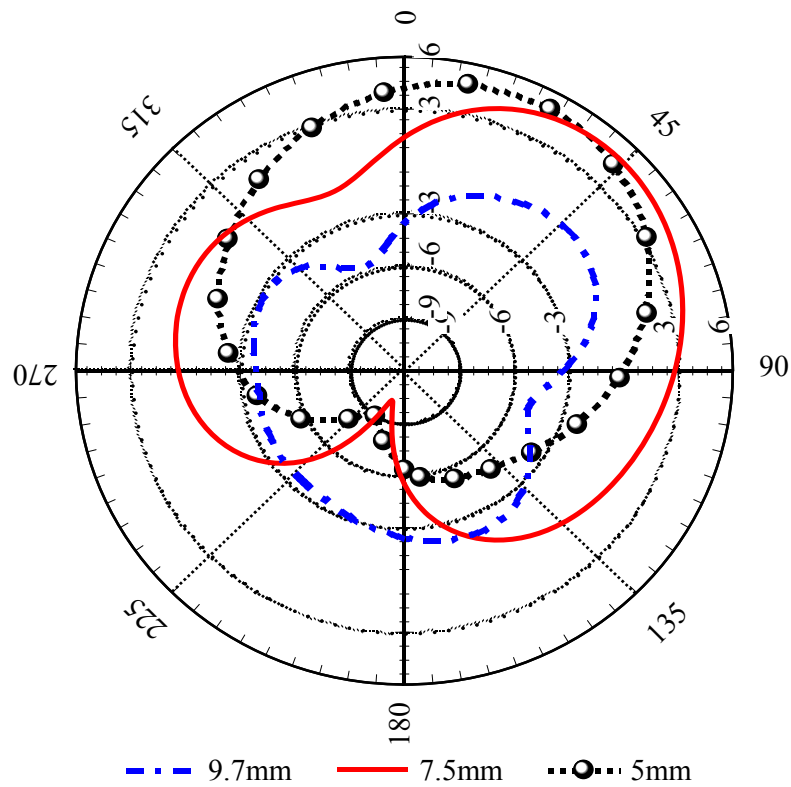
Figure 4.12 - Simulated H-plane gain vs. substrate height at 2.45 GHz. The scale ranges from -9 dB to 6 dB in step of 3 dB.

Finally, the impact of substrate height on cross-polarization for the E-plane ($\theta = 90°$) is presented in Figure 4.13. The patterns show that as the height of the substrate increases the cross-polarization also increases. The increase in cross polarization is predominantly a result of the TM_0 that propagates between the driver and director. The

relatively high cross-polarization, compared to a conventional quasi Yagi antenna, is not a primary factor in this design as the antenna is intended for operation in a multipath-rich environment.
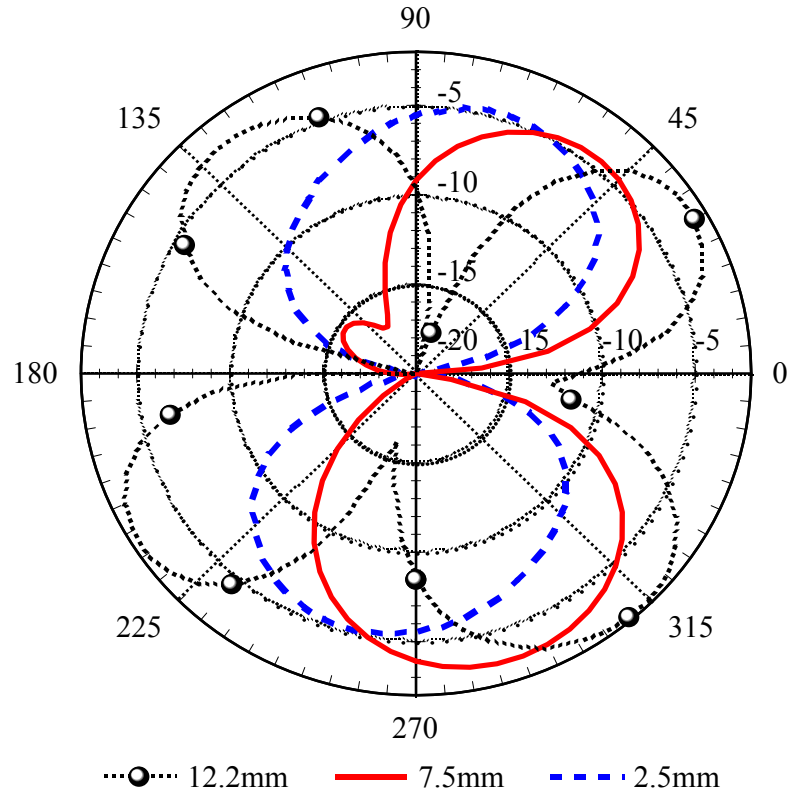
Figure 4.13 - Simulated E-plane cross-polarization gain as a function of substrate height at 2.45 GHz.

4.3.2 Impact of Shorting Via Placement

In this section a parametric analysis to study the impact of the location of via holes on return loss and radiation pattern is summarized. The shorting vias were used to connect the ground under the microstrip section to the ground beneath the dipole elements. The vias were shifted from the center of the board (0 mm) to the connector edge of the board (27.2 mm), Figure 4.14. As the vias were moved towards the connector edge the extension of the thick substrate and back metal were increased correspondingly.

The results on return loss and radiation pattern (H- plane pattern) for the different via positions are illustrated in Figure 4.15 and Figure 4.16, respectively. Figure 4.15 shows a return loss of 30 dB for via holes located in the center of the board. However, when the via holes are moved towards the connector edge the return loss drops to ~16dB; this return loss stays relatively constant for positions ranging from 1mm to 27.2mm. Figure 4.16 illustrates that the main beam angle remains fixed at an angle of ~ 42˚, with some minor variations around the bottom lobes. The results indicate a high sensitivity in return loss to via position, and substantially less sensitivity in the radiation pattern. Based on this analysis the 0-mm via position was selected.
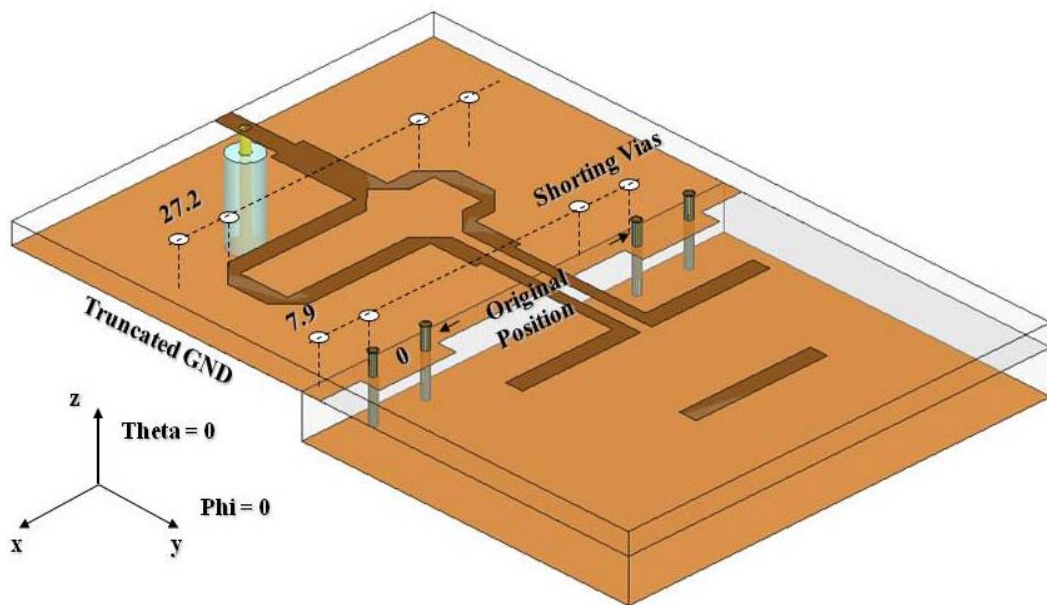
Figure 4.14 - Variations on via position from the center of the board towards the connector edge.
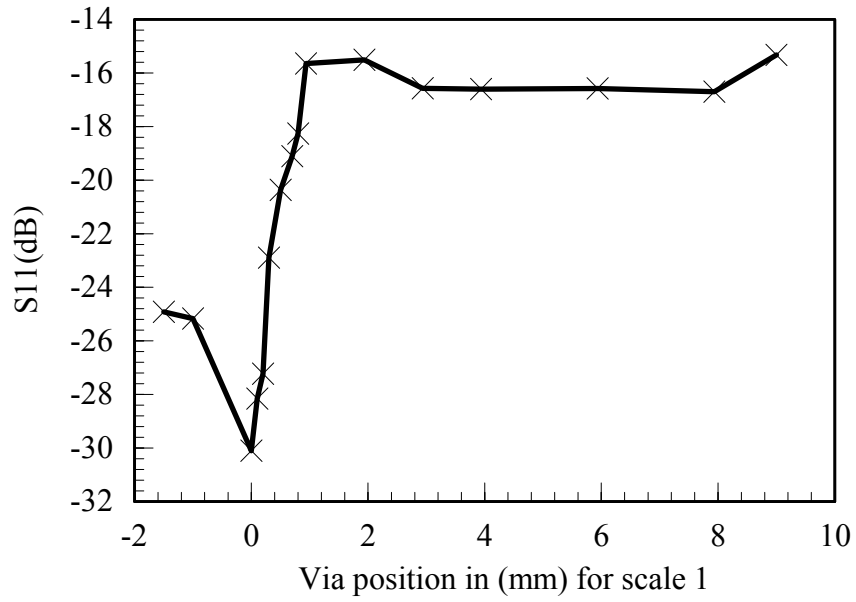
Figure 4.15 - Simulated return loss vs. via hole position at 2.45 GHz.
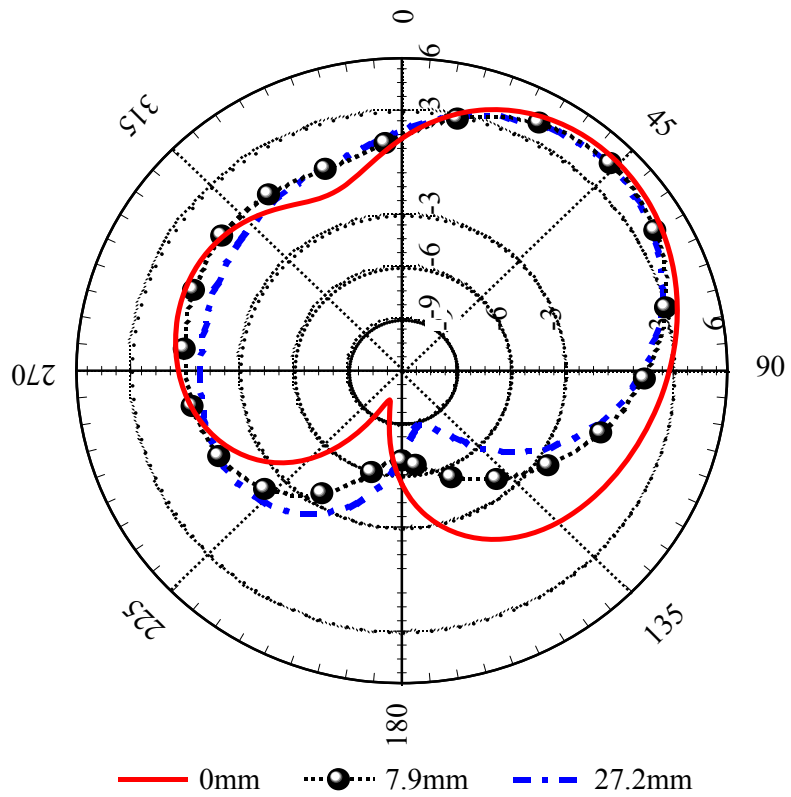
Figure 4.16 - Effect of via hole position on H plane gain pattern.

4.3.3 Impact of Director Dipole on Return Loss and Radiation Pattern

Simulations on return loss and radiation pattern (H-plane) with no director are compared between the proposed quasi Yagi (Figure 4.9) and the conventional quasi Yagi designed in [14]. The results on return loss from Figure 4.17 show that for the quasi Yagi in this research, not having a director causes the bandwidth to reduce by 94%, from 210 MHz (2.56-2.35 GHz) to 15 MHz (2.375-2.36 GHz). For the conventional non-grounded design in [14], Figure 4.18 demonstrates that excluding the director does not add a considerable drop on the bandwidth.
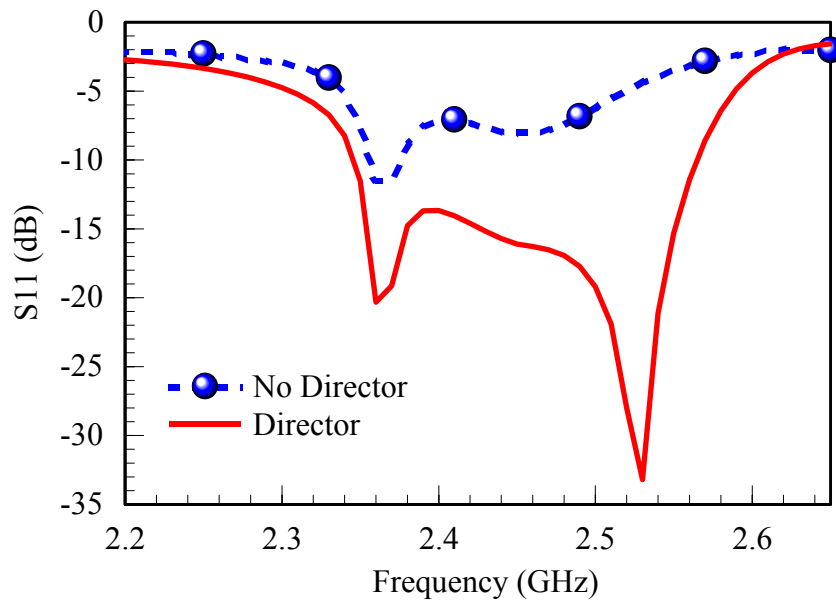
Figure 4.17 - Return loss for quasi Yagi backed by metal with and without a director.
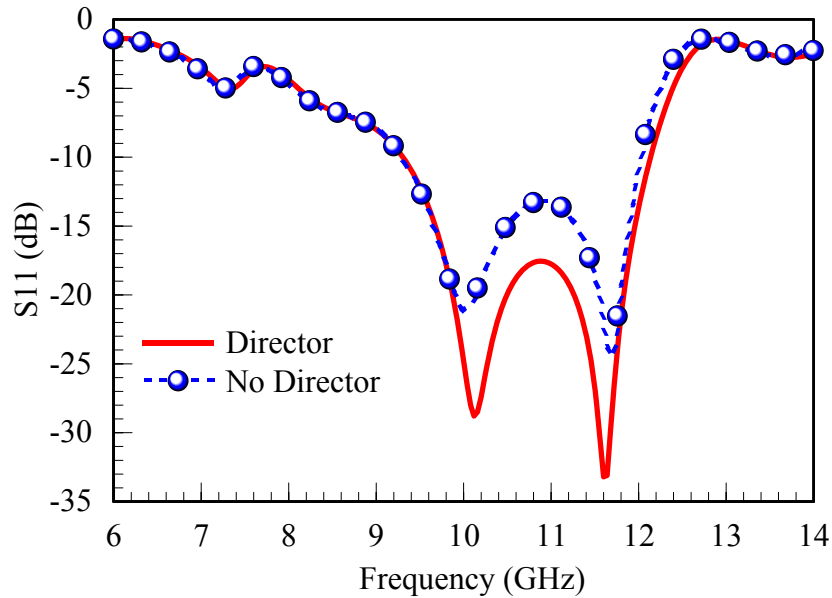
Figure 4.18 - Return loss for the quasi Yagi in [14] with and without a director.

Figure 4.19 compares the simulation results on the H-plane pattern for the quasi Yagi of this research with and without a director. The antenna with director displays maximum beam peak at 42˚ while the antenna without director peaks at 28˚, this means a 34% reduction on the off axis radiation. Thus the 3 dB beamwidth is also reduced (13%), the antenna with director offered 104˚ (5˚ to 99˚) of beamwidth and is reduced to 90˚ (-13˚ to 77˚). The presented simulation supports the importance of including a director for the main beam to steer towards the end fire direction. Finally, the same simulation is repeated on the conventional quasi Yagi design [14]; as observed in Figure 4.20 including a director does not affect radiation on the H-plane.

In summary, from the provided study it has been learned that the director is a critical element in the design of a quasi Yagi over a metal ground. The director contributes with better input match, wider bandwidth (210 MHz) and more beam steering (42˚) towards the end fire direction.
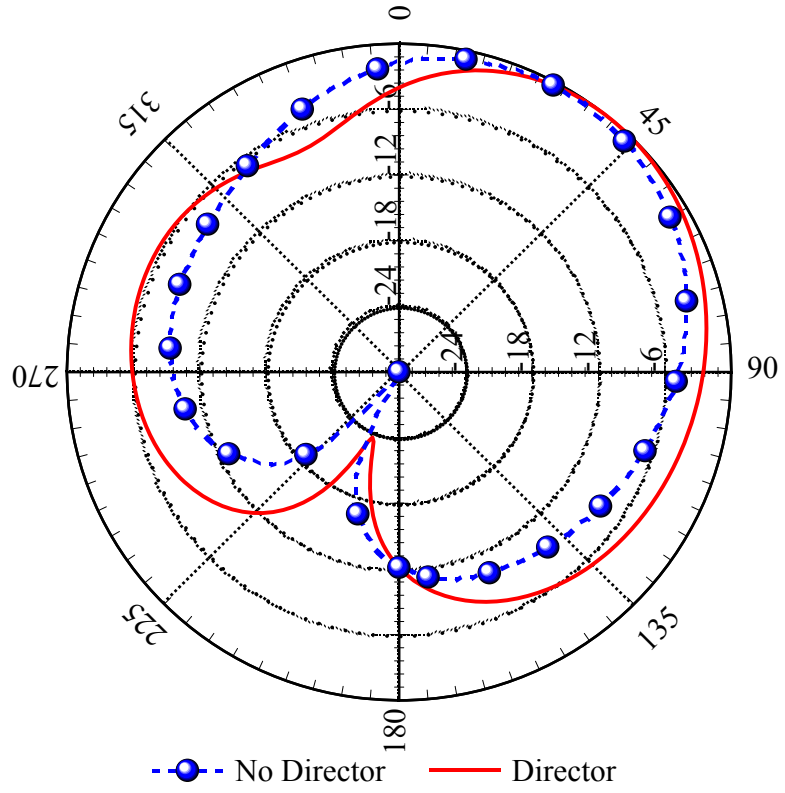
Figure 4.19 - Comparison of H-plane pattern for quasi Yagi with and without a director.
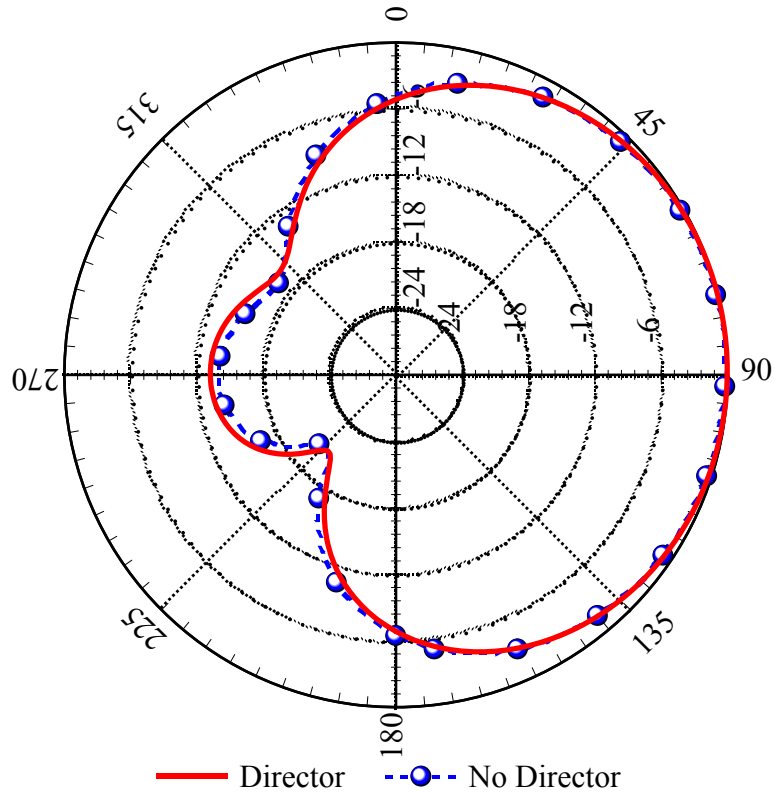
Figure 4.20 - Comparison of H-plane pattern on quasi Yagi from [14] with and without director.

4.4 Simulation and Measurement Results

A comparison between measured and simulated data on return loss, radiation pattern and gain is presented in this section. The results for return loss in Figure 4.21, show close comparison with a difference of 10% between the simulated bandwidth of 210 MHz (8.5%) and the measured bandwidth of 190 MHz (7.7%). For the normalized H-plane pattern, off-axis radiation is achieved with a variation of 2° between the simulated and measured data (42° and 40°), as illustrated in Figure 4.22 and Figure 4.23. The normalized E-plane co-polarization (C-POL) and cross-polarization (X-POL) patterns are displayed in Figure 4.24 and Figure 4.25. The simulated and measured C-POL exhibit directional patterns with front-to-back ratios of 3 dB and 5dB, respectively, while the X-POL levels are -6 dB and -7 dB. In comparison to non-grounded quasi Yagi

antennas [14] the front-to-back ratio is 12 dB smaller while the X-POL is 10dB larger. The diminished front-to-back ratio and X-POL are a result of the metal surface underneath the dipole elements which eliminates the TE_0 modes and propagates strongly the TM_0 modes. The simulated gain is 5.4 dB (Figure 4.27) and the measured gain is 4.5dB; the acquired gain is very close to what is expected from non-grounded quasi Yagis [14]. The simulated directivity and efficiency are 5.8 dB and 91%, respectively, while the corresponding measured values are 5 dB and 89%.
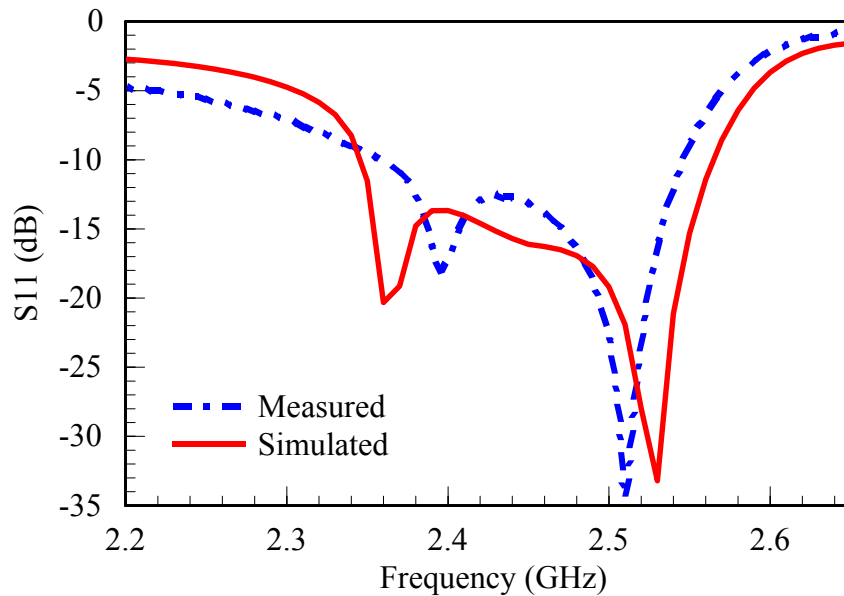
Figure 4.21 - Simulated vs. measured return loss for the quasi Yagi antenna. The simulated bandwidth ranges from 2.35 to 2.56 GHz while the measured bandwidth extends from 2.36 to 2.55 GHz.
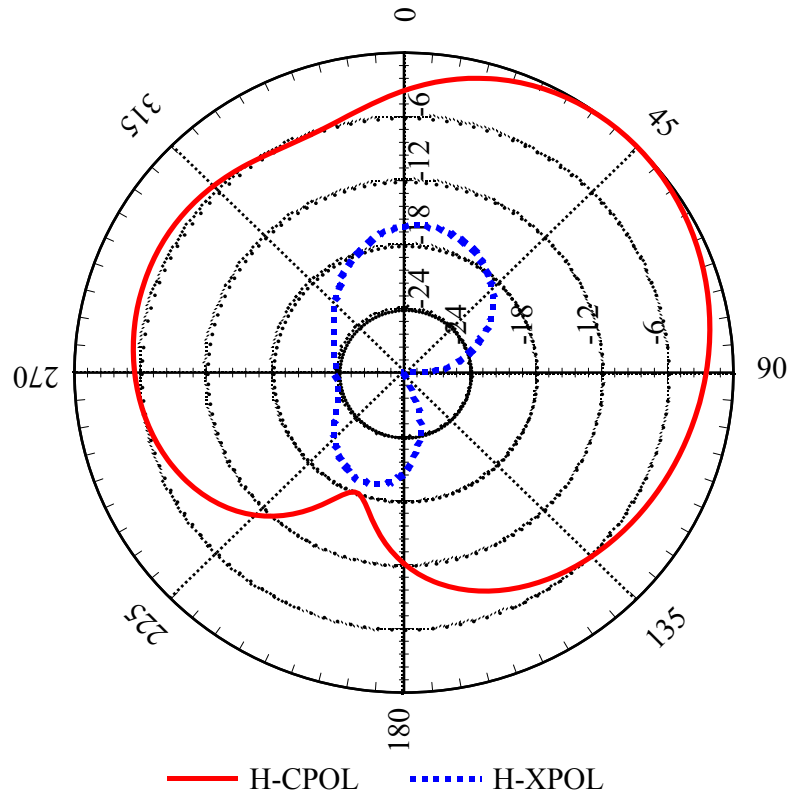
Figure 4.22 - Simulated 2.45 GHz normalized H-plane patterns for the quasi Yagi antenna. The beam peak angle shows a maximum tilt of 42˚. The pattern is normalized to the H-CPOL value.
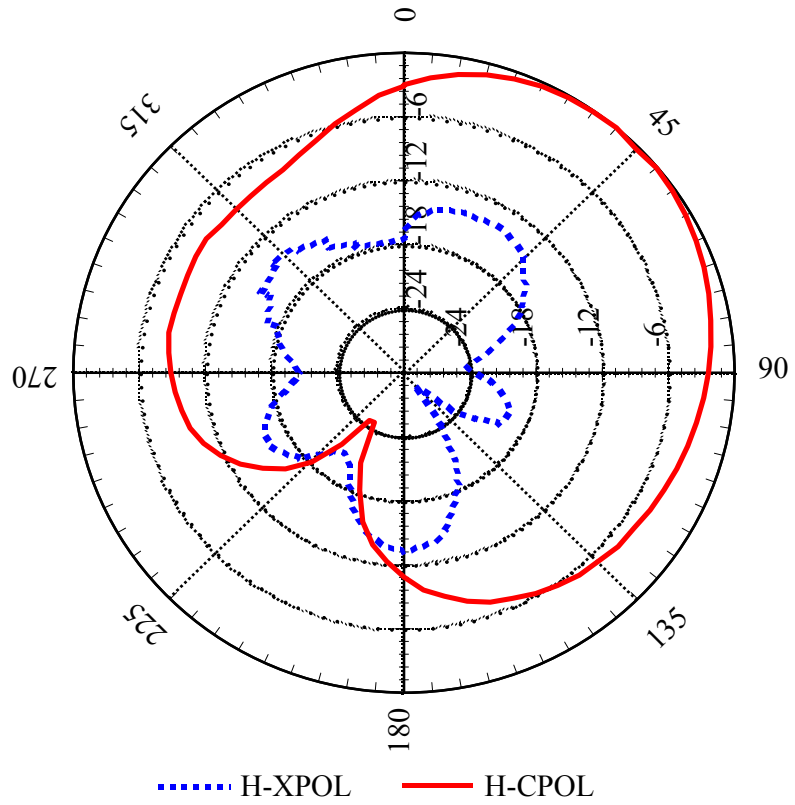
Figure 4.23 - Measured 2.45 GHz normalized H-plane patterns for the quasi Yagi antenna. The beam peak angle shows a maximum tilt of 40°. The pattern is normalized to the H-CPOL peak value.
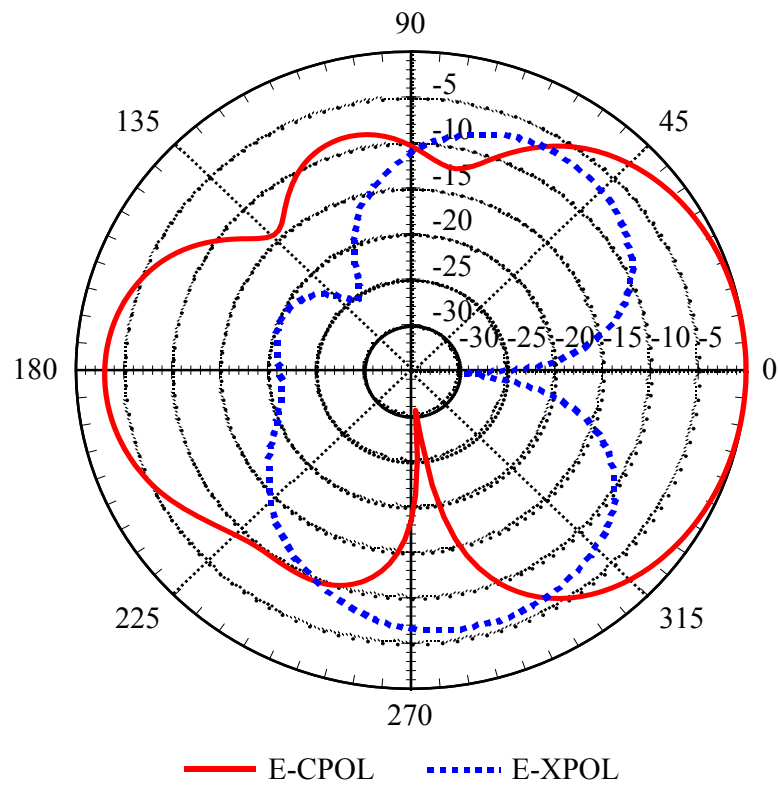
Figure 4.24 - Simulated 2.45 GHz normalized E –plane patterns for the quasi Yagi antenna. The pattern is normalized to the E-CPOL peak value.
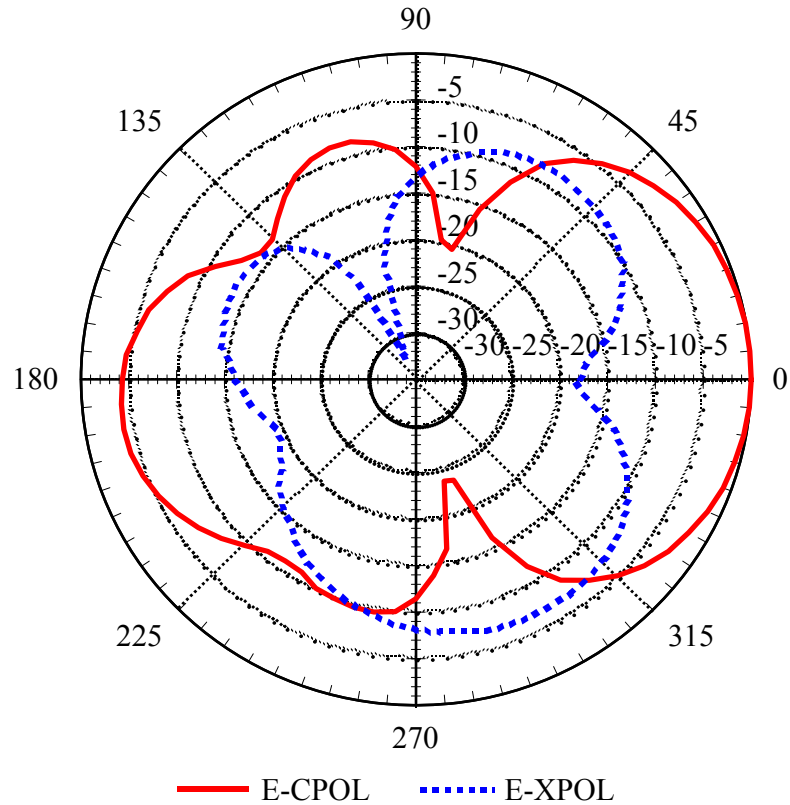
Figure 4.25 - Measured 2.45 GHz normalized E-plane patterns for the quasi Yagi antenna. The pattern is normalized to the E-CPOL peak value.

Figure 4.26 compares simulations on the normalized H plane pattern (beam tilt) for the quasi Yagi with a back metal ground and simulations for the normalized H pattern for a microstrip patch antenna. The microstrip patch antenna was design to operate at the same frequency and design under the same material as the quasi Yagi. The simulated maximum beam peak for the quasi Yagi at $\theta = 42°$ was 1 dB greater than the maximum beam peak for the microstrip patch at $\theta = 0.°$ In the broadside direction ($\theta = 0°$) the microstrip patch beam peak is 2.4 dB bigger than that of the quasi Yagi, and in the end fire direction ($\theta = 90°$) the beam peak of the quasi Yagi is 9 dB bigger than that of the microstrip patch. This comparison confirms that in relation to a well known broadside

radiation the proposed quasi Yagi steers most of its beam towards the end direction while

backed by a metal.
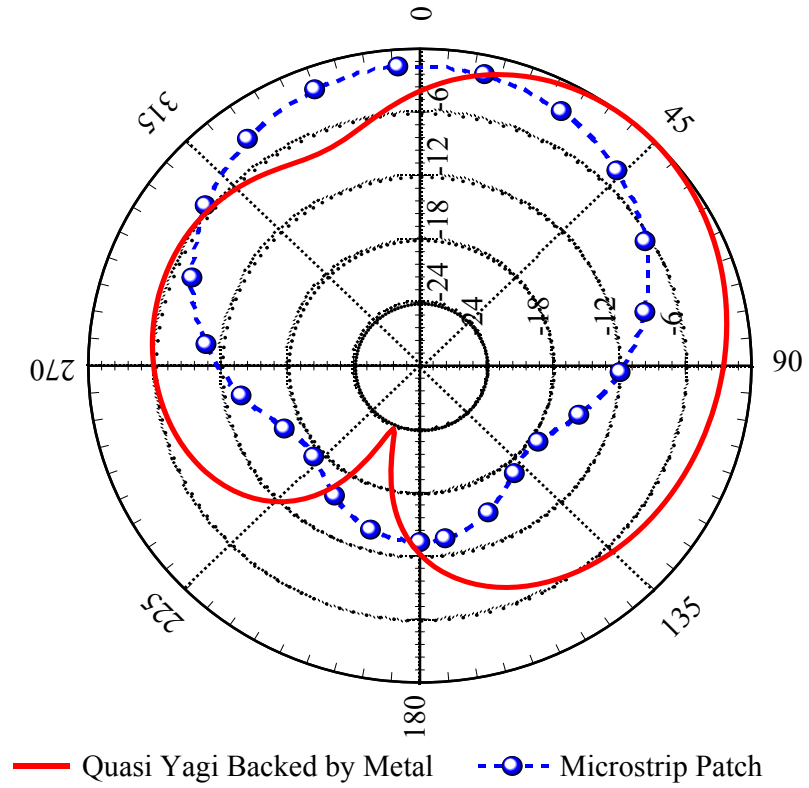
Figure 4.26 - H-plane pattern comparison of the quasi Yagi backed by a ground vs. a micrsotrip patch antenna.
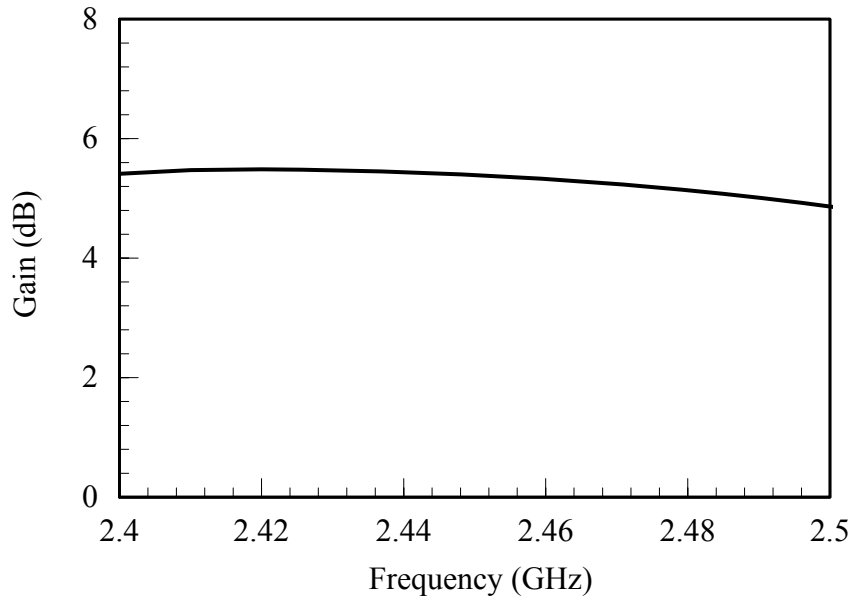
Figure 4.27 - Simulated gain vs. frequency sweep for the quasi Yagi antenna.

4.5 Summary and Conclusion

A new implementation of a quasi Yagi antenna with end fire like radiation when backed by a metal ground has been proposed. To realize the necessary pattern a high profile substrate is added under the dipole elements. The addition of this substrate cancels out the shorting effect of the ground metal and allows the main beam to be steered from the broadside direction while maintaining good radiation efficiency. In addition for this work the use of a director dipole is critical to maintain input match and beam steering away from the broadside direction. This is not the case for the conventional quasi Yagi design [14].

The work presents an analysis of the relation of substrate height and shorting via position to return loss and radiation pattern at 2.45GHz. A substrate 7.5 mm thick is chosen because it offers a beam tilt of 42° and a power gain of ≈5 dB. From the test on substrate height versus via position it is learned that the center of the board is the best location for these vias, providing in a return loss of 30dB.

74

Finally, a comparison is presented on the H-plane pattern of the quasi Yagi over a metal versus a broadsided microstrip patch antenna. The results support that good beam steering has been achieved by the quasi Yagi by offering more than 10dB of gain in comparison to the patch towards the end fire direction.

Chapter 5

A Multilayer Jerusalem Cross Frequency Selective Surface with Adequate Angular

Stability at 2.4 GHz ISM band

5.1 Introduction

This chapter presents the design of an electromagnetic textured structure which will be used as a ground plane for the quasi Yagi antenna. This structure is commonly referred to as a high impedance surface (HIS) or electromagnetic band gap structure (EBG). A HIS structure is a periodic cell structure which alters the electromagnetic characteristics of a ground plane. The HIS forbids the propagation of surface waves (AC currents) within a frequency band (band-gap) and reflects electromagnetic waves with, ideally, no phase reversal, ($|\Gamma| / \angle \Gamma$, $1/0˚$). Over the range of the band gap, both TE and TM surface waves are suppressed. At frequencies below the lower band edge, the surface impedance is inductive and TM surface waves can propagate. At frequencies higher than the upper band edge, the surface impedance is capacitive and TE surface wave can propagate. The HIS enhances antenna performance by improving gain, reducing backward radiation, increasing efficiency, and eliminating coupling between antenna elements in an array configuration.

Previous work in this type of structure includes that from Sievenpiper et al in [22] which uses an array of hexagonal patches as the HIS. Recent studies in [23] and [24] have found that the frequency band-gap for the hexagonal patch is sensitive to oblique angles of incidence for TE waves and TM polarized waves. The unstable behavior is a

consequence of the surface impedance of the HIS not being uniform with respect to different spatial harmonics for the large angular spectrum of TE and TM polarized waves radiated by an antenna. Consequently, the result is a summation of constructive and destructive interference between the antenna and the HIS.

The main focus of the work presented herein is the design of a HIS surface that is frequency stable for a wide range of incident angles for TE and TM polarized waves. Earlier configurations for HISs such as the conventional square patch, the grid spiral (with loops and without loops) [24], and the Jerusalem Cross frequency selective surface (JC-FSS) [25] have been investigated for angular stability. The square patch offers angular stability only for TM polarized waves as a result of the excitation of the shorting vias. For the TE polarized waves the resonant frequency shifts towards higher frequencies as the angle of incidence increases. The designs of the grid spiral with loops and without loops are stable for both TE and TM polarized waves but for a lower angular spectrum (<45˚). In addition the spiral design presents complexity of design and fabrication. The JC-FSS suggests an optimal design for this work because it provides small size, ease of fabrication (no vias), and frequency stability for angles of incidence of up to 70˚ for both TE and TM polarization.

The JC-FSS configuration is based on [25] and optimized for operation in the 2.4 GHz ISM band. The new contribution offered by this work is the addition of a second layer of dielectric slab flush mounted on top of the FSS. The added layer represents a superstrate separating the FSS from the antenna. Consideration of the superstrate for the FSS model, results in frequency tuning for the band gap from to 3.2 GHz to 2.45 GHz for the same FSS dimension.

The derivation of the elements for the multilayer JC-FSS is achieved analytically through closed-form equations from [26] and [27]. From here, the resulting model is simulated and optimized using Ansoft Designer (AD). The simulated results demonstrated an EBG with an angular stability (at the center frequency) of 70° for TE polarization and >80° for TM polarization, a bandwidth of 4.5%, and magnitude for the reflection coefficient greater than 0.8. The measured FSS exhibits 4%-7.7% bandwidth (at 2.55GHz and 2.67 GHz) for TE/TM polarized waves with incident angles ≤ 60° measured in the far field.

This chapter begins by presenting a comparison from a literature review on the properties of surface waves on a metal surface versus on a HIS. Following this, the JC-FSS is modeled using quasi-TEM closed form equations. Following, a discussion is presented on the effect of the superstrate over the FSS. Finally, the equation-based design is optimized through simulations and later measured, with a good comparison between simulation and measurement data. The simulated results from this research (USF) match up to previous work by [25] to show adequate operation for the FSS.

5.2 Surface Waves

A theoretical study is prepared which compares the properties of surface waves on a metal surface versus a textured surface. The surface waves on a metal conductor are AC currents bound to the interface until a discontinuity is reached (e.g. edge of board). The discontinuity generates scattering of the wave which propagates into surrounding media and produces interference. The purpose for the textured surface is to suppress this surface current over a range of frequencies called the band gap.

78

5.2.1 Metal Surfaces

Surface waves are propagating electromagnetic waves bound to the boundary between metal and air. At microwave frequencies surface waves are AC currents which occur on any electric conductor. For a smooth and flat conductor the surface wave does not couple to external plane waves, nevertheless it will radiate if scattered by bends, discontinuities, or surface texture.

An example of a TM surface wave propagating across a metal slab is shown in Figure 5.1. The magnetic field is transverse to the direction of propagation and is associated with the longitudinal currents flowing on the conductor. The electric field is associated with the charge on top of the conductor and it bounces out of the surface in loops. The charge oscillates and the wave propagates along at the surface at the speed of light. At microwave frequencies the electromagnetic fields extend many thousands of wavelengths into the surrounding space, thus surface waves across the metal are often described as surface currents.
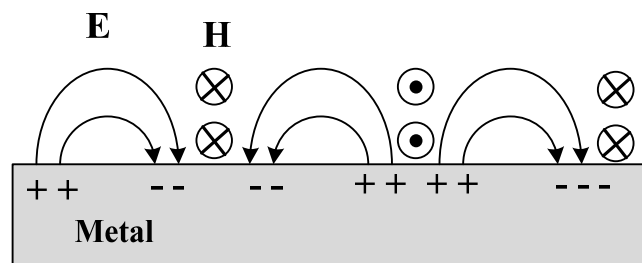
Figure 5.1 - A TM surface wave propagating across a metal slab.

Surface waves are inherent in many antennas situations where a metal backing is included, such as the quasi Yagi design of this research. If the radiating element is placed near the ground plane, it will generate currents that propagate along the sheet. On an infinite ground plane, the surface currents would only be noticed as a small reduction in

79

radiation efficiency (e.g. increase in side-lobes and gain reduction [8]). In reality, the ground plane has a finite size and the currents propagate until they reach an edge or a corner. Any break on the flat surface allows for the current to radiate. The result is a destructive interference which cancels the currents of the antenna and decreases the radiation efficiency. Furthermore, if multiple antennas share the same ground plane, surface currents can cause unwanted mutual coupling.

5.2.2 Textured Surface

By adding a special texture to a metal surface, it is possible to alter its electromagnetic characteristics [15]. If the period (D) of the textured surface is much smaller than the wavelength (D << λd, where λd is the wavelength in the dielectric media), the structure can be derived by an effective medium model, and its qualities can be summarized into a single value, the surface impedance. This boundary condition defines the ratio of the tangential E field to the tangential H field at the surface, which can also be represented by Ohms law, which is the ratio of the voltage to the current along the sheet in Ohms/square. A smooth or flat conductive sheet has low surface impedance, while a textured surface has high surface impedance.

A high impedance surface consists of an array of metal grid protrusions arranged on a two dimensional lattice over a flat metal sheet. If the protrusions are small compared to the wavelength, the electromagnetic properties can be described by lumped circuit elements, i.e. capacitors and inductors. The proximity of neighboring metal elements provides capacitance and the substrate height provides inductance. In other words, the metal protrusions and the substrate slab act as parallel resonant LC circuit blocking the flow of currents along the sheet.

Due to its unusual high impedance, the TE/TM surface wave modes on a high impedance surface are different from those on a smooth metal sheet. A HIS can support tightly bound TM modes that propagate much more slowly than the speed of light. It can also support TE modes that are bound to the surface at some frequencies, but radiate readily at other frequencies. For TE surface waves, the E field is tangential to the surface while the H field jumps out of the sheet in loops. This behavior resembles that of Figure 5.1 but with electric and magnetic fields exchanged as shown in Figure 5.2.
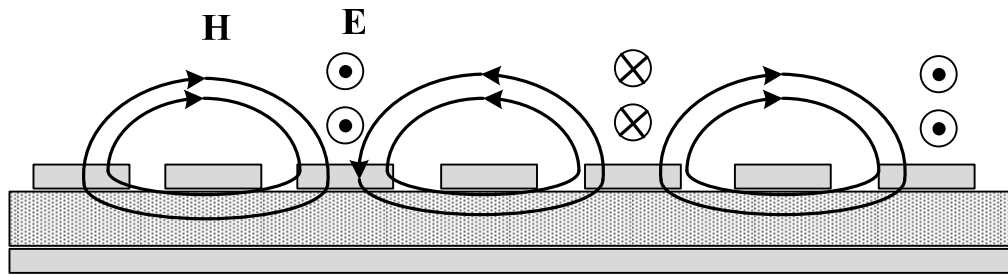
Figure 5.2 – A TE surface propagating across a high impedance surface.

In the frequency range where the surface impedance is very high, the tangential magnetic field is small, causing the structure to behave as a magnetic conductor.

5.3 Jerusalem Cross Frequency Selective Surface

The HIS selected for this work is the Jerusalem Cross Frequency Selective Surface (JC-FSS). This design offer improvement to existing technology from [24] by maintaining frequency stability for a large angular spectrum of TE and TM polarized waves.

Early work on FSSs by Munk [28] described the functionality of the Jerusalem Cross, specifically the current and voltage distribution for different harmonics. Each cell consists of a pair of center-connected cross dipoles terminated with end loading plates,

and in our design the metal pattern is sandwiched between two dielectric layers, as shown in Figure 5.3. A ground plane is present at the bottom surface.
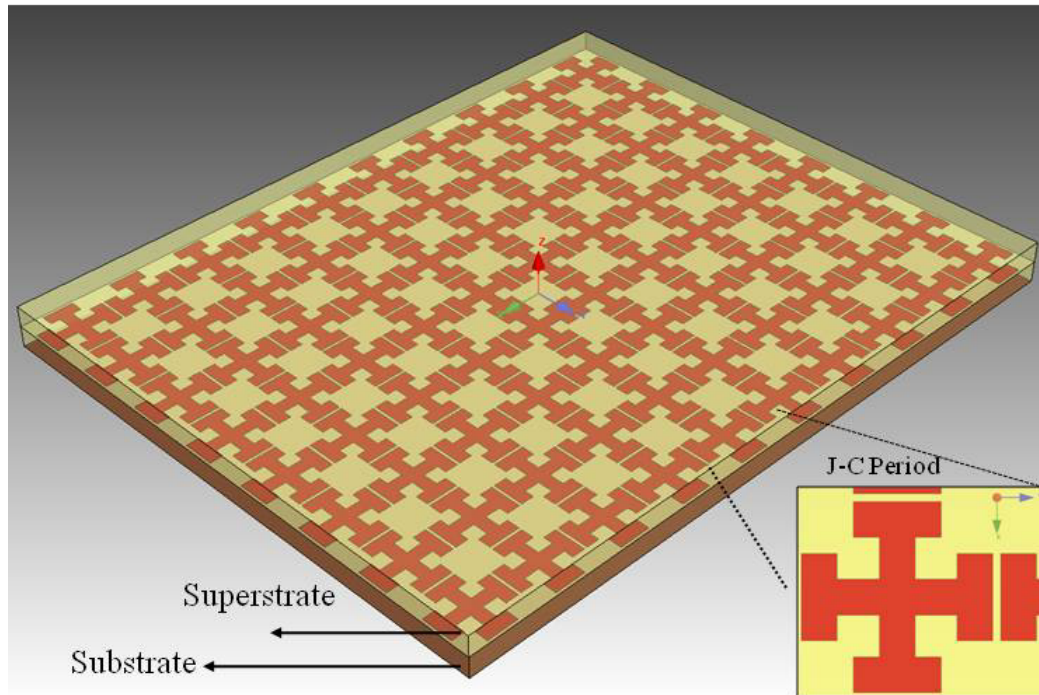
Figure 5.3 - JC-FSS multilayer design.

Similar work presented in [29] and [30] explained the JC-FSS as self resonant grid structures. The grid is made of the crosses and a square inductive grid enclosing the crosses. The self resonant grid is modeled by a series LC circuit, representing the cross, and a parallel LC circuit representing the square inductive grid. The stated designs along with the work in [25] provide supporting guidelines for realizing a JC-FSS.

5.3.1 Derivation of the JCFSS model

The JC-FSS can be effectively modeled by a parallel resonant LC circuit. The LC model consists of the parallel combination of the self resonant grid impedance (Zg) which represents a strip, with the grounded dielectric slab impedance (Zd). This model is applicable for a grid period (D) smaller than the wavelength (D << λg).

Figure 5.4 shows that Zg can be expanded into the series combination of the narrow strip impedance and the edge impedance between end loading strips. The narrow strip impedance is mostly inductive (Lg) and is derived from Telegrapher equations or from the stepped impedance equations from [13]. Its derivation is detailed in Appendix B. For convenience the equation for the grid inductance is re written as

$$L_g = \frac{Z_0 \beta \ell}{\omega} \tag{5.1}$$

The impedance between end loading plates is mostly capacitive (Cg) and is a result of the charge built up between these plates [15]. The equation for this static approach is

$$C_g = \frac{2d}{\pi} \varepsilon_0 \varepsilon_{\text{eff}} \cosh^{-1}\left(\frac{a}{g}\right) \tag{5.2}$$

where ε_{eff} is the effective permittivity including the superstrate layer, d is the length of an end loading plate, g is the gap between crosses and a is the period between adjacent capacitive plates.
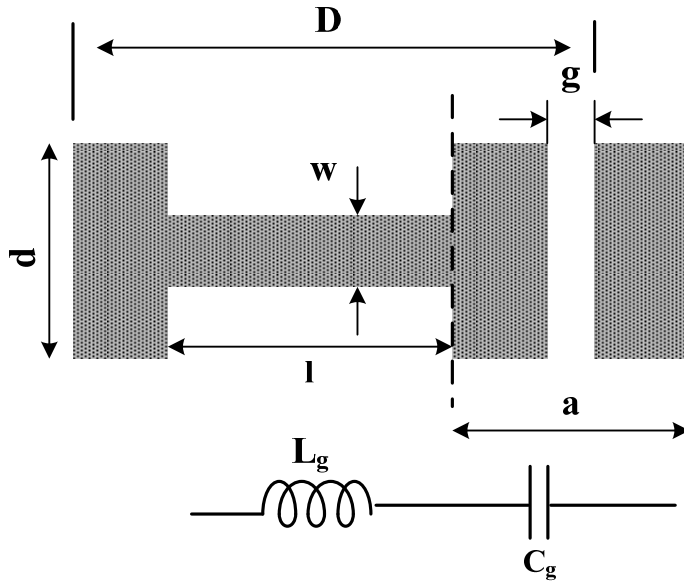
Figure 5.4 - Equivalent circuit for the self resonant grid.

As illustrated in Figure 5.5 the Zd is mostly inductive (Ld) and is derived from the TEM transmission line equation for a dielectric slab back by a perfect electric conductor (PEC). In (5.3) the wave number k is $\omega\sqrt{\mu_0\varepsilon_0}\sqrt{\varepsilon_r}$.

$$L_d = \frac{\eta_0}{\sqrt{\varepsilon_r}}\frac{\tan(kh)}{\omega} \tag{5.3}$$
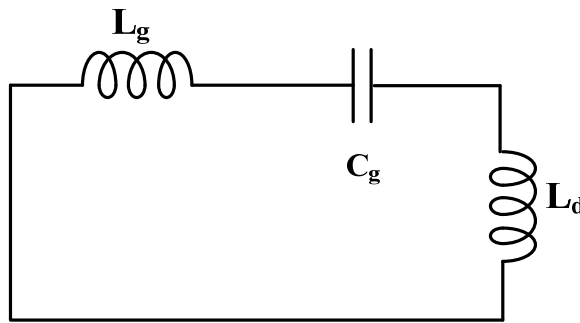
Figure 5.5 - Series combination of the self resonant grid with the dielectric slab impedance.

From the parallel LC circuit in Figure 5.5 the equivalent surface impedance is calculated by

84

$$Zs = \frac{Zg \cdot Zd}{Zg + Zd} \qquad (5.4)$$

$$Z_s = j\omega Ld \frac{1 - \omega^2 Lg \cdot Cg}{1 - \omega^2 \cdot (Lg + Ld) \cdot Cg} \qquad (5.5)$$

The resonant frequency can then be derived by equating the denominator from (5.5) to zero which results in

$$fr = \frac{1}{2\pi\sqrt{(Lg + Ld) \cdot Cg}} \qquad (5.6)$$

The bandwidth is obtained by dividing the equivalent impedance of the JC-FSS by the intrinsic impedance of free space. This equation, derived in detail in [15], gives the bandwidth over which the phase of the reflection coefficient falls between $\pm 0.5\pi$. If the criteria from [25] and [26] are followed then the phase of the reflection coefficient should fall between $\pm 0.25\pi$.

$$BW = \frac{\sqrt{\dfrac{Ld + Lg}{Cg}}}{\eta} \qquad (5.7)$$

The initial dimensions for the JC-FSS are obtained by linearly scaling in frequency the dimension from [26]. Next the JC-FSS is brought into Ansoft Designer and optimized for zero phase reversal for the reflection coefficient (Γ) at 2.45 GHz. Figure 5.6 shows the resulting dimensions for the optimized FSS. Both dielectric layers have a relative permittivity of 10.2. As demonstrated by [25], a high dielectric constant is preferred for low resonant frequencies to achieve better angular stability and smaller dimensions. The height (H) for each substrate is 2.5mm. Having a thick substrate adds inductance (Ld) to the equivalent surface impedance (5.5). The gap (g) between each

cross is 0.32mm (Figure 5.6). Having a small gap between crosses contributes more edge capacitance (Cg) which also increases the equivalent surface impedance.

The following conditions derived in [27] are followed as guidelines to achieve frequency stability with respect to incidence angle.

- The period of the cell (8.32mm) should be smaller than the wavelength (λg=39mm).

- No vias should be used as they affect the frequency stability for the angle of incidence of the TM polarized waves.

- The dielectric slab must be thin (kd*h<1); for this work kd*h = 0.065 < 1 from

$$kd = \omega\sqrt{\mu_0 \varepsilon_0 \varepsilon_r} \tag{5.7}$$
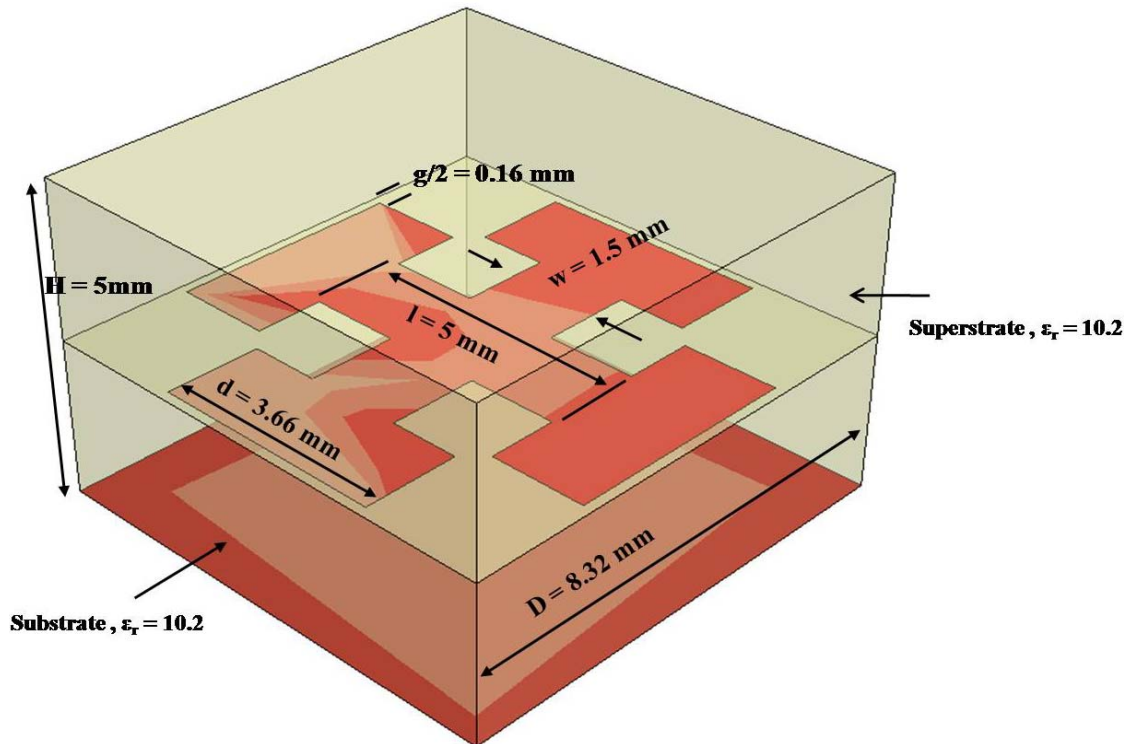
Figure 5.6 – Dimension of the cell of a JC-FSS.

5.3.2 Effect of the Superstrate over the FSS

The new feature introduced in this work is the addition of the dielectric layer (superstrate) on top of the JC-FSS. In comparison to other designs [25], the impinging wave is excited on top of the superstrate layer as shown in Figure 5.7. The equivalent reflection coefficient (Γ_{IN}) for the structure at oblique incidence for TE and TM polarized waves is the result of the combination of the reflected waves from the two substrate layers and ground. Γ_{IN} can be derived in detail through equations from [19].

The reflection coefficients for TE and TM waves at the JC-FSS boundary (top of substrate) are calculated by combining (5.5) with

$$\Gamma_{s}^{TE} = \frac{Zs \cdot \cos(\theta^1) - \eta_1 \cdot \cos(\theta)}{Zs \cdot \cos(\theta^1) + \eta_1 \cdot \cos(\theta)} \tag{5.8}$$

$$\Gamma_{s}^{TM} = \frac{Zs \cdot \cos(\theta) - \eta_1 \cdot \cos(\theta^1)}{Zs \cdot \cos(\theta) + \eta_1 \cdot \cos(\theta^1)} \tag{5.9}$$

where the incident (θ^1) and refracted angles (θ) have minimum effect on the phase of the reflected wave ($\angle\Gamma_s$ deg.) for the frequency range in which the JC-FSS exhibits high impedance, resulting in angular stability. The value for the JC surface impedance (Zs) is deduced from (5.5) and η_1 represents the intrinsic impedance of the superstrate, $\eta_0/\sqrt{10.2}$.

Furthermore, the reflection coefficient at the free space and superstrate boundary for TE and TM waves is derived. First the input impedance is found for the wave reflected from the JC,

$$Z_{IN}^{TE} = \eta_1 \cdot \frac{1 + \Gamma_s^{TE} e^{-j \cdot 2 \cdot \beta^1 d1}}{1 - \Gamma_s^{TE} e^{-j \cdot 2 \cdot \beta^1 d1}} \tag{5.10}$$

$$Z_{IN}^{TM} = \eta_1 \cdot \frac{1 + \Gamma_s^{TM} e^{-j \cdot 2 \cdot \beta^1 d1}}{1 - \Gamma_s^{TM} e^{-j \cdot 2 \cdot \beta^1 d1}} \tag{5.11}$$

after this, the results are included into

$$\Gamma_{IN}^{TE} = \frac{Z_{IN}^{TE} \cdot \cos(\theta^{inc}) - \eta_0 \cdot \cos(\theta^1)}{Z_{IN}^{TE} \cdot \cos(\theta^{inc}) + \eta_0 \cdot \cos(\theta^1)} \tag{5.12}$$

$$\Gamma_{IN}^{TM} = \frac{Z_{IN}^{TM} \cdot \cos(\theta^1) - \eta_0 \cdot \cos(\theta^{inc})}{Z_{IN}^{TM} \cdot \cos(\theta^1) + \eta_0 \cdot \cos(\theta^{inc})} \tag{5.13}$$

The relation between the angle of incidence and refraction at the boundary of each layer is determined from Snell's law of refraction in (5.14). This equation demonstrates that the addition of the superstrate layer reduces the angle of incidence for the wave impinging on the JC-FSS. For example, a travelling wave with an angle of incidence of 60˚ at the superstrate surface generates an angle of refraction of 15˚. This angle of refraction will be the angle of incidence for the substrate.

$$\theta^1 = \sin^{-1}\left[\left(\frac{\beta^{inc}}{\beta^1}\right) \cdot \sin(\theta^{inc})\right] \tag{5.14}$$

Another effect added by the addition of a substrate layer is on the value of the effective permittivity. The effective permittivity varies from ($\varepsilon_{eff} \approx 7.2$) for no superstrate to ($\varepsilon_{eff} \approx 9.7$) when the superstrate layer is included. This permittivity value needs to be considered because it influences the derivation of the grid capacitance in (5.2). Figure 5.8 shows the value for ε_{eff} calculated through EM simulations in Agilent's ADS for a covered microstrip transmission line with the same dimensions as one of the narrow strips for a cross. Since the propagation constant is a complex number ($\gamma = \alpha + j \cdot \beta$) the imaginary part is Im (γ) = $\omega \cdot (\mu\varepsilon_{eff})^{1/2}$, from this

88

$$\varepsilon_{\text{eff}} = \left(\frac{c \cdot \beta}{\omega} \right)^2 \qquad (5.15)$$

A comparison is performed on the design of a JC-FSS including the superstrate versus a design without the superstrate. For simplicity the evaluation is carried out for a wave with normal incidence. At normal incidence Γ_{IN} is independent of the polarization of the incident wave since the E and H fields are both tangential to the boundary. Simulation results in Figure 5.9 demonstrate that the superstrate shifts the frequency down to the desired band from 3.2 to 2.45 GHz (750MHz). This analysis supports the importance of accounting for any additional layer covering the JC-FSS during the FSS closed form modeling to prevent undesired frequency shifts. In addition, an overall cell size reduction has been achieved by considering the extra layer; an equivalent cross cell size for 3 GHz, with no superstrate, is used at 2.4GHz with superstrate.
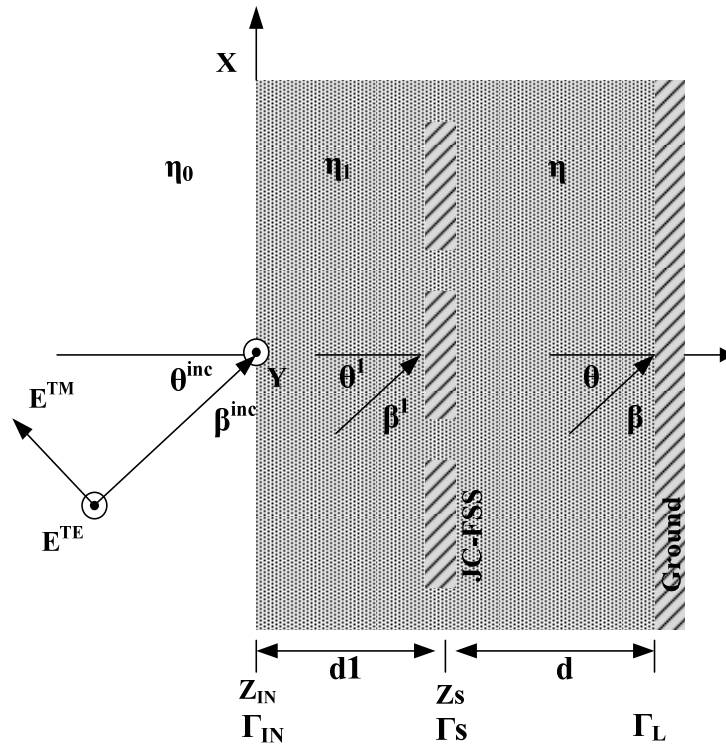

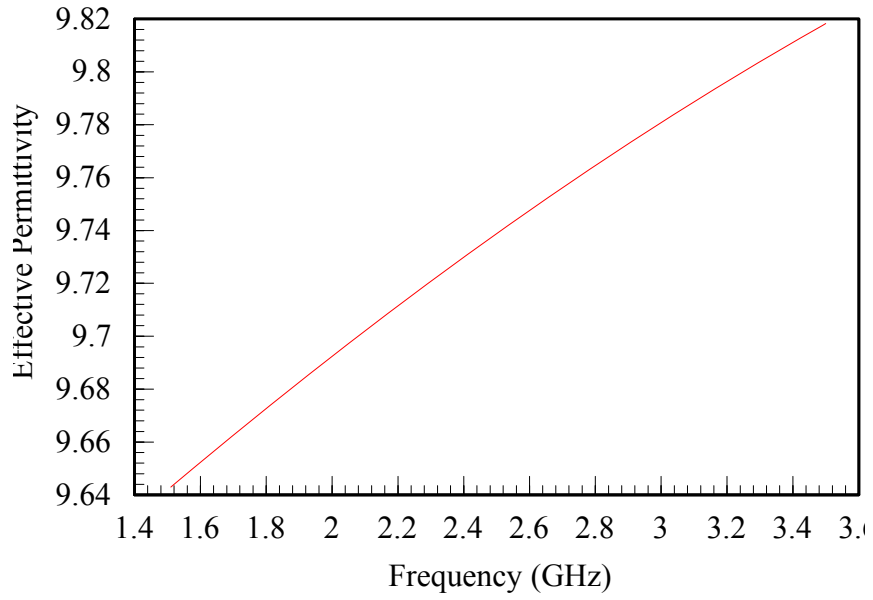Figure 5.7 - TE and TM polarized waves incident on the superstrate layer covering the FSS.

Figure 5.8 - ε_{eff} including the superstrate.
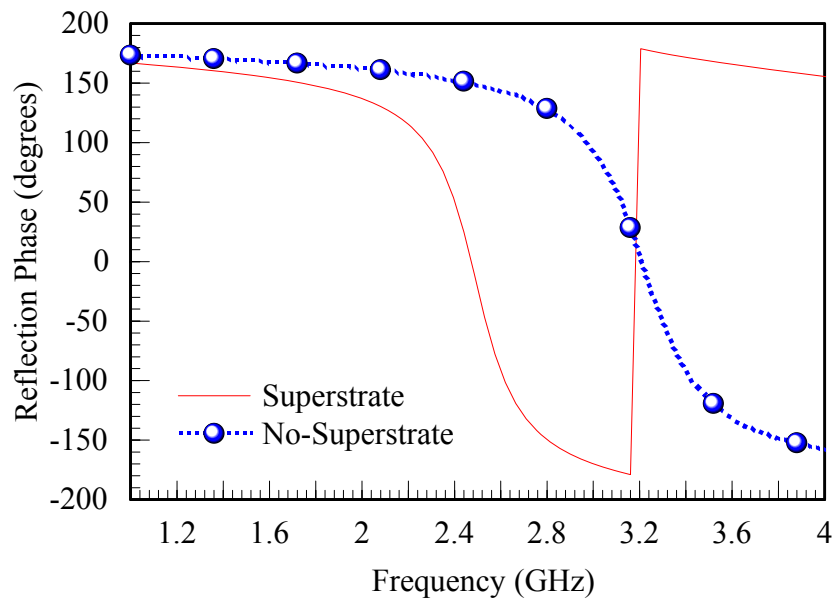
Figure 5.9 - Reflection phase (deg.) vs. frequency for a JC-FSS with and without superstrate.

5.4 Quasi-TEM Modeling, Simulation and Measurement on the JC-FSS

The approximation of the quasi-TEM closed form equations (5.1)-(5.6) for the JC-FSS is validated by comparing its results in reflection phase versus frequency for TE and TM polarized waves at 0°, 30° and 60° of incidence with simulations for the same cell size and angular incidence in Ansoft Designer (AD). Following the criteria from [25] and [26] the operational radiation bandwidth should fall between a reflection phase of ±45°. Figure 5.10 shows excellent agreement between the quasi-TEM equation model and AD simulation for the JC-FSS excited at normal incidence ($\theta^{inc} = 0°$). The equation based model shows a bandwidth extending from 2.44 to 2.55 GHz (110 MHz, 4.5%) with mid-band frequency at 2.5 GHz. The AD simulation result shows a bandwidth from 2.39 to 2.52 GHz (130MHz, 5.3%) with mid-band at 2.45 GHz. The difference in mid-band frequency between the equation based model and simulated design is of only 2 %, which confirms that an excellent equation based derivation has been implemented. For TE and TM polarized waves with larger angles of incidence, 30° and 60°, Figure 5.11 and Figure 5.12 show that there is excellent frequency stability. The mid-band frequency shifts by 2% for both TE and TM waves.

With respect with radiation bandwidth, the equation based model and the AD simulation present close comparison for the various angles of incidence, as shown in Table 5.1. The results show that the frequency band is most sensitive to the TE and TM waves as the incident angle is increased, particularly for the TE wave where the bandwidth is reduced by half when compared to normal incidence. However, the frequency shift stays in band (2.4-2.48GHz) confirming the stability of the design

Table 5.1 - Radiation bandwidth for reflection phase (deg.) for TE and TM polarized waves for the quasi-TEM closed form equations and for the AD simulations.

Incident wave	Quasi-TEM equations	AD simulations
Normal Inc. ($\theta^{inc} = 0°$)	2.44 – 2.45 GHz, 4.5%	2.39 – 2.5 GHz, 4.5%
TM - 30˚	2.45 – 2.57 GHz, 4.7%	2.4 – 2.52 GHz, 4.8 %
TM - 60˚	2.4 – 2.63 GHz, 9%	2.39 – 2.61 GHz, 8.8%
TE - 30˚	2.46 – 2.56 GHz, 4%	2.39 – 2.49 GHz, 4%
TE - 60˚	2.51 – 2.57 GHz, 2.4%	2.42 – 2.49 GHz, 2.8%
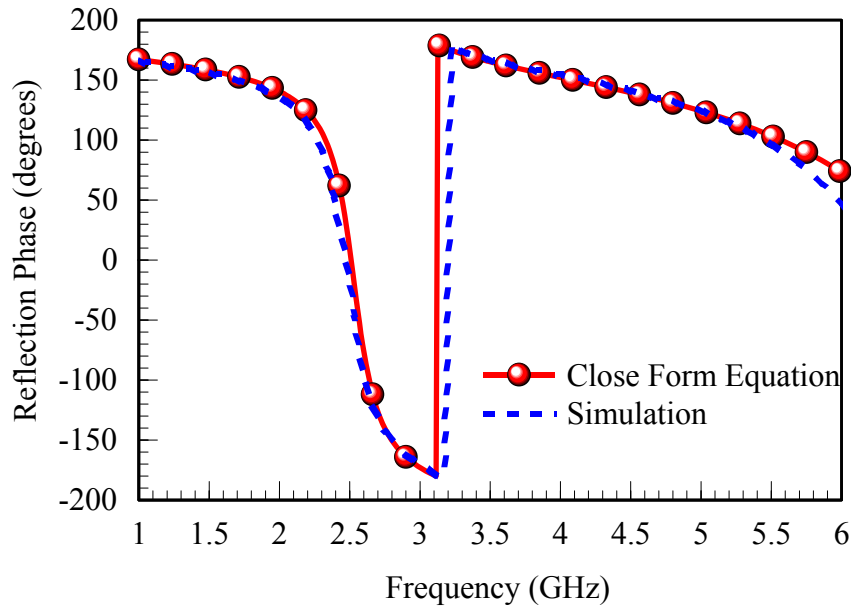
Figure 5.10 - Comparison of the reflection phase (deg.) vs. frequency response for a normal incident wave using the quasi-TEM closed form equations with mid-band at 2.5 GHz and Ansoft Designer simulations at 2.45 GHz.
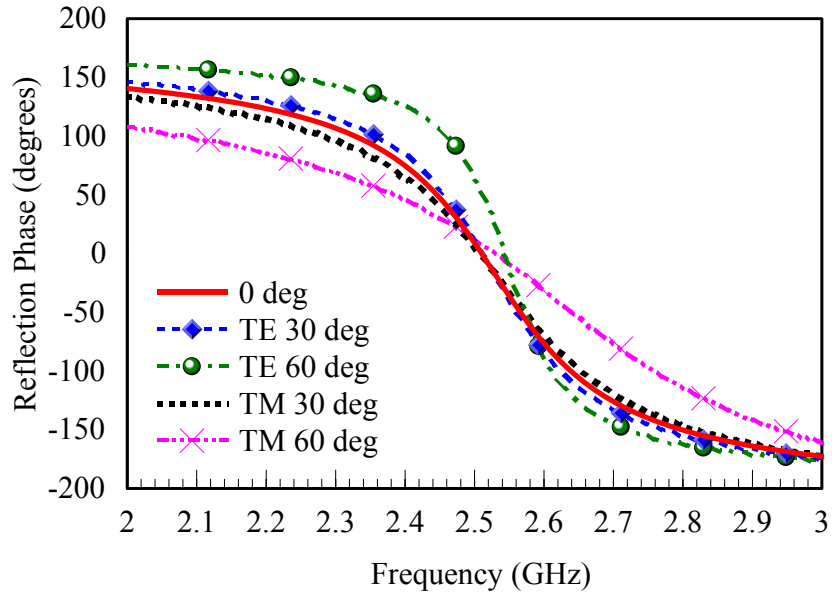
Figure 5.11 - Reflection Phase (deg.) vs. frequency for equation based model for TE and TM polarized waves with angles of incidence of 0˚, 30˚, 60˚.
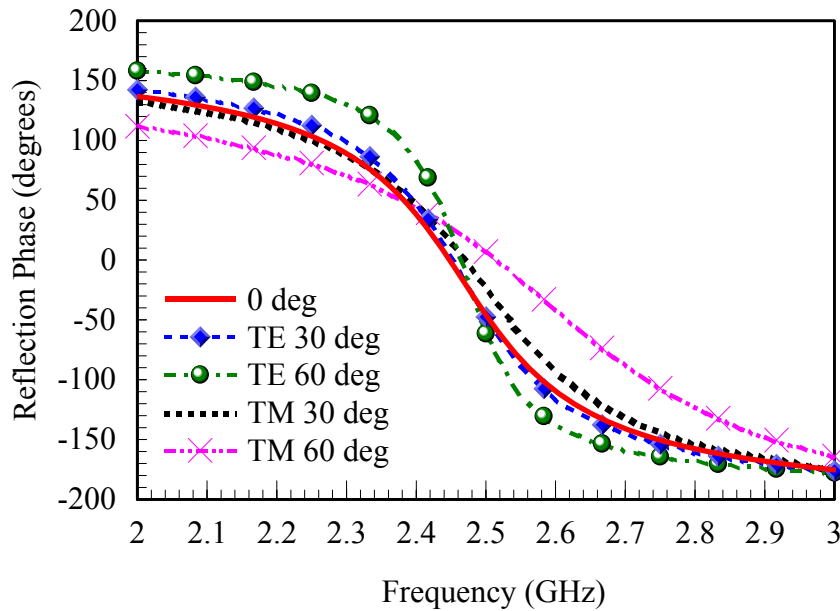
Figure 5.12 - Reflection Phase (deg.) vs. frequency on AD simulations for TE and TEM polarized waves with angles of incidence of 0˚, 30˚, 60˚.

Next, the simulated results from this research (USF) are compared to previous work by [25] to show adequate operation for the FSS. The graphs are plotted at 2.45 GHz

for the design proposed by this research (USF) and at 14 GHz for the FSS by Hosseini [25]. The following two conditions are taken as criteria to validate that angular stability for both TE and TM polarized waves has been achieved: at the resonant frequency (mid-band) the magnitude of the reflection coefficient (Γ) should be greater than 0.8, and the phase of Γ must be within $+45°$ and $-45°$.

The simulated results following these specifications are presented in Figure 5.13 and Figure 5.14. The simulations covered an angular spectrum from 0° to 80°. Figure 5.13 show that the USF design meets the requirements for the reflection coefficient magnitude and compares well to [25], differing only by ~3%. Figure 5.14 shows an angular stability for a TE polarized wave of up to 70°, which is only 5% less stability than given in [25].
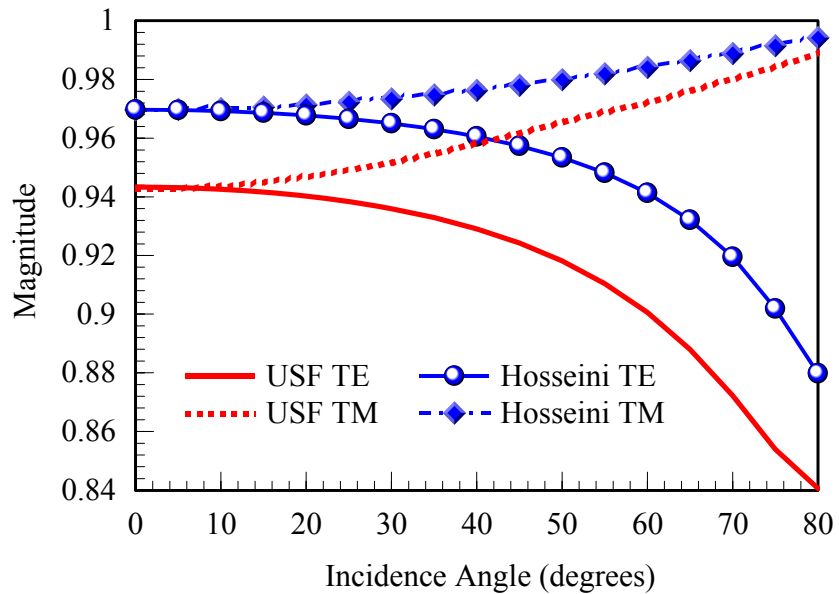
Figure 5.13 - Magnitude of Γ for the TE and TM polarized waves at 2.45 GHz for USF and at 14.1 GHz for Hosseini [25].
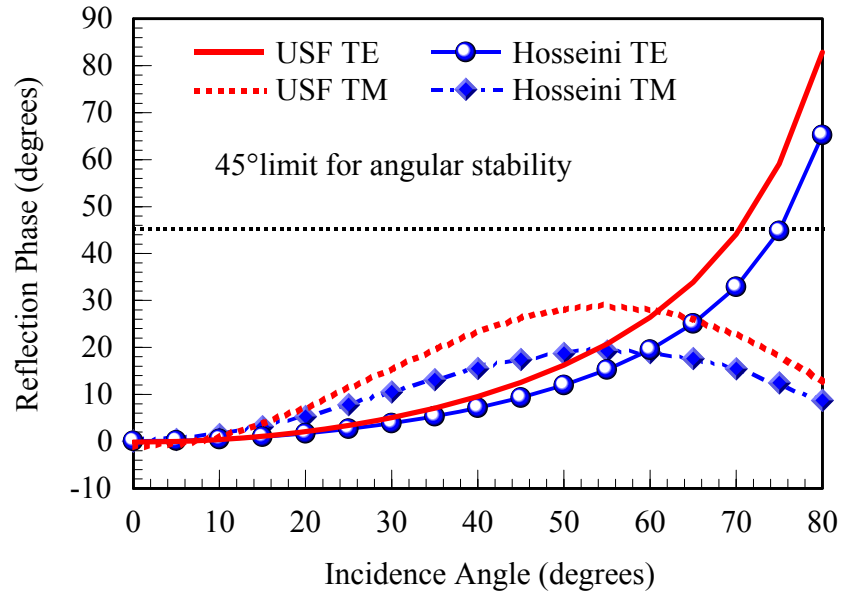
Figure 5.14 - Phase in degrees of Γ for the TE and TM polarized waves at 2.45 GHz for USF and at 14.1 GHz for Hosseini [25].

Experimental characterization was performed using two directional tube antennas as the transmit/receive elements and measuring the resulting reflection coefficient from the JC-FSS. An illustration of the fabricated structure before being covered is shown in Figure 5.15. The overall size of the FSS board is 12 x 18 inches. The large size for the test board is a consequence of the large beam-width (55˚/70˚ and 40˚/45˚ for E and H) for the transmit/receive tube antennas. The measurements were carried in the far field region for an angular spectrum extending of 0˚, 30˚, 60˚.

Two measurements are recorded, one for a flat metal sheet set up (Figure 5.16) and another one for the JC-FSS (Figure 5.17). Next, the measured reflection coefficient of the metal sheet is used as the reference for normalization of the measured reflection coefficient of the JC-FSS. The difference between the two measurements should be 180˚ at the resonant frequency.
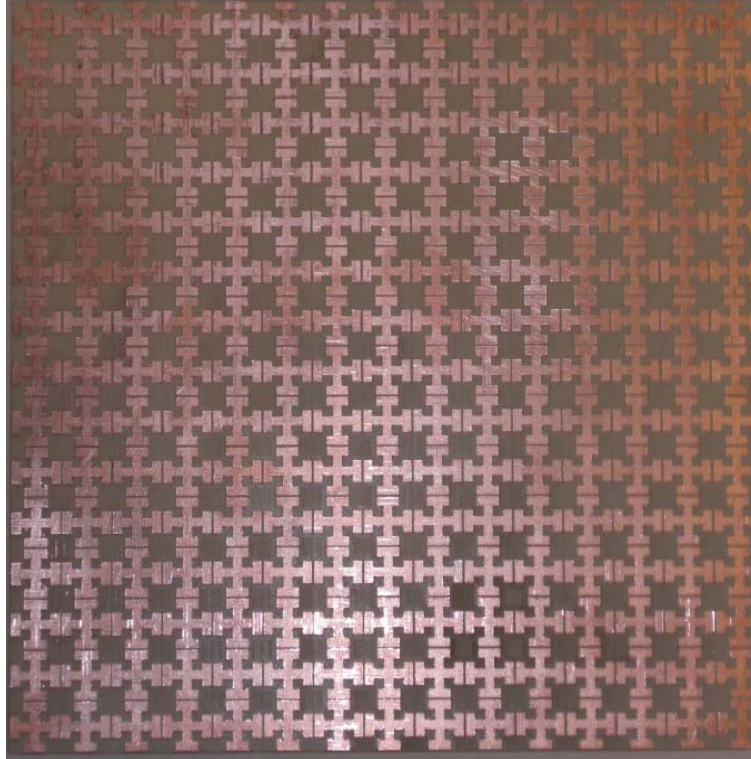
Figure 5.15 – Fabricated JC-FSS.
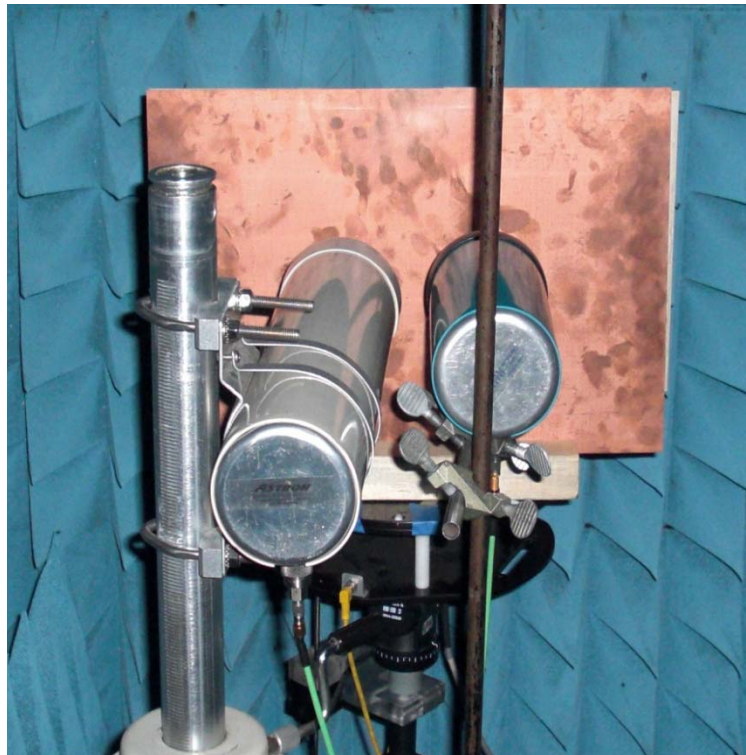
Figure 5.16 - Measurement on flat metal sheet.

Figure 5.17 – Measurement on covered JC-FSS.

The measurement results in Figure 5.18 show the resonant frequency for normal incidence (0˚) at 2.55 GHz with a frequency band of 4% (2.5-2.6GHz), and for oblique angles of incidence, 30˚ and 60˚, the resonant frequency is 2.65 GHz with a frequency band of 7.7% (2.51-2.71GHz) and 5% (2.59-2.73GHz) respectively.
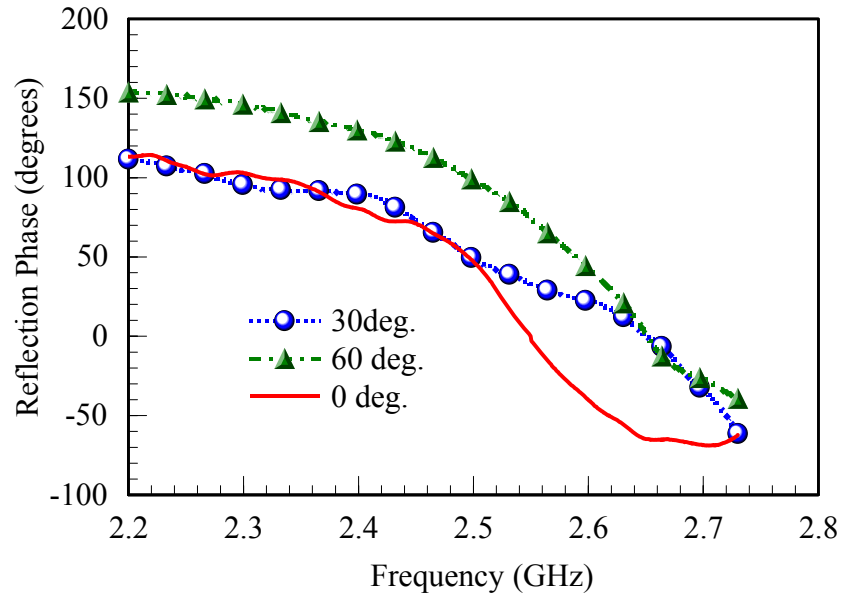
Figure 5.18 - Measured reflection phase (deg.) vs. frequency for angles of incidence of 0˚, 30˚ and 60˚. The normal incidence wave (0˚) shows a bandwidth from 2.5 to 2.6 GHz with center frequency at 2.55 GHz. The oblique angles of incidence, 30˚ and 60˚, present a respective bandwidth from 2.51 to 2.71GHz and from 2.59 to 2.73 GHz. with center frequency at 2.65 GHz.

The apparent frequency shift in the measurement result is a consequence of sensitivity to the set up for the reflection measurement on the metal sheet versus the FSS. If the distance from the transmit/receive antennas to the metal is different from the transmit/receive antennas to the FSS, when normalizing the second measurement to the first, the off-set distance add an extra phase shift which causes the frequency to move. Another factor contributing to the frequency shift is the bonding between layers (superstrate/substrate). Any gap between layers adds an extra length to the substrate path of the travelling wave, thus an extra phase is included and the frequency moves up. This statement is confirmed through simulations as shown in Figure 5.19. In addition, an air gap will also affect the ε_{eff}, disturbing the effectives of the grid design.
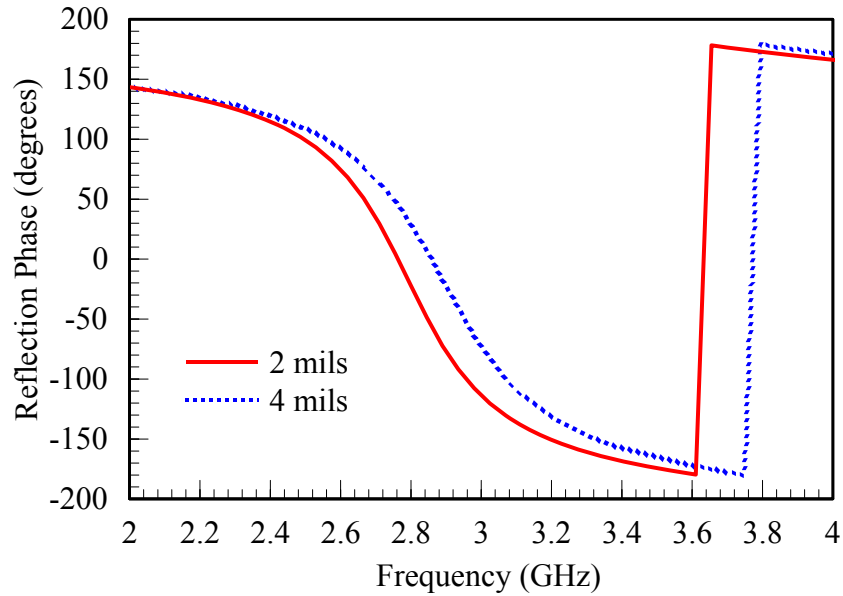
Figure 5.19 - Frequency shift caused by air gap between superstrate and substrate layers.

5.5 Conclusion

A multilayer JC-FSS presenting frequency stability for a large angular spectrum (0˚ to 80˚) of incidence for both TE and TM polarizations has been achieved. The FSS has been realized through excellent design techniques applying equation modeling and simulations. The addition of a superstrate affects the FSS by adding capacitance from the grid. The simulated results showed an angular stability for the resonant frequency of up to 70˚ for the TE wave and minimum shift on the TM wave. On the simulations describing bandwidth, changes are noticed for the larger angles (60˚) for both TE and TM waves. However these shifts do not degrade the operation of the FSS since the ISM band is still included in band-gap. The measurement results show the expected 180˚ phase shift between the FSS and a metal ground plane at 2.55 GHz for normal incidence and at 2.65 GHz for oblique incidence (30˚ and 60˚). The frequency shift is related to sensitivity to the measurement set up and fabrication.

Chapter 6

Quasi Yagi Antenna Backed by the Jerusalem Cross Frequency Selective Surface

6.1 Introduction

This chapter introduces a new alternative for metal shielding of a quasi Yagi antenna with a ground plane. As mentioned in earlier chapters having a quasi Yagi antenna with end fire radiation over a metal ground plane is very challenging. The end fire radiation pattern is affected by the surface currents from the metal ground degrading the currents from the antenna and as a result the radiation pattern is tilted to the broadside direction. One solution to this problem, previously discussed in chapter 4, is to displace the ground metal away from the quasi Yagi antenna by a distance of $\approx$7.5mm (0.19λ_g). The solution presented here proposes backing the quasi Yagi with the Jerusalem Cross Frequency Selective Surface (JC-FSS) presented in chapter 5. The JC-FSS suppresses the propagation of undesired surface waves from the ground within a forbidden frequency band and also provides frequency stability for large angles of TE and TM polarized incident waves. To the best of the author's knowledge this is the first instance that a quasi Yagi is packaged over a JC-FSS to achieve end fire radiation. Using a JC-FSS versus a ground displacing slab 7.5mm thick (chapter 4) as the backing structure presents benefits such as a size reduction for the overall antenna height of 33% and 14˚ of additional beam steering in the end fire direction. If compared to a quasi Yagi of same substrate profile (5mm) with no JC-FSS the presented design offers wider bandwidth (220MHz) and 27˚ more beam steering.

In this chapter we present the quasi Yagi design on top of the JC-FSS. The antenna elements are optimized from the configuration in chapter 4 to account for the new substrate layer of the JC-FSS. The prepared antenna is simulated and measured, and the results on return loss and radiation patterns are compared. Small disagreement from these results on the overall frequency bandwidth has lead to an additional analysis on the sensitivity of the design to small air gaps between substrate layers during their adhesion. Furthermore, the proposed design is evaluated against a design for the quasi Yagi with same substrate but height without the JC-FSS. Finally the measured results on return loss and radiation patterns for the quasi Yagi from chapter 4 and the design proposed here are compared.

6.2 Design of the Quasi Yagi Antenna over the JC-FSS

A quasi Yagi antenna consists of an array dipoles printed on a high permittivity substrate (ε_r = 10.2) and fed by a microstrip to CPS transition, where the ground from the microstrip transition is used as reflector for the array. The novel feature proposed here is to shield the radiating dipoles in the quasi Yagi array by including an electromagnetically altered ground plane, the JC-FSS. The JC-FSS consists of a periodic cell of self resonant grids (crosses) printed on a substrate (ε_r = 10.2) with metal backing. This textured structure suppresses the propagation of undesired surfaces waves from the ground plane in a forbidden frequency band and provides frequency stability for a large angular spectrum of TE/TM polarized waves. Figure 6.1 shows the quasi Yagi antenna laying flat on top of the JC-FSS. The truncated ground plane from the transition and the ground plane from the FSS are connected to the same potential through shorting vias.

The sizes for the antenna elements in Figure 6.1 are optimized through simulations in Ansoft HFSS from Figure 4.9 to account for the added JC-FSS. Here, the added dielectric slab used to displace the ground from the antenna elements in Figure 4.9 is replaced by the JC-FSS. The overall size of the antenna is 58mm × 86mm. The dimensions for the new optimized quasi Yagi antenna are listed in Table 6.1. The most significant adjustments are a reduction on the separation of the driver and director (30%) and a decrease the overall substrate profile (33%).

The JC-FSS implemented here was previously derived in chapter 5 (Figure 5.3). The design offers in-phase reflection ($1e^{j0^\circ}$) and suppression of undesired surface waves from the ground for an operational bandwidth (band gap) extending from 2.39 to 2.5 GHz at normal incidence. In addition, at the center frequency (2.45GHz) the JC-FSS offers frequency stability for large angular spectrum (<70°) of both TE and TM polarized incident waves. Figure 6.1 shows that 35 Jerusalem crosses were used for this work.

Table 6.1 - Optimized dimensions of the antenna elements.

Antenna Element	Chapter 4 (mm)	QY with JC-FSS (mm)
Length of CPS (Sref)	18.33	20.5
Length of Driver (Ldri)	34	35.5
Length of Director (Ldir)	18	18
Separation of driver and director (Sdir)	16	11.16
Separation of director/substrate (Ssub)	10.83	16
Height of substrate layer (H)	7.5	5
Height of truncated section (h1)	2.5	2.5
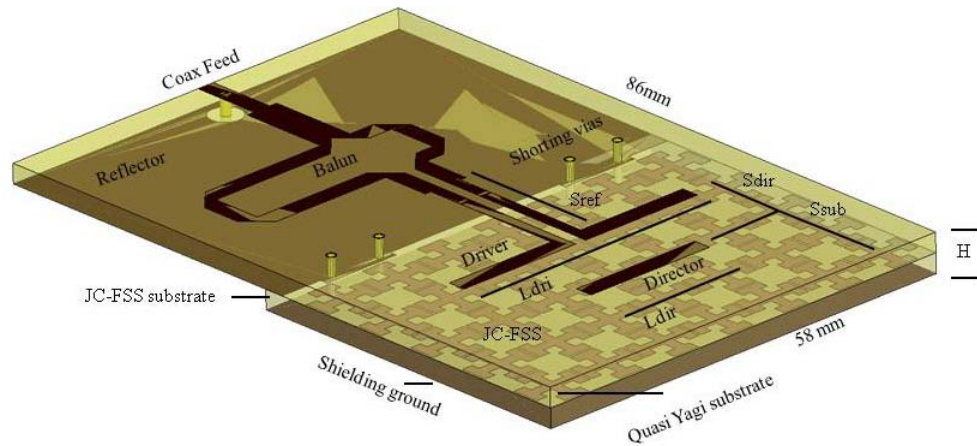
Figure 6.1 - Quasi Yagi antenna over a Jerusalem Cross Frequency Selective Surface.

6.3 Simulation and Measurement of the Quasi Yagi over the JC-FSS

The simulated and measured results on return loss for the quasi Yagi antenna over the JC-FSS are compared in Figure 6.2. The simulated data demonstrate an operational bandwidth from 2.24 to 2.46 GHz and the measured data from 2.29 to 2.55 GHz. However, the measured frequency band is shifted up in frequency, suffering from undesired reflections at the 2.4 to 2.5 GHz frequency range, as a result of the sensitivity of the JC-FSS to small air gaps from the adhesive used to glue the antenna substrate to the JC-FSS substrate. The frequency shift was previously predicted in Figure 5.19 for the JC-FSS alone and is confirmed here in Figure 6.3 for the combined structure. Figure 6.3 describes a simulation including a small air gap of 1.5 mils between substrate layers; the result exhibit the frequency variation observed in the measured data.

103
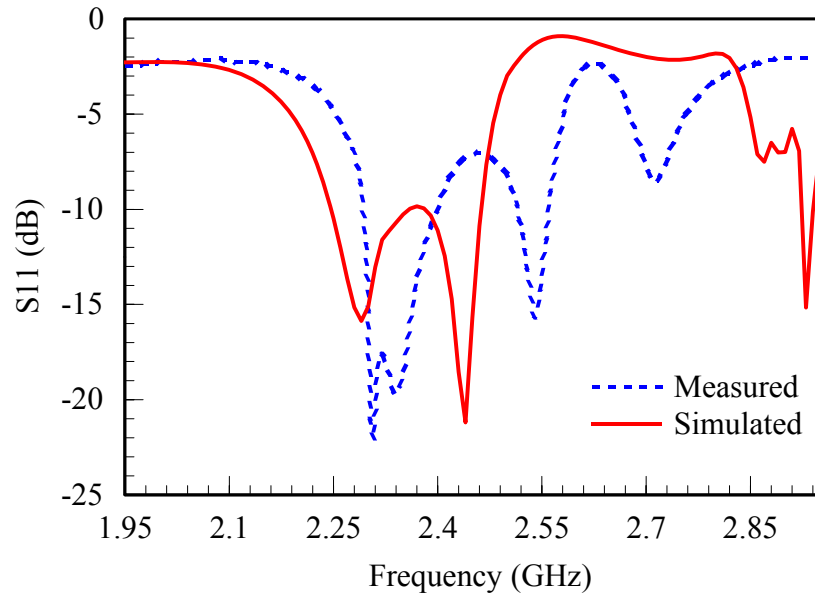
Figure 6.2 - Simulated vs. measured return loss for the quasi Yagi over the JC-FSS. The simulated return loss bandwidth extends from 2.24 to 2.46 GHz while the measured bandwidth extends from 2.29 to 2.55 GHz.
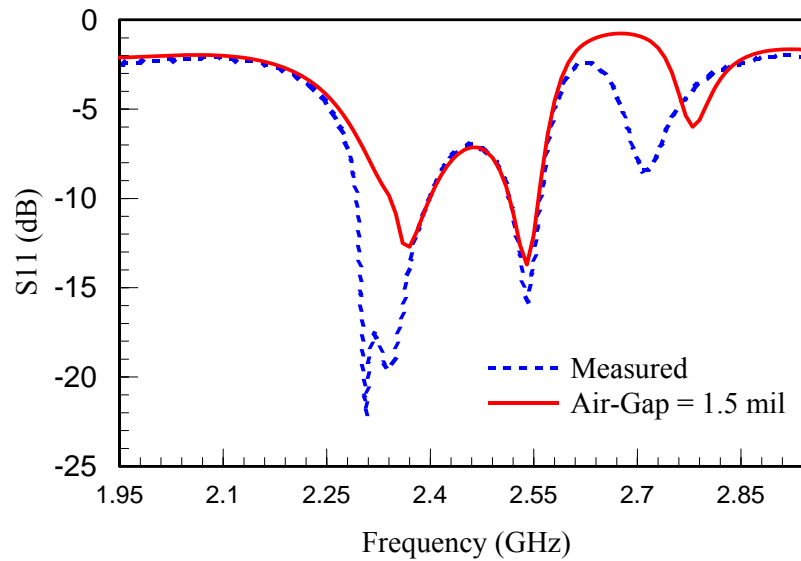
Figure 6.3 - Simulation including 1.5 mil air gap between substrate layers vs. measurement for the quasi Yagi over the JC-FSS to attest for the frequency shift on the measured design.

The results for the simulated and measured normalized H-plane pattern taken at 2.45 GHz are illustrated in Figure 6.4 and Figure 6.5 respectively. The simulated and

104

measured results demonstrate a co-polarized H-plane (H-CPOL) pattern with beam steering of 45˚ and 54˚. At 45˚ the simulated beam peak is 1 and 3 dB larger than at the end fire (θ = 90˚) and broadside (θ = 0˚) directions. Correspondingly the measured beam peak at 54˚ is 2 and 3 dB larger than at θ = 90˚ and 0˚. Furthermore, with respect to main beam directivity, the H-CPOL pattern presents 3 dB beamwidth for the simulated and measured patterns of 95˚ and 100˚. The simulated and measured H-plane cross-polarization (H-XPOL) levels are -22.6 and -13 dB. The drastic increase in the measured H-XPOL level is attributed to measurement set up tolerances, sensitivity of the JC-FSS to large angles of incidence and to the air gap resulting from the adhesive. If the frequency band gap moves up enough such that the frequency of interest (2.45GHz) falls below the band gap, then the surface impedance is inductive and TM surface waves from the ground radiate readily thereby increasing the X-POL levels [15].
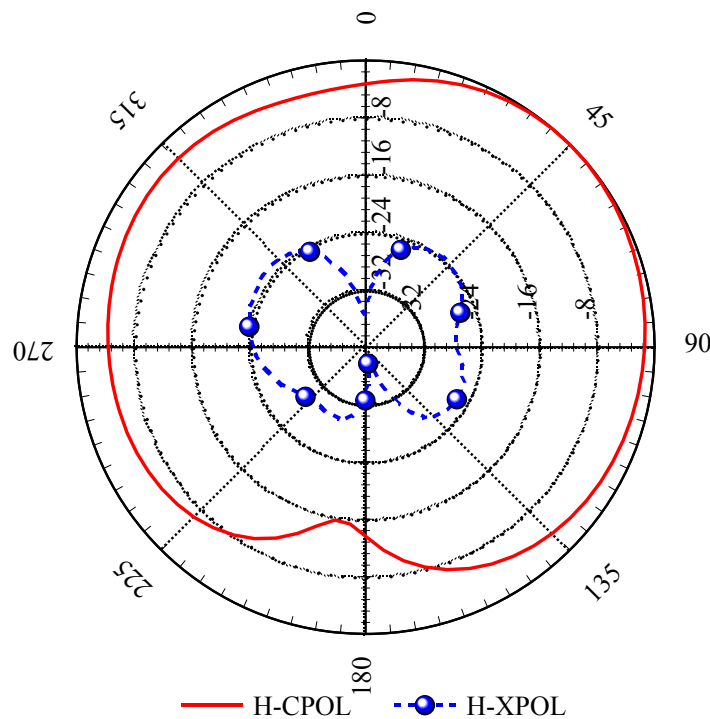
Figure 6.4 - Simulation of the normalized H-plane pattern at 2.45 GHz for the quasi Yagi over the JC-FSS. The beam peak angle shows a maximum tilt of 45˚. The pattern is normalized to the H-CPOL value.
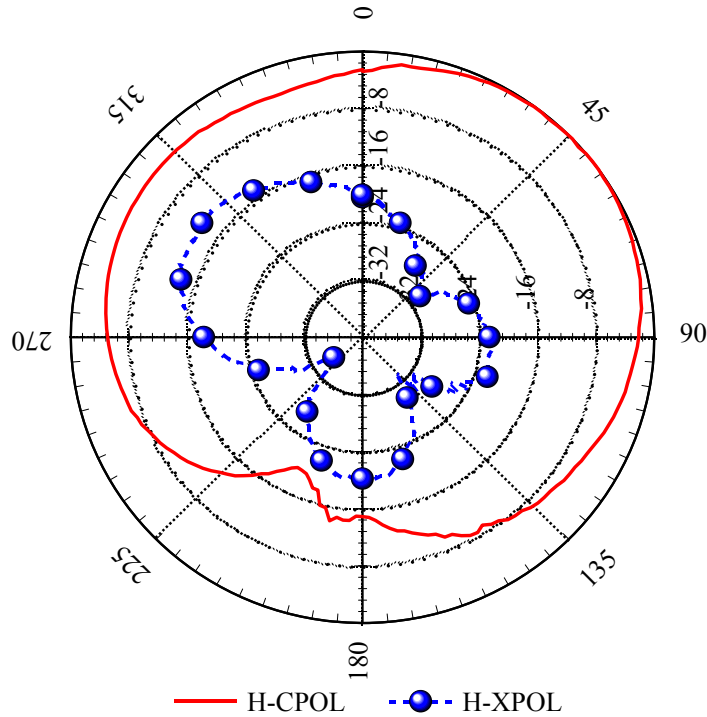
Figure 6.5 - Measurement for normalized H-plane pattern at 2.45 GHz. The maximum beam peak is recorded at 54˚. The pattern is normalized to the H-CPOL value.

The normalized E-plane co-polarization (E-CPOL) and cross polarization (E-XPOL) patterns at 2.45 GHz are displayed in Figure 6.6 and Figure 6.7. The simulated and measured C-POL exhibit a directional pattern with front-to-back ratios of 3 dB and 2 dB respectively, while the X-POL level are -8 dB and -4.35 dB. In comparison to conventional non-grounded quasi Yagis [14], the front-to-back ratio is 12 dB smaller and the X-POL level is 8dB larger. The diminished front-to-back ratio and the increased in X-POL level for the measured pattern is caused by the radiation of TM surface waves from the ground as previously explained on the H-plane case. Finally, the simulated and measured 3 dB beamwidth for the E-CPOL are 90˚ and 92˚.
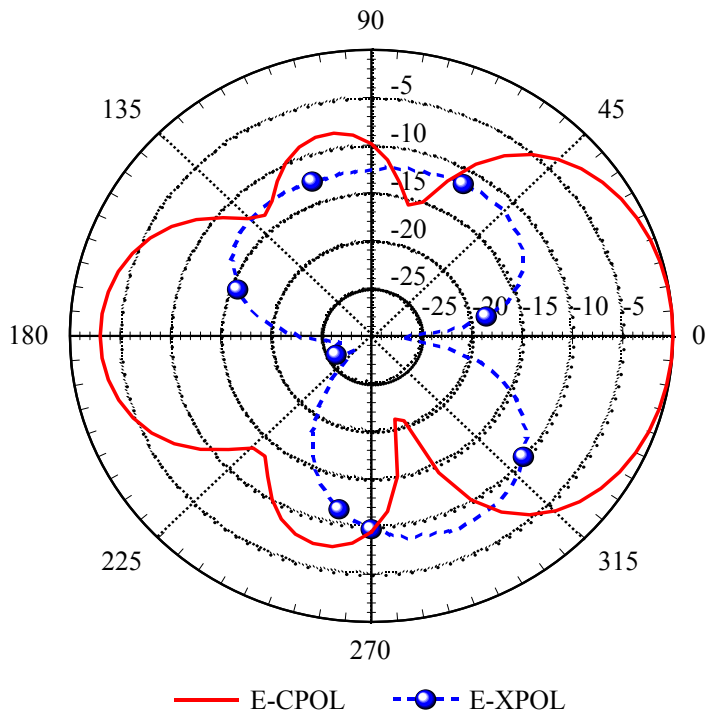
Figure 6.6 - Simulation on the normalized E-plane pattern at 2.45 GHz for the quasi Yagi over the JC-FSS. The pattern is normalized to the E-CPOL peak value.
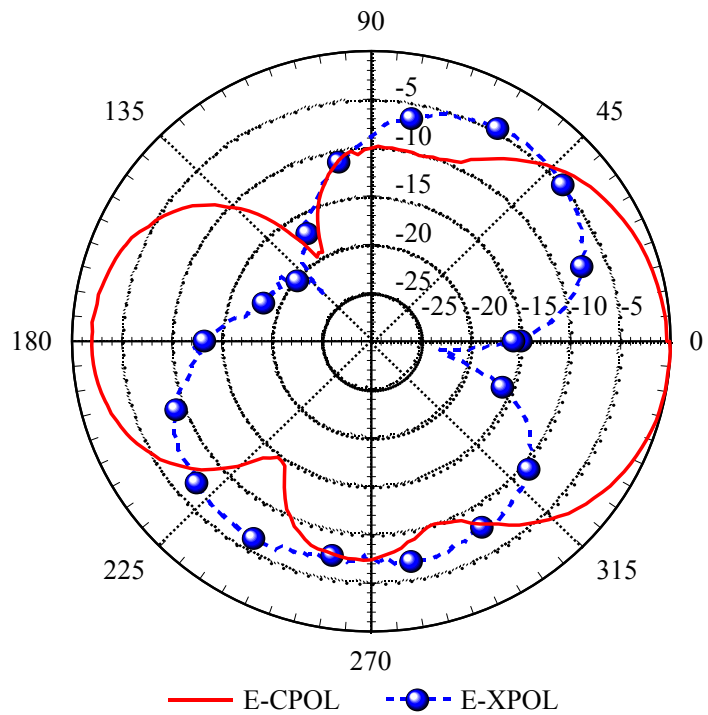
Figure 6.7 - Measurement on the normalized E-plane pattern at 2.45 GHz for the quasi Yagi over the JC-FSS. The pattern is normalized to the E-CPOL value.

The simulated and measured gains versus frequency are compared in Figure 6.8. The results present close agreement at 2.45 GHz for a simulated gain of 3.98 dB and a measured gain of 3.2 dB. The simulated and measured directivities are 5 and 6.5 dB with respective radiation efficiency of 77 % and 47%. The decrease on the measured radiation efficiency is a consequence of the discussed reflections at 2.45 GHz from the air gap between substrate layers.
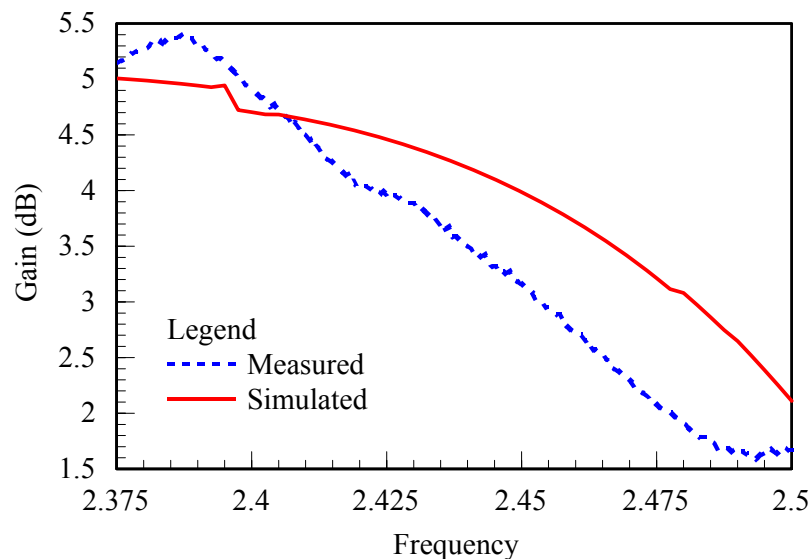
Figure 6.8 - Simulated and measured gain versus frequency for the quasi Yagi over the JC-FSS.

6.4 Quasi Yagi Antenna of Same Profile with and without a JC-FSS

Simulations are performed on a quasi Yagi antenna printed on a 5mm thick grounded dielectric slab and the results are compared to the design proposed in this chapter (Figure 6.1).The assessment presented in Figure 6.9 for return loss bandwidth shows a drastic improvement of 220MHz in the return loss for the quasi Yagi including the JC-FSS versus the quasi Yagi over the 5 mm thick grounded slab. A similar

evaluation is shown in Figure 6.10 and Figure 6.11 comparing the co polarization (C-POL) and cross polarization (X-POL) levels for the H-plane and E-plane patterns. In Figure 6.10, for the quasi Yagi design backed by the JC-FSS, the H-plane C-POL pattern provides an additional 27˚ of beam steering towards the end fire direction and the X-POL pattern is reduced by -2 dB. In Figure 6.11, the E-plane pattern X-POL level for the quasi Yagi over the JC-FSS versus the 5mm thick slab is reduced by -2 dB. Higher X-POL level is exhibited for the 5mm thick grounded dielectric slab because in this configuration the radiation from the quasi Yagi is degraded by out of phase reflections and TM surface waves radiating from the ground metal.
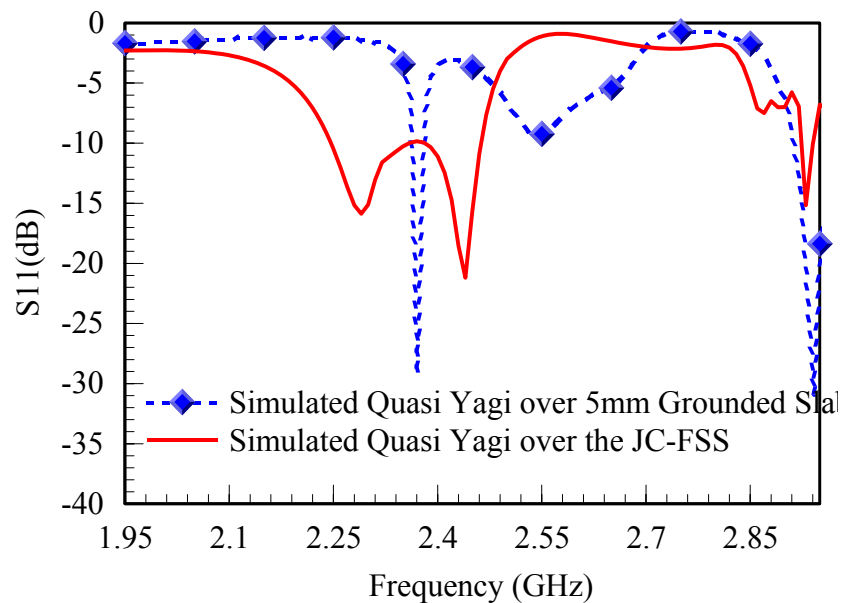
Figure 6.9 - Simulation comparing the return loss bandwidth for a quasi Yagi resting on top of a grounded dielectric slab 5mm thick versus the quasi Yagi design on top of the JC-FSS. The simulated bandwidth for the grounded slab is very narrow (2.35GHz) while the bandwidth of the quasi Yagi including the JC-FSS extends from 2.24 to 2.46 GHz.

109
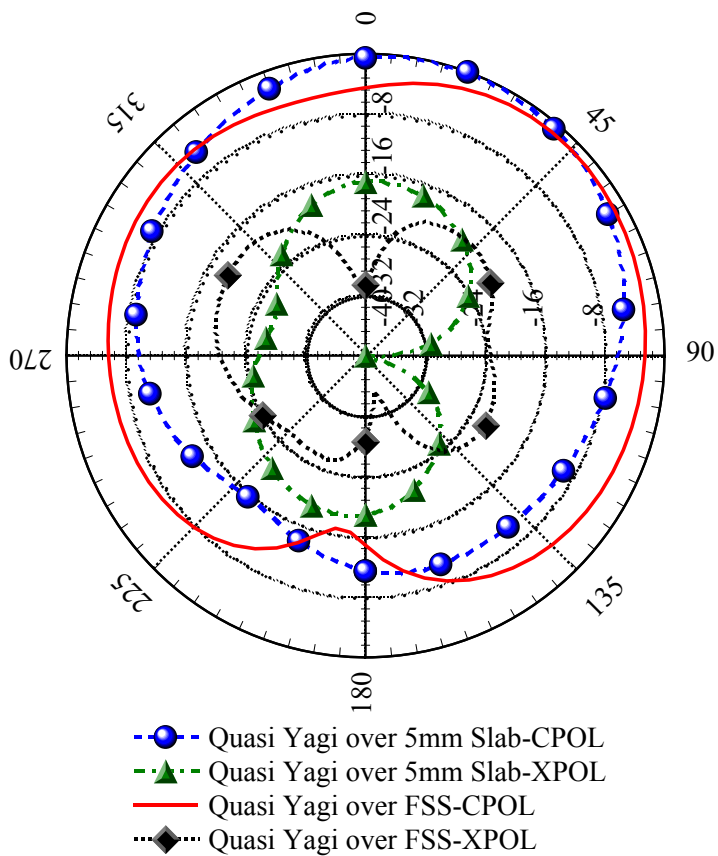
Figure 6.10 - Co and cross polarization of the H-plane pattern at 2.45 GHz for the quasi Yagi design on top of a grounded dielectric slab 5mm thick versus the quasi Yagi design on top of the JC-FSS.
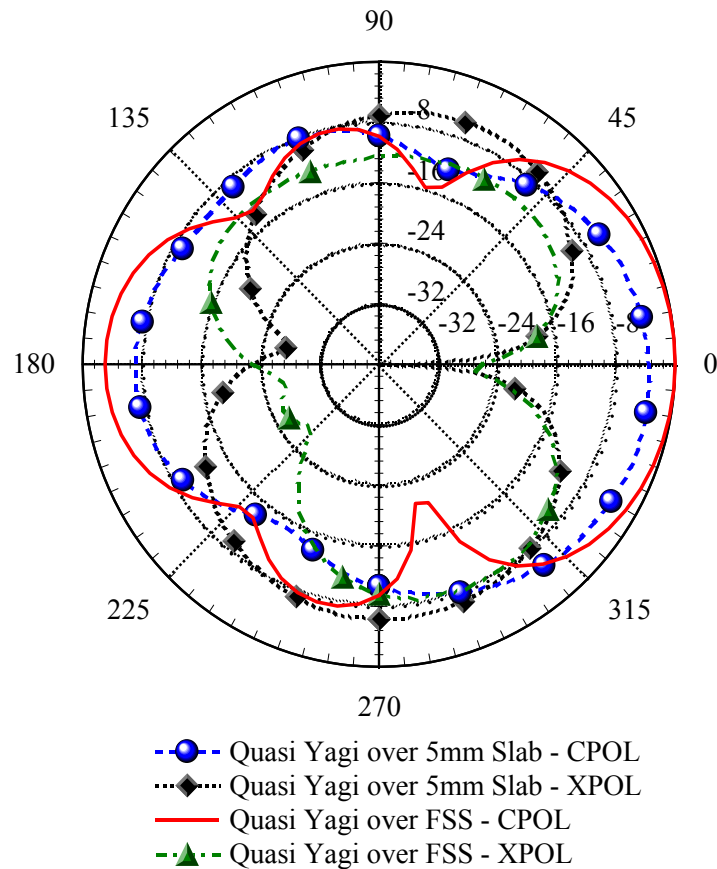
Figure 6.11 - Co and cross polarization on the E plane pattern at 2.45 GHz for the quasi Yagi on top of a grounded dielectric slab 5 mm thick versus the quasi Yagi on top of the JC-FSS.

6.5 Comparison of Measured Antennas

This section compares the measurements of the quasi Yagi printed on a grounded dielectric slab 7.5mm thick (Figure 4.9) against the quasi Yagi backed by a JC-FSS with an overall profile thickness of 5mm. In Figure 6.12, the operating frequency band for the measured quasi Yagi printed on a thick grounded slab (Figure 4.9) extends from 2.36 to 2.55 GHz while the bandwidth for the measured quasi Yagi over the JC-FSS extends from 2.29 to 2.55 GHZ. As explained in Figure 6.3 for the quasi Yagi over the JC-FSS, the small air gap resulting from the adhesion of substrate layers has degraded the return loss (<10dB) over the frequency range from 2.4 to 2.5 GHz. This reflection is observed in

the C-POL H and E-plane patterns (Figure 6.13 and Figure 6. **14**) for 2.45 GHz as 1 dB difference between maximum beam peaks for the quasi Yagi over the JC-FSS versus on top the grounded slab

The most significant improvements brought in by the quasi Yagi packaged over the JC-FSS are 14° of additional beam steering towards the end fire direction, as shown by the H-CPOL pattern from Figure 6.13, and overall substrate profile reduction by 33% in comparison to the thick grounded slab.
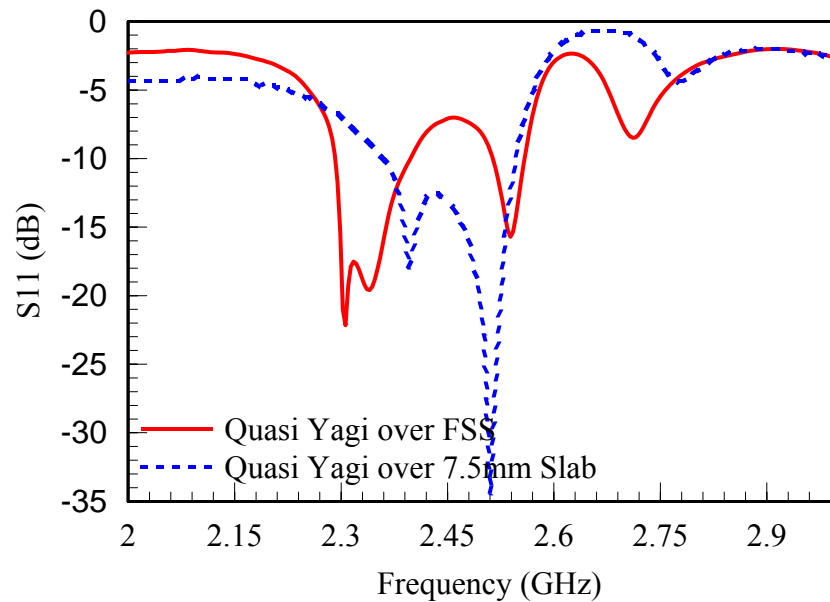
Figure 6.12 - Return loss for Quasi Yagi over FSS versus quasi Yagi over 7.5 mm slab. The frequency band for the quasi Yagi over FSS extends from 2.29 to 2.55 GHz. The frequency band for the quasi Yagi over the 7.5mm slab extends from 2.36 to 2.55 GHz.
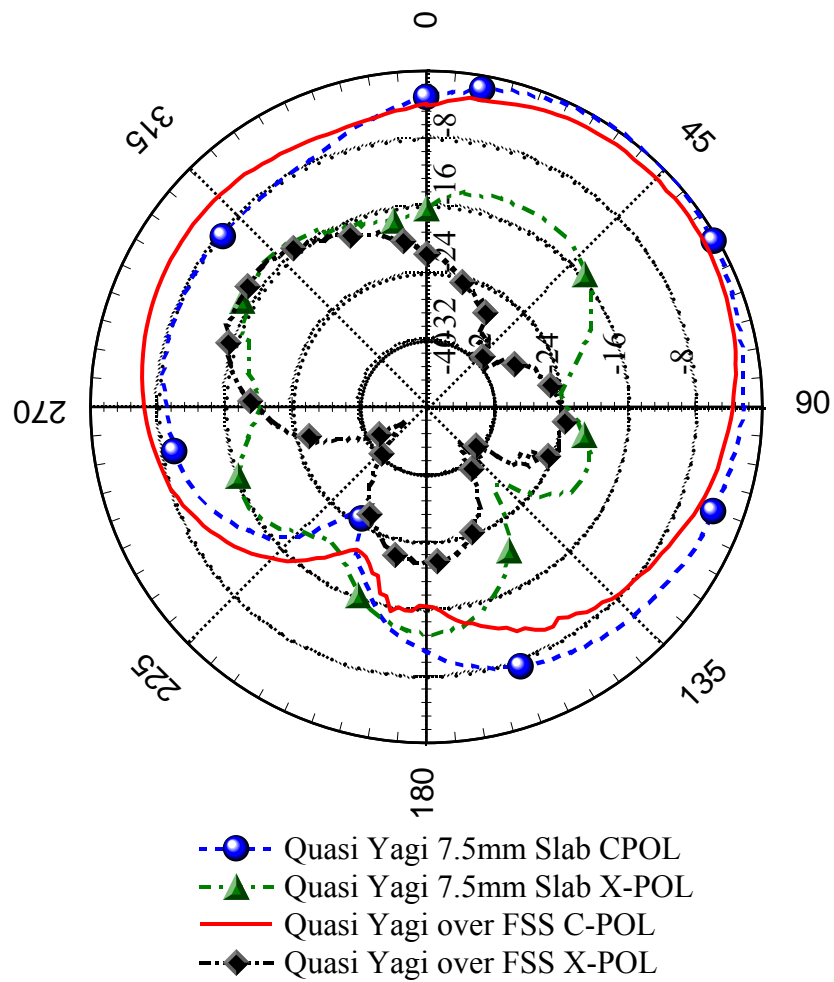
Figure 6.13 - Measured H-plane C-POL and X-POL for the quasi Yagi over the JC-FSS and the quasi Yagi over the 7.5mm slab. The beam tilt for the quasi Yagi over the JC-FSS is 54° versus 40° for the quasi over 7.5mm slab.
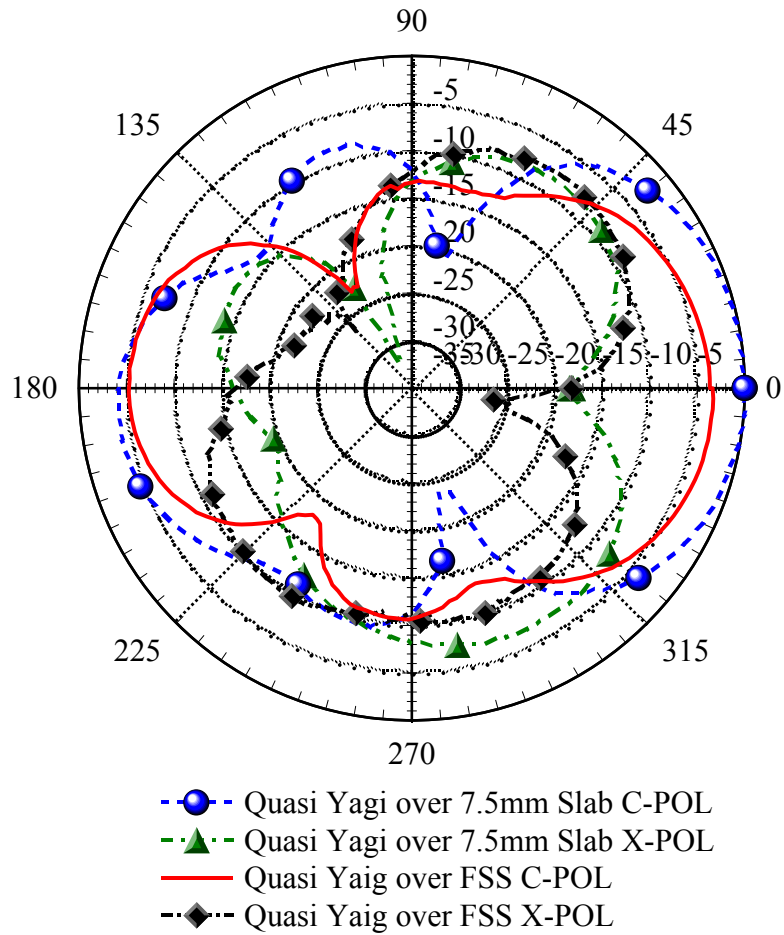
Figure 6. 14 - Measured E-plane C-POL and X-POL pattern for the quasi Yagi over the JC-FSS and the quasi Yagi over the 7.5mm slab.

6.5 Conclusion

A new design for a quasi Yagi antenna shielded by a metal ground and with end fire radiation has been proposed. The design consisted of placing a quasi Yagi over a JC-FSS. This is the first time that these two structures are combined for end fire operation. The simulated and measured H-plane patterns showed beam steering with maximum peak directed at 45˚ and 54˚, respectively. From this assessment it is also learned that the proposed design is very sensitive to small air gaps resulting from the adhesion of the antenna substrate to the JC-FSS substrate. This air gap shifts the operational band up in

frequency and degrades the return loss and gain over the frequency range from 2.4 to 2.5 GHz.

In comparison to a design of same substrate height (5mm) but without the JC-FSS, the proposed design offers 220MHz of more bandwidth, 27˚ of extra beam steering in the end fire direction, reduction of X-POL level for the H and E-plane of ≈ -2dB. Furthermore, when compared to the option previously proposed in chapter 4 with the quasi Yagi placed over a thick grounded slab, the proposed design offers a profile reduction of 33%, and 14˚ of additional beam steering in the end fire direction.

Chapter 7

Review and Recommendations

7.1 Summary of New Contributions to the Field

This research has presented two different options to achieve end fire radiation with a quasi Yagi antenna packaged over a metal ground plane. The first option included a high profile substrate 7.5 mm thick to displace the ground metal away from the antenna. The main additions from this configuration are 40˚ of beam steering towards the end fire direction and an ample operational bandwidth extending from 2.36 to 2.55 GHz. The second option consisted of packaging the quasi Yagi antenna over a Jerusalem Cross Frequency Selective Surface (JC-FSS). This arrangement improves on the first option by reducing the overall antenna profile by 33%, adding 14˚ of more steering in the end fire direction, and expanding the operational bandwidth from 2.29 to 2.55 GHz. Furthermore, the impact of including the antenna substrate (superstrate) for the derivation of the grid model for the JC-FSS is also discussed. Accounting for the superstrate (ε_{reff} = 9.7) versus assuming air (ε_{reff} = 6.8) allows to use cross grid sized for 3.2 GHz at 2.45 GHz. In other words, the addition of the superstrate tunes the frequency down from 3.2 to 2.45 GHz for the same cross grid size.

The following features are unique and novel contributions to the antenna field from this work: development of a quasi Yagi antenna with end fire radiation when completely backed by a ground metal, implementation of the JC-FSS as antenna backing

structure to achieve end fire radiation, and the inclusion of the antenna substrate for tuning in the derivation of the JC-FSS.

7.2 Recommendations for Future Work

The analysis and experiments performed in this research have set the foundation for future work on end fire antennas over a JC-FSS. The following are suggestions for future research that will expand on the work prepared here. Further optimizations should be carried on the crosses of the FSS for the combined structure, including the quasi Yagi antenna, to tune the resonant frequency band of the FSS to an angle of reflection phase where the radiation pattern can be steered further in the end fire direction. Similar results can be accomplished if the FSS is made electronically tunable by including BST varactor diodes between the grids. Each varactor diode is controlled by a bias voltage which varies the surface impedance (effective capacitance) and tunes the operating frequency band for the FSS. Another improvement for this work is to model the air gap between the superstrate and substrate layers in the simulations and closed form equations to better predict the resulting frequency shift. In addition, if copper etching is used for the fabrication of the FSS rather than milling, a better estimation can be made on the air gap based on the amount of copper cladding and adhesive used. Another enhancement is to implement a better test set up to measure the reflection phase for the FSS, as explained in chapter 5 if the fixture under test (metal or FSS) is not kept at the same distance to the transmit/receive antenna for each measurement the difference will result in a frequency shift. Finally, other candidates for end fire radiators (e.g. microstrip Yagi array) should be tested to be use with the JC-FSS.

References

[1] J.M Bell and M.F Iskander, "A Low-Profile Archimedean Spiral Antenna Using an EBG Ground Plane," *IEEE Antennas and Wireless Propagation Letters*, VOL. 3, 2004, pp.223-226.

[2] S. Zhu and R. Langley, "Dual-band wearable antennas over EBG substrates," Electronic Letters, Feb. 1st 2007, VOL. 43 No. 3.

[3] Q. Luo, H. M Salgado, A.R Moura, J.R. Pereira, "Dual-Band Antenna Design Using an EBG Artificial Magnetic Conductor Ground Plane," Loughborough Antennas & Propagation Conference, March. 17-18 2008, Loughborough, UK.

[4] J.J Lee, R.J Broas, S. Livingston, D. Sievenpiper, "Flush-Mounted Antennas on Hi-Z Ground Planes," IEEE Antennas and Propagation Society International Symposium, 2002, VOL. 3, pp.764-767.

[5] D. Sievenpiper, J.H Schaffner, J. Song, R.Y Loo and G. Tangonan, "Two-Dimensional Beam Steering Using and Electrically Tunable Impedance Surface," IEEE Transactions on Antennas and Propagation, VOL. 51, NO. 10, October 2003, pp.2713-2721.

[6] L. Akhoondzadeh-Asl, P.S. Hall, J. Nourinia and Ch. Gobadi, "Influence of Angular Stability of EBG Structure on Low Profile Dipole Antenna Performance," IEEE International Workshop on Antenna Technology Small Antennas and Novel Metamaterials, March 6-8 2006, pp. 253-256.

[7] C.A Balanis, "Antenna Theory Analysis and Design," John Wiley & Sons, INC. 3rd Edition, New York, 2005, pp.283-303.

[8] F.J. Zucker "Surface and leaky-wave antennas," in *Antenna Engineering Handbook*, H. Jasik, Ed. New York: McGraw-Hill, 1961.

[9] N. Kaneda, Y. Qian. Amd T. Itoh, "A novel Yagi-Uda dipole array fed by a microstrip-to-CPS transition,"in *Asia-Pacific Microwave Conf. Deg.,* Yokohama, Japan, Dec. 1998, pp. 1413-1416.

[10] C.H. Tsao, Y.M Hwang, F. Kilburg and F. Dietrich, "Aperture-coupled patch antennas with wide-bandwidth and dual-polarization capabilities," in *IEEE AP-S Int. Symp. Dig.*, New York, NY, June 1988, pp. 936-939.

[11] Y. Yoshimura, "A microstripline slot antenna," *IEEE Trans. Microwave Theory Tech.,* vol. MTT-20, pp. 760-762, Nov. 1972.

[12] Y.Qian and T.Itoh, "A broadband uniplanar microstrip-to-CPS transition," *Asia-Pacific Microwave Conf. Dig.*, pp. 609-612, Dec. 1997.

[13] D.M Pozar, Microwave Engineering, 3rd Ed. New York: Wiley, 2005, pp. 59, 360 and 470.

[14] W.R Deal, N. Kaneda, J. Sor, Y. Qian, and T. Itoh, "A New Quasi-Yagi Antenna for Planar Active Antenna Arrays," *IEEE Trans Microwave Theory Tech*, vol.48, pp. 910-918, June 2000.

[15] D. Sievenpiper, "High-impedance electromagnetic surfaces," Ph.D. dissertation, Dept. Elec. Eng., Univ. California at Los Angeles, Los Angeles, CA,1999.

[16] T. Itoh, "Planar Antenna Arrays for Ku/Q Bands," Dept. Elect. Eng., Univ. California, Los Angeles, Final Rep., 2000-2001 for MICRO Project 00-041.

[17] J. Huang, "Planar Microstrip Yagi Array Antenna," *IEEE APS/USRI Symposium Digest*, June 1989, pp.894-897.

[18] F.T Ulaby, "Fundamentals of Applied Electromagnetics," 2001 Media Edition, Prentice Hall, N.J., 2001, pp. 164-166, 213-214.

[19] C.A Balanis, "Advanced Engineering Electromagnetics," John Wiley and Sons, Inc. 1989, pp. 210-214 and 235-236.

[20] Y. Qian, W.R. Deal, N. Kaneda, and T. Itoh, "A uniplanar quasi-Yagi antenna with wide bandwidth and low mutual coupling characteristics," in *IEEE AP-S Int. Symp. Dig.*, vol.2, Orlando, FL, July 1999, pp.924-927.

[21] R.F Harrington, Time-Harmonic Electromagnetic Fields, McGraw-Hill, New York, 1961, pp.163-169.

[22] D. Sievenpiper, L. Zhang, R. Broas, N.G Alexopolous, and E. Yablonovitch, "High-Impedance Electromagnetic Surfaces with a Forbidden Frequency Band," *IEEE Transactions on Microwave Theory and Techniques*, Vol. 47, No. 11, Nov. 1999.

[23] C.R. Simovski, S.A. Tretyakov, and P. de Maagt, "Artificial high impedance-surfaces: Analytical theory for oblique incidence," in Proc. Antennas Propag. Soc. Int. Symp., vol. 4, 2003, pp.434-437.

[24] C.R. Simovski, P. de Maagt S.A. Tretyakov, M. Paquay, and A. A. Sochava, "Angular stabilization of resonant frequency of artificial magnetic conductor for TE-incidence," Electron. Lett., vol.40, no.2, pp. 92-93, 2004.

[25] M. Hosseini, A. Pirhadi, and M. Hakkak, "Design of an AMC with little sensitivity to angle of incidence using an optimized Jerusalem cross FSS," in Proc. IEEE Int. Workshop Antenna Technol.: Small Antennas Novel Metamat., New York, USA, 2006, pp.245-248.

[26] M. Hosseini and M. Hakkak, "Characteristic estimation for Jerusalem Cross Based artificial magnetic conductors," IEEE Antennas and Wireless Propag. Letters. Vol. 7, 2008.

[27] C.R. Simovski, P .de Maagt, I.V. Melchakova, "High-impedance surfaces having stable resonance with respect to polarization and incidence angle," IEEE Transactions on Antennas and Propagation, vol. 53, no. 3, March 2005.

[28] Munk, Ben, Frequency Selective Surfaces Theory and Design, John Wiley & Sons, Inc., pp.26-63

[29] J.A. Arnaud, "Resonant-Grid Quasi-Optical Diplexers," Electronics Letters, Dec. 1973, vol.9 No.25.

[30] W. Gregorwich, "The design and development of frequency selective surfaces for phased arrays," IEEE Aerospace Conference Proceedings, vol.5, pp.471-479.

Appendices

Appendix A: Plane Wave Functions

This appendix describes the equations used to derive the cutoff frequencies for the TM and TE modes in a dielectric slab guide and in a dielectric covered ground plane [21]. The dielectric slab guide equations are in the quasi Yagi with no metal backing, chapter 3. The grounded dielectric slab equations are used in the quasi Yagi with metal backing, chapter 4. For the quasi Yagi from chapter 3 with a substrate height of 2.5 mm, the dominant modes are TE_0 and TM_0. For the quasi Yagi backed by a metal in chapter 4 and with a substrate height of 7.5 mm, the dominant mode is TM_0.

The objective of a dielectric slab guide is to store the energy within the structure and direct it towards a given direction. This is achieved by having the wave bounce back and forth between its upper and lower interfaces at an incidence angle greater than the critical angle. Once this is done, the refracted fields outside the dielectric form evanescent waves and all the energy is reflected and contained within the structure [19]. Figure A.1 shows the simples illustration of a dielectric slab waveguide.
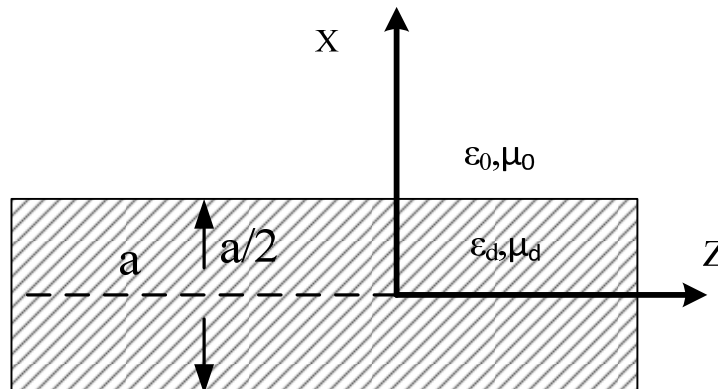

Figure A.1 – The dielectric slab waveguide

The operation of the dielectric covered ground as the one shown in Figure A.2 is based on the same principles as the dielectric slab guide, the main difference is that the

Appendix A (Continued)

present modes are those for a dielectric slab having zero tangential component of E over

the x = 0 plane. These are the TM_n (odd) for n = 0,2,4,... and TE_n (even) for n = 1,3,5,...,

the dominant mode is the TM_0 which propagates unattenuated at all frequencies.
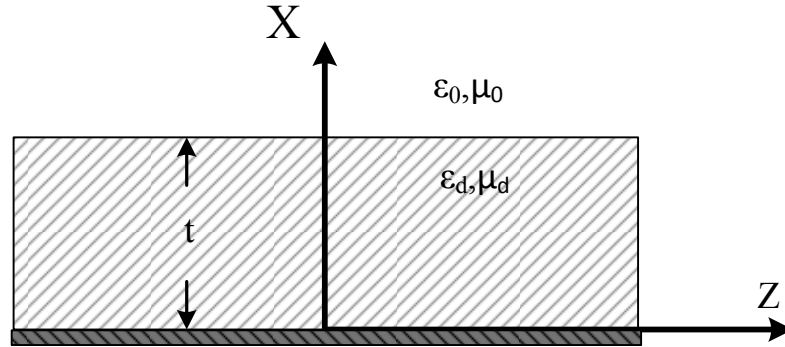

Figure A.2 – Dielectric cover conductor

The slab from Figure A.1 is analyzed as two dimensional (x-z plane) with no

variation in the y coordinate. It is desired to find the z-traveling wave which is the $e^{-jk_z z}$

variation. The modes for TM and TE on x or z need to be derived. The TM modes

propagating in z are expressed as

$$E_x = \frac{-k_z}{\omega \varepsilon} \frac{\partial \psi}{\partial x}$$

$$E_z = \frac{1}{j\omega\varepsilon}(k^2 - k_z^2)\psi$$

$$H_y = -\frac{\partial \psi}{\partial x} \qquad\qquad (A.1)$$

Consider two cases: (1) ψ an odd function of x denoted by ψ^o, and (2) ψ an even

function denoted by ψ^e. For case (1) in the dielectric region

$$\psi_d^o = A \sin ux e^{-jk_z z} \qquad |x| < a/2 \qquad\qquad (A.2)$$

and in the air region

124

Appendix A (Continued)

$$\psi_a^O = Be^{-vx}e^{-jk_zz} \qquad x > a/2$$

$$\psi_a^O = -Be^{vx}e^{-jk_zz} \qquad x < -a/2 \tag{A.3}$$

where $u = k_{xd}$ and $k_{x0} = jv$ for simplicity.

The separation parameters in the dielectric and air region are

$$u^2 + k_z^2 = k_d^2 = \omega^2 \varepsilon_d \mu_d$$

$$-v^2 + k_z^2 = k_0^2 = \omega^2 \varepsilon_0 \mu_0 \tag{A.4}$$

Evaluations of the field components tangential to the air-dielectric interface are listed next. Substituting u from (A.4) into E_z and H_y on (A.1) gives

$$E_z = \frac{A}{j\omega\varepsilon_d}u^2 \sin ux\, e^{-jk_zz} \quad |x| < a/2$$

$$H_y = -Au \cos ux\, e^{-jk_zz} \quad |x| < a/2 \tag{A.5}$$

Next, replacing (A.3) for $|x| > a/2$ into H_y for (A.1) results in

$$H_y = Bve^{-v|x|}e^{-jk_zz} \tag{A.6}$$

Similarly, replacing ψ_a^O for $x > a/2$ and $x < -a/2$ from (A.3) into E_z (A.1) results in

$$E_z = \frac{-B}{j\omega\varepsilon_0}v^2 e^{-vx}e^{-jk_zz}$$

$$E_z = \frac{B}{j\omega\varepsilon_0}v^2 e^{vx}e^{-jk_zz} \tag{A.7}$$

Continuity of E_z and H_y at $x = \pm\, a/2$ requires that E_z from (A.5) and (A.7) be related as

$$\frac{A}{\varepsilon_d}u^2 \sin\frac{ua}{2} = \frac{-B}{\varepsilon_0}v^2 e^{-va/2} \tag{A.8}$$

and H_y from (A.5) and (A.6) as

$$Au \cos\frac{ua}{2} = -Bve^{-va/2} \tag{A.9}$$

125

Appendix A (Continued)

The ratio of (A.8) to (A.9) is

$$\frac{ua}{2}\tan\frac{ua}{2} = \frac{\varepsilon_d}{\varepsilon_0}\frac{va}{2} \tag{A.10}$$

which combined with (A.4) results in the characteristic equation for calculating k_z's and the cutoff frequencies of the odd TM modes.

For the even TM modes of x in the dielectric and air region the wave functions are

$$\psi_d^e = A\cos ux\, e^{-jk_z z} \qquad |x| < a/2 \tag{A.11}$$

$$\psi_a^e = Be^{-v|x|}e^{-jk_z z} \qquad |x| > a/2 \tag{A.12}$$

The separation parameters previously listed in (A.4) are combined with (A.11) and (A.12) to calculate the field components (E_z and H_y) tangential to the air-dielectric interface as shown by

$$E_z = \frac{A}{j\omega\varepsilon_d}u^2\cos ux\, e^{-jk_z z} \quad |x| < a/2 \tag{A.13}$$

$$E_z = \frac{-B}{j\omega\varepsilon_0}v^2 e^{-v|x|}e^{-jk_z z} \quad |x| > a/2 \tag{A.14}$$

$$H_y = Au\sin ux\, e^{-jk_z z} \qquad |x| < a/2 \tag{A.15}$$

$$H_y = Bve^{-v|x|}e^{-jk_z z} \qquad |x| > a/2 \tag{A.16}$$

Continuity of E_z and H_y at $x = \pm\, a/2$ requires (A.13) and (A.14) be related as

$$\frac{A}{\varepsilon_d}u^2\cos\frac{ua}{2} = \frac{-B}{\varepsilon_0}v^2 e^{-va/2} \tag{A.17}$$

$$Au\sin\frac{ua}{2} = Bve^{-va/2} \tag{A.18}$$

The ratio of (A.17) to (A.18) provides the characteristic equation to determine k's and the cutoff frequencies of the even mode for the TM modes as shown by

$$-\frac{ua}{2}\cot\frac{ua}{2} = \frac{\varepsilon_d}{\varepsilon_0}\frac{va}{2} \tag{A.19}$$

126

Appendix A (Continued)

There is complete duality between the TM and TE modes for a slab waveguide.
The characteristic equation for the TE mode for the odd ψ is

$$\frac{ua}{2}\tan\frac{ua}{2} = \frac{\mu_d}{\mu_0}\frac{va}{2} \tag{A.20}$$

and for the even mode is

$$-\frac{ua}{2}\cot\frac{ua}{2} = \frac{\mu_d}{\mu_0}\frac{va}{2} \tag{A.21}$$

The odd wave functions generating the TE mode are the same as (A.2) and (A.3),
and for the even modes are the same as (A.11) and (A.12). The fields are obtained from
the ψ's by equations dual to (A.1), but for TE, which are

$$H_x = -\frac{k_z}{\omega\mu}\frac{\partial\psi}{\partial x}$$

$$H_z = \frac{1}{j\omega\mu}(k^2 - k_z^2)\psi$$

$$E_y = \frac{\partial\psi}{\partial x} \tag{A.22}$$

The concept of cutoff frequency for dielectric waveguides is interpreted the
following way. Above the cutoff frequency the dielectric guide propagates a mode
unattenuated (k_z is real), while below, the propagating mode is attenuated ($k_z = \beta - j\alpha$).
Since a dielectric is loss free, the attenuation must be accounted for by radiation of
energy as the wave progresses. Commonly dielectric guides operating in a radiating mode
below cutoff are used as antennas. The phase constant of an attenuated mode falls
between the intrinsic phase constant of dielectric and air; $k_0 < k_z < k_d$. This can be
explained by the following. (A.4) requires that u and υ be either real or imaginary when
k_z is real. The characteristic equations have solutions only when υ is real.

127

Appendix A (Continued)

Furthermore, υ must be positive, otherwise the field will increase with distance from slab, see (A.12) and (A.13). When υ is real and positive the characteristic equations have solutions only when u is also real. Therefore, u and υ are real.

The lowest frequency for which unattenuated propagation exists is known as the cutoff frequency. To obtained this frequency, $k_z \rightarrow k_0$ and $v \rightarrow 0$. This means that $u^2 = k_d^2 - k_0^2$ and $v = 0$. The result for both TE and TM modes are

$$\tan\left(\frac{a}{2}\sqrt{k_d^2 - k_0^2}\right) = 0 \tag{A.23}$$

$$\cot\left(\frac{a}{2}\sqrt{k_d^2 - k_0^2}\right) = 0 \tag{A.24}$$

These equations are satisfied when

$$\frac{a}{2}\sqrt{k_d^2 - k_0^2} = \frac{n\pi}{2} \quad n = 0,1,2,\ldots \tag{A.25}$$

and the cutoff frequencies are

$$f_c = \frac{n}{2a\sqrt{\varepsilon_d\mu_d - \varepsilon_0\mu_0}} \quad n = 0,1,2,\ldots \tag{A.26}$$

The modes are ordered as TM_n and TE_n according to choice of n in (A.26). The cutoff frequency for the TE_0 and TM_0 modes is zero, in other words the lowest order TE and TM mode propagate unattenuated regardless of the slab height, a sketch of the TE_0 mode is illustrated in Figure A. **3**. Equation (A.26) is used in chapter 3 to calculate the modes for the slab section beneath the dipoles for the quasi Yagi.
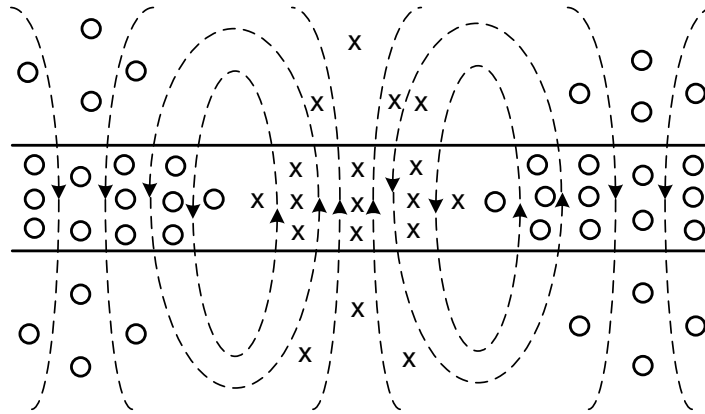
Appendix A (Continued)

Figure A. 3 – TE$_0$ mode for a dielectric slab (H lines dashed) [21]

For the grounded dielectric slab illustrated in Figure A.2, the modes are those of

the dielectric slab having zero tangential E over the x = 0 plane. These are the TM$_n$ n = 0,

2, 4,…odd modes and the TE$_n$ n = 1,3,5,…, even modes of the slab. The characteristic

equations for the TM and TE are the same as (A.10) and (A.21) respectively with a/2

replaced by t.

The cutoff frequencies are

$$f_c = \frac{n}{4t\sqrt{\varepsilon_d\mu_d - \varepsilon_0\mu_0}}$$ (A.27)

where for TM modes n = 0,2,4, …, and for TE modes n = 1,3,5, … The dominant mode

is the TM$_0$ which propagates unattenuated at all frequencies. The mode pattern is
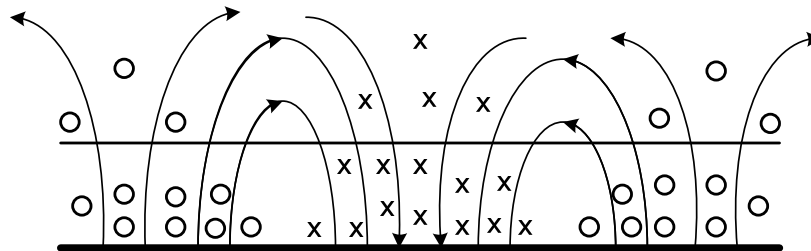
sketched in Figure A.4.

Figure A.4 – TM$_0$ mode pattern for the grounded dielectric slab (E lines solid) [21]

129

Appendix B: Derivation of the Grid Inductance

To derive the grid inductance for the narrow strip on a cross cell, an approximate equivalent circuit for a short T transmission line section having high characteristic impedance (Z_0) is used. This circuit is usually referred to as a stepped impedance low pass filters [13].

First, the ABCD parameters for a line of length l are calculated from Table 4.1 in [13]. Next these parameters are included into Table 4.2 from [13] and converted to Z parameters. The resulting Z parameters are

$$Z_{11} = Z_{22} = A/C = -jZ_0\cot\beta l \qquad (B.1)$$

$$Z_{12} = Z_{21} = 1/C = -jZ_0\csc\beta l \qquad (B.2)$$

The series elements for a T equivalent circuit are

$$Z_{11} - Z_{12} = -jZ_0\tan(\beta l/2) \qquad (B.3)$$

and the shunt element is Z_{12}, referred to Figure B.1. If $\beta l < 90°$, the series element has a positive reactance (inductor), while the shunt element has a negative reactance (capacitor). Thus the approximate equivalent circuit is shown in Figure B.2 where

$$X/2 = Z_0 \tan(\beta l/2) \qquad (B.4)$$

$$B = 1/Z_0 \sin\beta l \qquad (B.5)$$

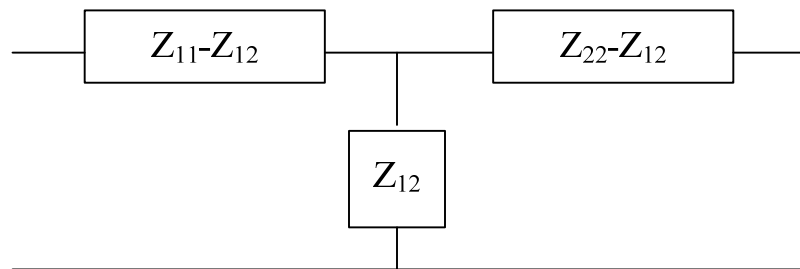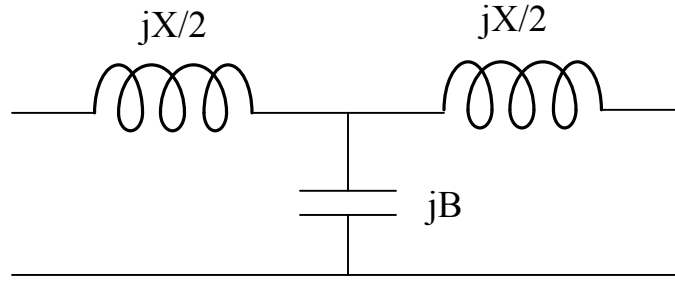Figure B.1 – Z parameters in an equivalent T circuit

130

Figure B.2 – T equivalent circuit for a transmission line section having $\beta l < 0.5\pi$

For the approximation a short length of line, where $\beta l < 45°$, and with high characteristic impedance (Z_0), (B.4) and (B.5) reduces to

$$X \approx Z_0\beta l \qquad\qquad (B.6)$$

$$B \approx 0 \qquad\qquad (B.7)$$

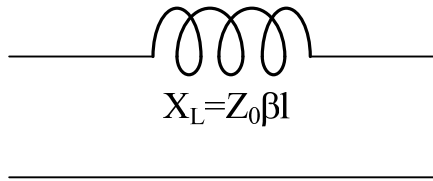and the circuit is expressed as

$$X_L = Z_0\beta l$$

Figure B.3 – Equivalent circuit for a line with small length and high Z_0

The characteristic impedance is calculated from the quasi TEM equations for a microstrip line [13].

For the narrow strip of the Jerusalem cross in this research the length is very small, 5mm, in comparison to λ_g, therefore the equivalent approximation from Figure B.3 is applicable for our derivation.

The grid inductance can also be derived through the implementation of telegraphers equations for a transmission line. The simplified equations are

$$k(f) = \omega(f)\,(L'C')^{1/2} \qquad\qquad (B.8)$$

131

Appendix B (Continued)

$$C' \cdot \text{length} = k(f)/\omega(f)Z_0^2 \text{ (F/mm)} \qquad \text{(B.9)}$$

$$L' = Z_0^2 C' \cdot \text{length (H/mm)} \qquad \text{(B.10)}$$

About the Author

Sergio E. Melais received the B.S. and M.S. degrees in electrical engineering from the University of South Florida, Tampa, in 2003 and 2005 respectively. He is currently a Ph.D. student working with Dr. Thomas Weller in the electrical engineering department at the University of South Florida, Tampa. His areas of research are RF, Microwaves, EM computations and Antenna design. He also worked as an intern for Sciperio Inc. located in Stillwater OK in the summer of 2004. Mr. Melais is a student member of the Institute of Electrical and Electronics Engineers (IEEE) since 2002 and the International Microelectronics and Packaging Society (IMAPS) since 2007.